ANL-79-39

DR.69

ANL-79-39

354
9/20/79

HIGH-PERFORMANCE BATTERIES FOR ELECTRIC-VEHICLE PROPULSION AND STATIONARY ENERGY STORAGE

Progress Report for the Period October 1978—March 1979

MASTER

ARGONNE NATIONAL LABORATORY, ARGONNE, ILLINOIS

Prepared for the U. S. DEPARTMENT OF ENERGY
under Contract W-31-109-Eng-38

DISCLAIMER

Printed in the United States of America
Available from
National Technical Information Service
U. S. Department of Commerce
5285 Port Royal Road
Springfield, VA 22161

NTIS price codes
Printed copy: A08
Microfiche copy: A01

Distribution Category:
Energy Storage--Electrochemical--
Advanced Batteries (UC-94 cb)

ANL-79-39

ARGONNE NATIONAL LABORATORY
9700 South Cass Avenue
Argonne, Illinois 60439

HIGH-PERFORMANCE BATTERIES FOR ELECTRIC-VEHICLE PROPULSION AND STATIONARY ENERGY STORAGE

Progress Report for the Period
October 1978—March 1979

P. A. Nelson	Director, Chemical and Electrical Systems
D. L. Barney	Director, Advanced Battery Projects
R. K. Steunenberg	Manager, Lithium/Metal Sulfide Battery Program
A. A. Chilenskas	Manager, Advanced Battery Technology Development
E. C. Gay	Section Manager, Battery Engineering
J. E. Battles	Group Leader, Materials Development
F. Hornstra	Group Leader, Battery Charging Systems
W. E. Miller	Group Leader, Industrial Cell and Battery Testing
D. R. Vissers	Group Leader, Cell Chemistry
M. F. Roche	Group Leader, Calcium/Metal Sulfide Battery Development
H. Shimotake	Group Leader, Cell Development and Engineering
R. Hudson	Program Manager, Eagle-Picher Industries, Inc.
R. J. Rubischko	Program Manager, Gould Inc.
S. Sudar	Program Manager, Rockwell International

May 1979

Previous Reports

ANL-77-75 July-September 1977
ANL-78-21 October-December 1977
ANL-78-45 January-March 1978
ANL-78-94 October 1977—September 1978

PREFACE

This program on high-temperature secondary batteries consists of an in-house research and development effort at Argonne National Laboratory and subcontracted work by industrial laboratories. The work at Argonne is carried out primarily in the Chemical Engineering Division, with assistance on specific problems being given by the Materials Science Division and, from time to time, by other Argonne divisions. The individual efforts of many engineers, scientists, and technicians are essential to the success of the program; recognition of these efforts is given by the individual authors that are cited throughout the report.

TABLE OF CONTENTS

TABLE OF CONTENTS (contd)

TABLE OF CONTENTS (contd)

LIST OF FIGURES

LIST OF FIGURES (contd)

LIST OF FIGURES (contd)

LIST OF TABLES

LIST OF TABLES (contd)

HIGH-PERFORMANCE BATTERIES FOR ELECTRIC-VEHICLE PROPULSION AND STATIONARY ENERGY STORAGE

Progress Report for the Period
October 1978 - March 1979

ABSTRACT

This report covers the research, development, and management activities of the programs at Argonne National Laboratory (ANL) and at subcontractors' laboratories on high-temperature batteries during the period October 1978 - March 1979. These batteries are being developed for electric-vehicle propulsion and for stationary energy-storage applications. The present cells, which operate at 400-500°C, are of a vertically oriented, prismatic design with one or more inner positive electrodes of FeS or FeS_2, facing electrodes of lithium-aluminum alloy, and molten LiCl-KCl electrolyte.

During this six-month period, cell and battery development work has continued at ANL, Eagle-Picher Industries, Inc., Gould Inc., and the Energy Systems Group of Rockwell International. Fabrication of a 40 kW-hr battery by Eagle-Picher for testing in an electric van is nearing completion. Cost and design studies for a Mark II electric-vehicle battery, which will have somewhat higher performance and use potentially low-cost materials and fabrication methods, have been conducted by all three subcontractors, and contracts are being negotiated for development of Mark II batteries. Conceptual design studies have continued at Rockwell International on a 100 MW-hr stationary energy-storage module. The present plan is to construct a module based on these designs for testing at the BEST (Battery Energy Storage Test) Facility. Work has also been in progress at the Carborundum Co., General Motors Research Laboratories, and various other organizations on developing materials and components for cells.

SUMMARY

Industrial Contracts

The three major subcontractors of the battery program are Eagle-Picher Industries, Inc., Gould Inc., and Rockwell International's Energy System Group.

In February 1978, Eagle-Picher was contracted to develop, design, and fabricate a 40 kW-hr electric-vehicle battery (designated Mark IA). The Mark IA battery will consist of two 20-kW-hr modules, each module having 60 multiplate cells connected in series and housed in a thermally insulated case. In the cell development phase of the Mark IA program, Eagle-Picher fabricated about 120 multiplate Li-Al/FeS cells of varying designs, which were tested at their own laboratories or ANL. Several problems were

encountered during the development phase of the program, including high cell resistance, loss of capacity during cycling, and poor wetting of the separator by the electrolyte; these problems were resolved through intensive efforts at Eagle-Picher and ANL. The test results from individual cells indicate that the Mark IA cells, which are presently being fabricated, should meet our performance and lifetime goals. According to the present schedule, the Mark IA battery will be completed and ready for testing by mid-May 1979.

To aid in developing the final design for the Mark IA battery, Eagle-Picher has fabricated a small (6 V) battery module which contains five Li-Al/FeS multiplate cells connected in series. This battery is presently being tested at ANL.

Gould Inc. is investigating electrode assembly techniques that are suitable for mass-production, including fabrication of electrodes by extrusion and powder rolling techniques and assembly with the active materials in the semi-charged state. In addition, a cell design has been developed to accomodate BN felt separators, which have the potential for lower cost than that of the previously used BN fabric separators. During this report period, Gould also tested about 20 experimental Li-Al/FeS bicells. Based on test results reported in the previous period, these cells had carbon, cobalt, and excess iron powder added to the positive electrode and a LiCl-KCl electrolyte with a LiCl content higher than that of the eutectic. These cells typically attained specific energies above 58 W-hr/kg at current densities of 5 to 80 mA/cm^2, and resistances of 2.5 mΩ (t=0 sec). The test data indicate that the near-term (1979-1981) performance goals for the electric-vehicle battery can be met or exceeded with the Li-Al/FeS system. Gould has recently prepared a cost and design study for the 50-kW-hr Mark II battery.

Rockwell International tested fourteen Li-Si/FeS electric-vehicle bicells. These cells showed significant improvements in performance when operated at high temperatures (>450°C) or when the LiCl-KCl electrolyte had a high LiCl content. In addition, construction of cells in the partially charged state (*i.e.*, substitution of Li_2Si for $FeSi_2$ in the negative electrode) increased the average cell voltage from 1.22 to 1.34 V at a discharge current density of 60 mA/cm^2. In other work, Rockwell has completed a balance-of-plant (BOP) cost analysis for the 100 MW-hr energy-storage battery described in the last report in this series, and found that the BOP cost, $80/kW-hr, was significantly above that of our goal of $45-55/kW-hr (1979 dollars). Studies are under way at Rockwell and ANL to discover modifications in the basic battery design that will lead to a lower BOP cost.

Cell and Battery Testing

ANL Cell Tests. Over the past six months, ANL has tested 22 engineering-scale Li-Al/FeS bicells fabricated at ANL. Four of these cells, designated M-series cells (pressed electrodes assembled charged; BN felt separators), were tested in a continuing effort to determine the effect on performance of the following: positive-electrode additive of Cu_2S or LiCl-rich electrolyte, and high positive-electrode loading (1.4 or 1.6 A-hr/cm^3). All but one of these cells operated for between 300 and 375 cycles. The test results indicated that both the Cu_2S additive and the LiCl-rich electrolyte improved the performance of the Li-Al/FeS cell. In addition, the use of a positive-electrode loading of 1.6 A-hr/cm^3 appeared to result in a somewhat better

performance. Two other Li-Al/FeS bicells, designated the R series (pressed electrodes assembled uncharged; BN felt separators), were tested to determine the effect of current collector material on cell performance. One of the cells had a nickel current collector; the other had a low-carbon steel current collector. Somewhat surprisingly, both of these cells are exhibiting about the same performance after over 110 cycles. Operation of these cells will continue in order to determine the long-term effects (>300 cycles) of these two current collector materials.

Carbon-bonded positive electrodes are being developed as an alternative to those made by pressing techniques, and MgO powder separators are being developed as an alternative to the BN fabric and felt that are currently used as separators. During this period, we tested one bicell with a carbon-bonded positive electrode (BN felt separator) and four bicells with MgO powder separators (pressed electrodes). The test results continue to indicate that the carbon-bonded positive electrode and MgO powder separator are viable alternatives to the components presently used in lithium/metal sulfide cells.

Two multiplate Li-Al/FeS cells with BN felt separators, one with a carbon-bonded positive electrode and the other with pressed electrodes, were tested at ANL; and their performance was compared with that of similar bicells having BN felt separators. To date the former cell has operated for 42 cycles, the other for 85 cycles. Even though not optimized for maximum performance, both of these multiplate cells have attained performance levels slightly better than those of similar bicells. A third multiplate cell, which has an MgO powder separator, has recently been started-up; test results will be reported in the next period.

Industrial Cell Tests. A number of the multiplate Li-Al/FeS cells fabricated by Eagle-Picher for the Mark IA program were tested at ANL to determine the effect of continued cycling after cell failure, operating temperatures of 420 to 475°C, and simulated driving conditions. These tests indicated the following: the Mark IA battery can continue to be cycled after some of the cells have shown a marked decline in coulombic efficiency; the optimum operating temperature for the Mark IA cell is 460-470°C; and the Mark IA cells should produce acceptable power under severe acceleration conditions without adverse effects to the cell.

During the developmental stage of the Mark IA program, it was discovered (1) that the Eagle-Picher multiplate cells were frequently failing due to swelling of the cell can which resulted in extrusion of active material from the positive electrode and (2) that the cell power was lower than that required by the Mark IA goals. For the former problem, intensive investigation at ANL revealed that the melting of the electrolyte in these cells resulted in a pressure surge that was largely dependent upon the available void space in the cell prior to melting of the electrolyte. For the Mark IA battery, this edge-wise force will be controlled by the amount of electrolyte added to the cells; the cell tray is also being designed to restrain this force. To increase the power of the Mark IA developmental cells, ANL made and then tested various design changes to the current collector, bus bar, lead ribbons, *etc.* However, the most effective measure resulted from adding a copper layer to the top of the Eagle-Picher cell to lower the resistance path between the negative bus bar and the intercell connectors. As a result of the design changes, the cells fabricated for use in the Mark IA should easily meet the power goals.

Battery Tests. A small (6 V) Li-Al/FeS battery fabricated by Eagle-Picher, which contains five multiplate cells connected in series, was tested in the laboratory and in a Volkswagen van at ANL. In the laboratory tests, this battery was operated for 58 cycles with less than 5% loss of capacity and 7.6% loss of energy. After laboratory testing, the battery was connected in series to the 144-V lead-acid battery in a Volkswagen van and road tested. At the end of one hour, the internal temperature of the 6-V battery had decreased from 475 to 470°C. (The full-scale 40 kW-hr Mark IA battery will heat up slowly during discharge.) The performance of the battery was as anticipated.

Cell Peformance and Lifetime Summary

A review was conducted of the electrical performance of six Li-Al/FeS bicells fabricated by ANL as well as five Li-Al/FeS bicells and ten Li-Al/FeS multiplate cells fabricated by Eagle-Picher. As expected, the highest specific energy was achieved by the multiplate cells; however, these cells had the highest decline in energy and capacity with cycling.

Two sets of ten status cells, one with BN felt and the other with MgO powder separators, are being built. These cells are being tested to obtain performance and lifetime data on at least six cells with an identical design.

Post-test examinations have been completed on 22 multiplate cells fabricated by Eagle-Picher and 20 bicells fabricated by ANL and industrial contractors. Of the 22 multiplate cells, the primary causes of cell failure were as follows: extrusion of active material from the positive electrode, seven cases; short circuit in feedthrough, four cases; metallic deposits in the separators, three cases; and equipment malfunction, three cases. Measures to correct these problems are being sought. Post-test examination of the bicells indicated that the major causes of cell failure in the past--extrusion of active material, cutting of separators by current collector, and cell assembly difficulties--appear to have been resolved by modifications in cell design and better quality control.

Cell Development

Engineering modeling studies are being conducted at ANL with the objective of developing empirical equations that relate cell performance to the physical and chemical characteristics of the cell and the mode of cell operation. Very general equations have been developed to fit FeS and FeS_2 bicells and multiplate cells; the coefficients in the equations were determined by multiple regression analysis. Operating and performance data of 26 cells were used to develop the model, and data from a second group of 16 cells were used as a subsequent check of the model. Good agreement has been obtained between predicted and actual cell performance. The model will be very useful in the optimization of the electric-vehicle cell design.

Small-diameter ($\sim$3 mm) reference electrodes are being developed for polarization measurements in engineering cells and for basic electrochemical investigations. Long-term stability tests have been completed on five electrode systems--Li-Al/Li^+, Li-Bi/Li^+, Ni/$Ni_3S_2/S^=$, Ag/$Ag_2S/S^=$, and Ag/AgCl--and the Ni/Ni_3S_2 system was found to be the most suitable.

Measurements will be made with reference electrodes in three sizes of cells: large (~100 A-hr) and intermediate-scale (5-15 A-hr) prismatic cells, and small tubular cells.

Cell tests are in progress to optimize the performance of the Li-Al/FeS cells. Studies have been conducted on 11.3 A-hr Li-Al/6.5 A-hr FeS cells containing the following amounts of Cu_2S additive to the positive electrode (in wt %): 0, 5, 10, and 20. The test results indicated that increasing the Cu_2S concentration in the positive electrode increased its utilization. In addition, at current densities of 100 to 200 mA/cm^2, the positive-electrode utilization decreased only slightly with increased current density.

Optimization studies were also conducted on engineering-scale cells. The utilization of four M-series cells, which have initial electrolyte volumes of 0.39 to 0.49 at full charge, was measured at current densities of 20 to 120 mA/cm^2, and the cell with the highest electrolyte volume was found to have the least dependence upon current density. In general, the resistance of ANL cells was found to increase as the depth of discharge was increased (from 3.1 to 4.5 mΩ).

Materials and Components Development

Electrode Development. Investigations are under way on the formation of agglomerated Li-Al in the center of the negative electrode during the discharge of multiplate FeS cells; this agglomeration is believed to be partly responsible for the marked decline in capacity with cycling of these cells. For these studies, we are using cells having small working electrodes of solid aluminum and large counter electrodes of porous Li-Al to eliminate any effects from metal sulfide. Results of these studies will be reported in the next period. In other work on the development of negative electrodes, we investigated the effect on performance of the addition of 15 wt % Zn to Li-Al electrodes; no improvement in performance was observed after 200 cycles of the Li-Al-Zn electrode. Next, indium additive will be evaluated in Li-Al electrodes.

The cell chemistry of the positive electrode (FeS and FeS_2) is being studied in cyclic-voltammetry experiments, small-cell tests, and out-of-cell studies.

For the FeS electrode studies, two 2 A-hr Li-Al/1 A-hr FeS cells (eutectic electrolyte) were operated to determine the potential at which $LiK_6Fe_{24}S_{26}Cl$ (J phase) forms during charge and discharge. Preliminary results indicate that J phase transforms to FeS at 1.6 V during charge. Cyclic voltammetry studies were completed on the FeS electrode in three different electrolytes--LiCl-KCl eutectic, LiCl-rich (*i.e.*, 63.8 to 74.4 mol %) LiCl-KCl, and LiCl-LiF-LiBr--and at temperatures of 400 to 500°C. The results obtained in the LiCl-KCl eutectic are consistent with the finding that J phase forms at the end of charge and also indicate that increasing the temperature improves the reaction kinetics of the FeS electrode. The results obtained with the LiCl-rich system indicate that some FeS is being formed at the end of charge, and that the charge and discharge electrode kinetics of the FeS electrode are improved as the LiCl content of the electrolyte is increased above that of the eutectic. The results obtained with the

LiF-LiCl-LiBr system indicate that X phase (Li_2FeS_2) and FeS are formed during cycling. Thermodynamic calculations were used to determine the cell potentials at which phase transitions occur in a cycled FeS cell with eutectic electrolyte.

In studies of FeS_2 electrodes, powders of Li_2S, Li_2FeS_2, Fe and FeS_2 were equilibrated with LiCl-KCl molten salt at 450°C; and the products were examined to identify the phases present. The information from this experiment was then used to further refine our understanding of the Li-Fe-S phase diagram presented in the last report of this series. In a continuing effort to understand the electrochemistry of the FeS_2 electrode during charge, three small cells were cycled at a current density of 25-30 mA/cm^2 for ten cycles and then cell operation was stopped after trickle charging at a selected cutoff voltage (1.64 V, 1.786 V, and 1.85 V, respectively) for about 18 hr. The results indicated that it is not possible to form FeS_2 at a potential of 1.76 V, which is the emf observed for the upper voltage plateau in Li-Al/FeS_2 cells. In further studies, one of the above three cells was cycled at a current density of 2 mA/cm^2; this study indicated that the Li-Fe-S phase diagram is more complex than previously thought, and that there may be two forms of Z phase ($Li_3Fe_2S_4$) both of which can be charged to FeS_2.

Designing the thermal management of a cell requires knowledge of the entropic heat effects, and hence of the cell reactants and products. In cell-chemistry studies, estimated values were calculated for the absolute entropies of X phase (Li_2FeS_2), J phase ($LiK_6Fe_{24}S_{26}Cl$), and Z phase ($Li_3Fe_2S_4$), which are not available in the literature. These estimates were made by established procedures. Good agreement was found between the calculated values and those obtained from emf *vs.* temperature curves from experimental cells. In addition, the calculated entropic heating of an Li-Al/FeS cell based on these estimates agreed with values that were obtained from a cell that was designed specifically to measure heat balances.

Separator Development. Carborundum Co. delivered a shipment of BN felt sheets to ANL. The physical properties of this material were then assessed before it was used in cells.

Stress-strain measurements were made on BN fabric and felt to estimate the thickness of the separator during cell operation. At stresses of 210-245 kPa (30-35 psi), the pressure at which FeS pellets have been found to flow significantly, the percent compression was found to be 40% for the fabric and 60% for the felt. Similar measurements will be made at higher stress levels.

Four separator materials--MgO powder, BN felt, Y_2O_3 sintered ceramic, and MgO sintered ceramic--were evaluated in experimental Li-Al/FeS cells. The MgO powder separator was prepared by a new, potentially low-cost casting technique; the cell having this type of separator was found to have excellent performance in comparison with previously operated cells having MgO powder separators (vibratory loaded). The results of the separator tests also indicated that MgO sintered ceramic could be used successfully as a separator material in Li-Al/FeS cells. Three cells were operated with BN felt separators; one was treated with a wetting agent ($LiAlCl_4$) and the other two were not given the usual stabilization procedure (*i.e.*, bonds not

completely converted from B_2O_3 to BN). The test results indicated that BN felt treated with the $LiAlCl_4$ wetting agent and BN felt with unstabilized BN bonds are suitable for testing in engineering cells.

Current Collector Development. In the development work on current collectors, preliminary characterization has been completed on the following iron-base alloys for FeS electrodes: ANL-5-0 (Fe-5 wt % Mo), ANL-10-20 (Fe-10 wt % Mo-20 wt % Ni), and ANL-15-30 (Fe-15 wt % Mo-30 wt % Ni). Measurements of the resistivity, oxidation potential, and hardness showed that these properties increased as the amount of alloying element is increased. The first two of the above alloys (ANL-5-0 and ANL-10-20) were subsequently tested in experimental cells, and both materials showed promise as a low-cost, long-lifetime current collector in FeS electrodes.

In-cell tests are also being conducted on other candidate materials for current collectors and frames for metal sulfide electrodes. For these tests, nine 50 A-hr cells were operated at 450°C--three FeS_2 cells with positive-electrode current collectors and frames of Hastelloy B and six FeS cells with collectors and frames of nickel. Of the six FeS cells, four were assembled semi-charged and two charged; the test results indicated that nickel has the necessary corrosion resistance for long life in FeS electrodes. The corrosion rates of the Hastelloy B in the FeS_2 electrodes was found to be unacceptably high. Hastelloy B appears unsuitable for application in FeS_2 cells, but remains a candidate for FeS cells.

Static corrosion tests are being conducted to evaluate electronically conductive ceramics as coating materials for metallic current collectors in FeS_2 electrodes. The following materials were tested for 300 hr at 500°C in FeS_2 plus LiCl-KCl: TiN, TiC, and TiB_2 prepared by hot-pressing; TiN, TiC, TiCN, and TiB_2 chemically vapor deposited on AISI 1008 steel; and MoS and $MoSi_2$ deposited on AISI 1008 steel by rf sputtering. The test results indicated that only the hot-pressed TiN and TiC were chemically stable in the FeS_2 environment. The poor quality of the coatings was thought to be the reason for their failure. Since it is difficult to obtain a defect-free thin coating, attempts are being made to fabricate monolithic ceramic (TiN and TiC) current collectors that can be used for in-cell testing.

Systems Design and Analysis

Early in 1978, a reference design of a 100 MW-hr energy-storage battery having Li-Al/FeS or Li-Si/FeS cells was devised as a result of a joint effort between ANL and Rockwell International. However, investigations indicated that the cost of the battery hardware (exclusive of cells) and installation would be $80/kW-hr, which is well over the goal of $45-55/kW-hr. To reduce this cost, several changes in the battery design have been recommended. One of the major suggested changes is to increase the cell size from 2.5 to 30 kW-hr; the dimensions for this large cell would be about 2.4 m x 30 cm x 22 cm. In the modified 100 MW-hr battery design, 168 such cells would be electrically connected to form a module having an energy capacity of 5 MW-hr. Ten such modules would be connected in series to form one of two 50 MW-hr banks, each of which would have an ac-dc converter.

In studies of electric-vehicle battery systems, the thermal properties of the 6-V battery fabricated by Eagle-Picher were investigated. Cycling of this battery in the laboratory showed that a slow accumulation of hydrogen within the vacuum annulus had raised the pressure above the level required to maintain good insulating properties. For subsequent laboratory tests, the pressure of hydrogen was reduced to an acceptable level, about 0.026 Pa (2×10^{-4} torr), by the use of an ion-pump or a room-temperature getter that was selective for hydrogen. Typical heat-loss rates at a pressure of 0.026 Pa were found to be 160 W with a battery operating temperature of 465°C. These results reinforce our expectation of achieving the goal of a 400-W heat loss for the 40 kW-hr Mark IA battery. In other studies, two Eagle-Picher cells at operating temperature were crushed and the contents exposed to air; no signs of fire or other chemical reactions were observed.

Calcium/Metal Sulfide Battery Development

The objective of this program is to develop calcium alloy/metal sulfide cells for inexpensive, high-performance batteries. The electrodes and electrolyte for these cells are being developed and optimized through cyclic-voltammetry studies, cell tests, and out-of-cell experiments.

In out-of-cell experiments, the solubility of CaS (one of the active materials in the positive electrode of uncharged calcium cells) in LiCl-NaCl-$CaCl_2$-$BaCl_2$ electrolyte was found to be a factor of ten lower than that of Li_2S in LiCl-KCl electrolyte (lithium cell), and the vaporization rate of sulfur from CaS-FeS_2 mixtures in the quaternary electrolyte was found to be significantly lower than that of Li_2S-FeS_2 mixtures in LiCl-KCl.

Tests were conducted on small-scale cells having positive electrodes of either NiS_2, FeS_2, or FeS_2-CoS_2. The maximum utilizations of the NiS_2 and FeS_2 electrodes were satisfactory (64%), and the CoS_2 additive improved the utilization of the FeS_2 electrode by 8%. Voltammetry studies of these three metal disulfide electrodes in an electrolyte of LiCl-KCl and LiCl-NaCl-$CaCl_2$-$BaCl_2$ indicated that the FeS_2 electrode with the quaternary electrolyte and the NiS_2 electrode with the binary electrolyte should exhibit the best performance characteristics.

Two engineering-scale cells (theoretical capacity, 214 A-hr) were tested during this report period. One of these was a $Ca_2Si/Ni(Co)S_2$ cell that was operated for 115 cycles and achieved a specific energy of 61 W-hr/kg at the 20-hr rate. The other was a $Ca_2Si/Fe(Co)S_2$ cell that is still operating after 30 cycles; the specific energy of this cell is the highest of any calcium cell built to date--78 W-hr/kg at the 24-hr rate. Both of these cells showed a significant decline in specific energy with cycling; efforts are in progress to resolve this problem.

I. INTRODUCTION

Lithium/metal sulfide batteries are being developed by Argonne National Laboratory (ANL) and its subcontractors for use as (1) the energy source for electric-vehicle propulsion, and (2) stationary energy-storage applications such as load leveling on electric utility systems or storage of energy produced by solar, wind, or other intermittent sources. The widespread use of electric vehicles would conserve petroleum fuels, since the electrical energy for charging the batteries could be provided by coal, nuclear, hydroelectric, or other energy sources; a side-benefit would also be realized in decreased air pollution in congested urban areas. The use of stationary energy-storage batteries for load leveling could save petroleum by reducing the need for gas turbines to meet peak power demands and by facilitating the use of alternative energy sources.

The major requirements for an electric-vehicle battery are high specific energy (W-hr/kg), high volumetric energy density (W-hr/L), and high specific power (W/kg). Economic considerations require a minimum battery lifetime of about 3 yr (~1000 deep discharge cycles or equivalent) and a cost goal of about $50-60/kW-hr.* Stationary energy-storage batteries have somewhat less stringent specific-energy and specific-power requirements, but this application demands a longer lifetime (~10 years and 3000 cycles) and a cost goal of $45-55/kW-hr. As a result of these requirements, considerably different approaches are being taken in the designs of cells and batteries for these two applications.

The current program on the electric-vehicle battery involves the development, design, and fabrication of a series of full-scale lithium/metal sulfide batteries, designated Mark IA,† II, and III. The main purpose of the Mark IA battery is to evaluate the technical feasibility of the lithium/metal sulfide system as an electric-vehicle battery and to resolve interfacing problems among the battery, the vehicle, and the charging system. The Mark II battery has somewhat higher performance goals than Mark IA, but the major objective is to develop designs and materials that will permit low-cost mass manufacturing methods. It is anticipated that the Mark II battery may have commercial potential for certain limited applications. The Mark III battery is planned as a high-performance prototype suitable for evaluation and demonstration in a passenger automobile. The performance and lifetime goals for the Mark IA, II, and III batteries are presented in Table I-1.

Work is nearing completion at Eagle-Picher Industries on the fabrication of the Mark IA battery, which is scheduled for laboratory and mobile testing in an electric van in 1979. This battery consists of two 20 kW-hr modules, each containing 60 cells. Although various technical problems have been encountered in the design and fabrication of the cells and the insulated cases for the Mark IA battery, there appear to be no major obstacles to the completion of this program. An effort has also been initiated on the Mark II

---

*Cost given in 1979 dollars throughout this report.

†The original plan was to develop a series of Mark I batteries (IA, IB, and IC); however, a decision has been made to proceed directly from Mark IA to Mark II in the development program.

Table I-1. Program Goals for the Lithium/Metal Sulfide Electric-Vehicle Battery

Goal	Mark IA	Mark II	Mark III
Specific Energy, W-hr/kg[a]			
Cell (Average)	80	125	160
Battery	60	100	130
Energy Density, W-hr/liter			
Cell (Average)	240	400	525
Battery	100	200	300
Peak Power, W/kg[b]			
Cell (Average)	80	125	200
Battery	60	100	160
Battery Heat Loss, W[c]	400	150	125
Lifetime			
Deep Discharges	200	500	1,000
Equivalent Kilometers	32,000	95,000	240,000
Equivalent Miles	20,000	60,000	150,000

[a] Calculated at the 4-hr discharge rate.

[b] Peak power sustainable for 15 sec at 0 to 50% state of discharge; at 80% discharge, the peak power is 70% of the values shown.

[c] The values shown represent the heat loss of the battery through the insulated case; under some operating conditions, additional heat removal may be required.

battery program. Late in 1978, three cost and design studies on the Mark II battery were conducted by Eagle-Picher Industries, Gould Inc., and the Energy Systems Group of Rockwell International. The next phase of the Mark II program, which is now under way, involves the development, design, and fabrication of a 50 kW-hr battery by each of the two contractors (Eagle-Picher and Gould).

Most of the recent effort on stationary energy-storage batteries has consisted of conceptual design and cost studies, which were started in 1978 as a joint study by Rockwell International and ANL. A reference design of a 100 MW-hr battery module utilizing either Li-Si/FeS or Li-Al/FeS cells was developed during 1978. Cost estimates of the battery hardware and installation, however, have resulted in a redirection of the effort to develop more cost-effective battery designs. The long-range objective of this work is to develop a 5-6 MW-hr battery module, which will be tested in the BEST

(Battery Energy Storage Test) facility. This facility is a joint undertaking by the U.S. Department of Energy, the Electric Power Research Institute, and the Public Service Company of New Jersey to provide for the testing of various types of batteries on an electric-utility system.

The battery cells that are currently under development consist of Li-Al or Li-Si negative electrodes, FeS or FeS_2 positive electrodes, a separator to provide electrical isolation of the electrodes, and molten LiCl-KCl electrolyte. The melting point of the electrolyte at the eutectic composition (58.2 mol % LiCl) is 352°C, and the cells are operated at temperatures between 400 and 500°C. The cells now being developed for the Mark IA and Mark II electric-vehicle batteries have Li-Al negative electrodes and FeS positive electrodes; electric-vehicle cells for the Mark III or other future batteries will probably have FeS_2 positive electrodes and lithium alloy negative electrodes. Stationary energy-storage cells will consist of Li-Al or Li-Si negative electrodes and FeS positive electrodes.

The overall electrochemical reaction for the Li-Al/FeS cell can be written as follows:

$$2LiAl + FeS \underset{\longleftarrow}{\overset{2e^-}{\longrightarrow}} Li_2S + Fe + 2Al \qquad (1)$$

The theoretical specific energy for this reaction is about 460 W-hr/hg, and the voltage *vs* capacity curve has a voltage plateau at about 1.3 V. The reaction is actually more complex than shown; for example, an intermediate compound, $LiK_6Fe_{24}S_{26}Cl$ (J phase), is formed through an interaction with the KCl in the electrolyte. The overall reaction for the Li-Al/FeS_2 cell can be written as:

$$4LiAl + FeS_2 \underset{\longleftarrow}{\overset{4e^-}{\longrightarrow}} 2Li_2S + Fe + 4Al \qquad (2)$$

The theoretical specific energy for reaction (2) is about 650 W-hr/kg. The voltage *vs* capacity curve has two voltage plateaus at approximately 1.6 and 1.3 V, respectively. Some Li-Al/FeS_2 cells are designed to operate only on the 1.6 V plateau and are referred to as "upper plateau" cells. Reaction (2) also involves several intermediate compounds (generally ternary compounds of lithium, iron, and sulfur). Although cells having FeS_2 electrodes offer a higher specific energy and voltage than those with FeS electrodes, the higher sulfur activity of FeS_2 leads to high corrosion rates and long-term instability of the electrode.

A key cell component is the electrode separator, a porous material that provides electrical isolation of the electrodes but permits the migration of lithium ions between the electrodes. Separator materials currently being used include boron nitride (BN) fabric, BN felt, and powders such as MgO. In most cell designs, it is also necessary to use screens or other structures to retain particulate material within the electrodes. To enhance the electronic conductivity of the electrodes, metallic current collectors are used to provide a low-resistance current path between the active material and the electrode terminal.

The cell designs currently being developed for the Mark IA, Mark II, and stationary energy-storage batteries all have a prismatic, multiplate configuration with two or more positive electrodes and facing negative electrodes. The cells can be fabricated in a charged, uncharged, or partially charged state by using various combinations of reactants and products in the electrodes. Both the positive and the negative electrodes are normally fabricated by cold- or hot-pressing methods.

A major objective of this program is to transfer the technology to interested commercial organizations as it is developed, with the ultimate goal of a competitive, self-sustaining industry for the production of lithium/metal sulfide batteries. To this end, most of the cell and battery development, design, and fabrication is subcontracted to industrial firms, which include Eagle-Picher Industries, Gould Inc., and the Energy Systems Group of Rockwell International. The Carborundum Co. is involved in the preparation of BN separator materials and the development of production processes for these materials. Other contractors currently participating in the program include the General Motors Research Laboratories, ESB, Inc., Illinois Institute of Technology, the University of Florida, and United Technologies Corp.

The in-house research and development program at ANL consists of supporting cell-chemistry studies, materials development and evaluation, cell and battery development, cell and battery testing, battery design, and commercialization studies. Facilities are now available at ANL for laboratory and on-board testing of electric-vehicle batteries and lifetime testing of cells. Another small effort at ANL is directed toward the development of calcium alloy/metal sulfide cells, which are believed to have a potential for low cost in mass production.

II. INDUSTRIAL CONTRACTS

The ultimate goal of the program at ANL is the development of a competitive, self-sustaining industry for the production of electric-vehicle and stationary energy-storage batteries. To this end, industrial firms have been invited to participate in the program, with approximately 50% of the current funding directed to industrial subcontracts. Three firms--Eagle-Picher Industries Inc., Gould Inc., and the Energy Systems Group of Rockwell International--are developing manufacturing procedures and fabricating test cells. Other contractors are developing cell materials and components.

A. Eagle-Picher Industries, Inc.

In February 1978, Eagle-Picher was contracted to develop, design, and fabricate the Mark IA battery. The technical goals for the Mark IA are given in Table II-1. On the basis of previous test results from Li-Al/FeS and Li-Al/FeS_2 bicells* (ANL-78-94, pp. 98-102), Eagle-Picher selected a multiplate cell design (three positive and four negative electrodes) for this battery.

Table II-1. Technical Goals for the Mark IA Battery

Battery Characteristics	Goals
Energy Output,[a] kW-hr	40
Power Output,[b] kW	30
Maximum Weight, kg	667
Maximum Volume, L	400
Specific Energy,[a] W-hr/kg	60
Energy Density,[a] W-hr/L	100
Operating Temperature, °C	400-500
Maximum Heat Loss, W	400
Battery Voltage, V	144
Cycle Life[c]	200

[a]Discharge to 1.0 V/cell at the 4-hr rate.

[b]15-sec pulse at 50% discharge.

[c]To 20% loss of the design capacity.

*A central positive electrode and two facing negative electrodes.

1. Cell Development for Mark IA

In the cell development phase of the Mark IA program, Eagle-Picher fabricated about 120 multiplate cells, which were tested at their own laboratories or ANL.* The electrodes for these cells had many design variables, including 0 to 20 wt % Cu_2S added to the positive electrode,† positive electrode‡ theoretical capacities of 355 to 448 A-hr, and lithium-to-sulfur ratios of 0.89 to 1.29. Other cell design variables included positive current collector design and material (iron and nickel), LiCl content of the electrolyte (eutectic and 67 mol % LiCl),† and particle retainer material (Y_2O_3 or ZrO_3 cloth on both electrodes, Y_2O_3 cloth on the positive electrode only, and no retainer for either electrode).

Several problems were encountered during the development phase of the program, including high cell resistance, loss of capacity during cycling, and poor wetting of the separator by the electrolyte. These problems have been resolved through intensive efforts both at ANL and Eagle-Picher. Performance data on the developmental cells tested during the past six months are given in Appendix A.1. Based on the results of these tests, Eagle-Picher selected the final design for the cells to be used in the Mark IA, and began fabrication of these cells.

The Mark IA cell has dimensions of 19 x 18 x 3.9 cm and a weight of about 4 kg. The negative electrodes consist of 46 wt % Li-Al (theoretical capacity of about 440 A-hr) and have dimensions of 16 x 17 x 0.57 and 0.27 cm. The positive electrodes consist of FeS and 15 wt % Cu_2S (theoretical capacity of 410 A-hr) and have dimensions of 16 x 17 x 0.32 cm. Other cell components include current collectors of AISI 1010 carbon steel, separators of 0.175-cm thick BN cloth, particle retainers of Y_2O_3 felt for the positive electrode and Type 304 stainless steel screen (200 mesh) for both the positive and negative electrodes, a crimp-type electrical feed-through with a BN powder seal, and a cell container of AISI 1008 and 1010 carbon steel with a material thickness of 0.57 cm.

To date, 81 acceptable cells have been fabricated for use in the Mark IA battery, which requires 120 cells plus 12 spares. Testing of a group of recent Mark IA cells revealed an unacceptably low resistance at room temperature of some of the cells. Metallographic examination of cell sections at ANL showed that this problem was caused by overcharging the cells during the electrolyte filling and initial cycling operations. Corrective actions have been taken by Eagle-Picher, and the problem appears to be solved. Additional cells are being fabricated and a high yield of acceptable cells is excepted.

2. Insulating Cases for Mark IA

Eagle-Picher was also contracted by ANL to design and fabricate the thermally insulating cases and other hardware required for the Mark IA cells; the Mark IA battery will consist of two 20 kW-hr modules, each housed

* Those cells tested at ANL are reported in Section III.C.

† Added to eliminate the formation of J phase, which causes poor electrical performance.

‡ Limits cell capacity.

in a thermally insulating case. Eagle-Picher subsequently contracted Thermo Electron Corp. and Budd Co. to fabricate the two Mark IA cases and a prototype case. The final design chosen for these cases consists of double-walled metal (Inconel 718) with multilayered foil in the evacuated space; the basic case design is illustrated in Fig. II-1.

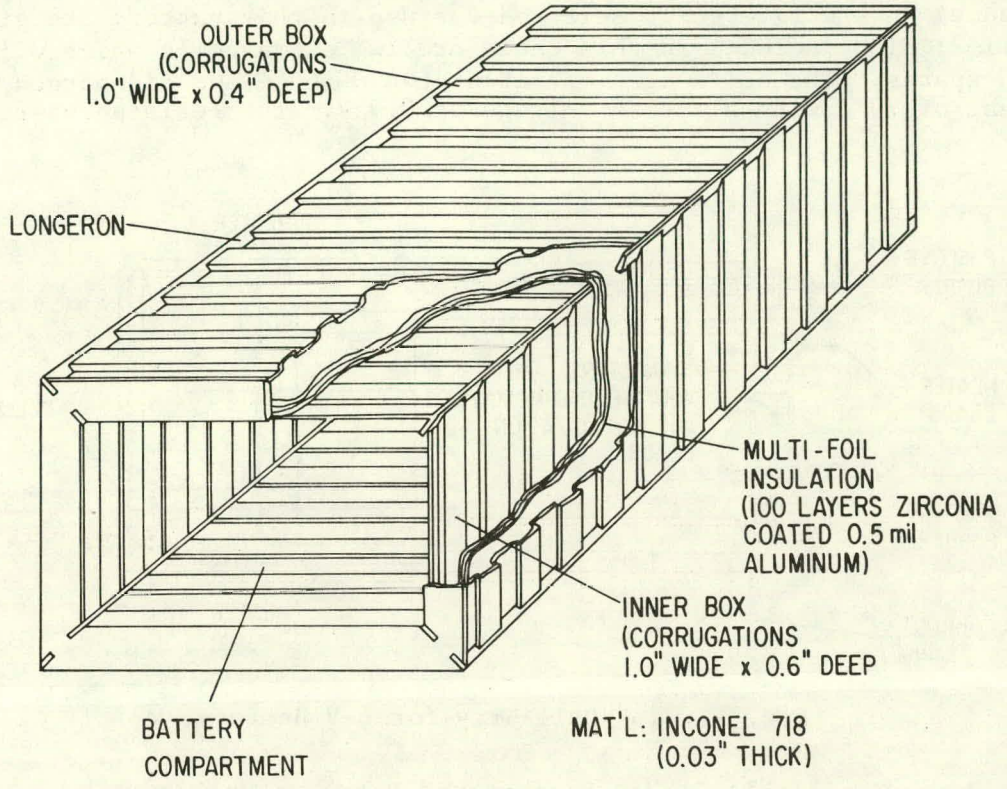

Fig. II-1. Insulating Case for Mark IA Battery

All three cases have been fabricated, and have undergone thermal testing; the prototype case was also subjected to vibration tests. In one of the Mark IA cases, a leak was discovered in the inner of its two walls; this defect is extremely difficult to repair. The current plan is to ship the cases to ANL for any necessary repairing of leaks, and bakeout and pumpdown of the vacuum annulus in each case. Eagle-Picher will then install the cells and hardware to complete the battery. According to the present schedule, the Mark IA battery will be completed by mid-May 1979.

3. Construction of a Small (6-V) Battery

Eagle-Picher* has fabricated a 6-V (1.8 kW-hr) Li-Al/FeS battery to aid in developing the final design for the Mark IA battery. This small battery has five Mark IA cells connected in series, which have been installed in a cell tray (see Fig. II-2) and housed in a thermally insulating case similar in design to that of the Mark IA case. Performance data (capacity and resistance) on the five cells selected for use in this battery are given in Table II-2; also included in this table are two extra cells which will be used as spares. The cells were operated at 450-465°C and discharged at a current of 70 A with a cutoff voltage of 0.9 V. The resistances for these

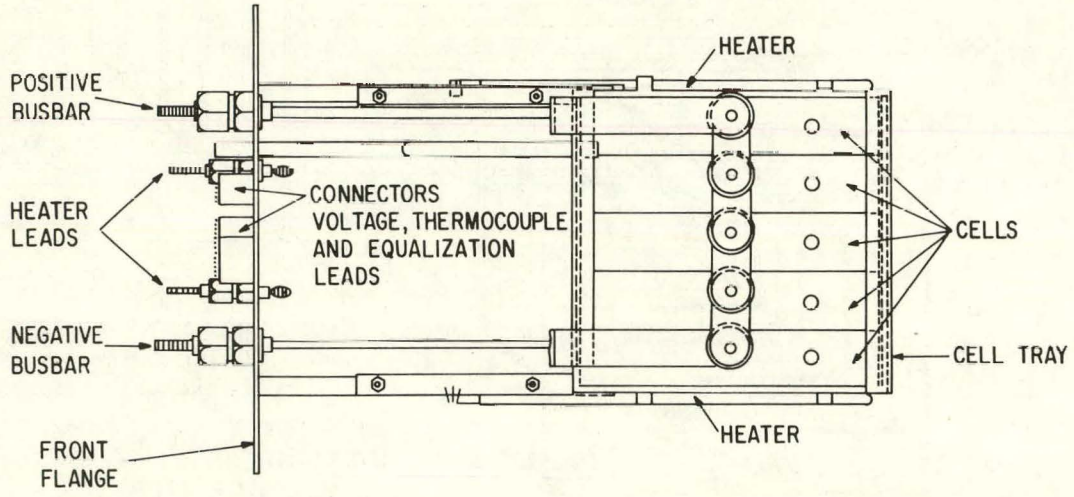

Fig. II-2. Cell Tray for 6-V Battery

Table II-2. Performance Data[a] on Cells Chosen for 6-V Battery

Cell No.	Capacity, A-hr	Cell Resistance, mΩ
EPMP-7-133	339	1.61
EPMP-7-128	340	1.71
EPMP-7-130	345	1.55
EPMP-7-131	334	1.50
EPMP-7-129	345	1.54
EPMP-7-127	335	1.63
EPMP-7-134	339	1.64

[a]Measured on 5th cycle.

* Thermo Electron and Budd were contracted by Eagle-Picher to assist in the development and fabrication of the 6-V module.

cells are relatively high (1.5-1.71 mΩ), which reflects the state of the art for multiplate cells at the time of the assembly of the 6-V battery. However, recent cooperative efforts with ANL (discussed in Section III.C) have resulted in the development of multiplate cells with a lower resistance for the Mark IA cells.

After assembly of the case for the 6-V battery, thermal tests at Thermo Electron Corp. revealed a case heat loss of about 97 W with an internal temperature of 490°C. Upon completion of the thermal tests, the 6-V battery was completely assembled and operated at Eagle-Picher for 10 cycles. Performance data and heat loss during operation are given in Table II-3. As can be seen, the heat loss increased considerably during battery operation; this effect was due to a loss of vacuum in the annulus. Vibrational tests (4-hr discharge rate at up to 1.5 g and 5 to 50 Hz) were conducted on the battery during cycle 5 at a discharge current of 50 A; no adverse effects of vibrations on electrical performance were found. Upon completion of the above tests, the battery was cooled and shipped to ANL for testing.*

Table II-3. Performance Data on 6-V Battery

	Operating Conditions		Performance		Heat
Cycle No.	Temp., °C	Current, A	Cap., A-hr	Energy, W-hr	Loss, W
0	400	-	-	-	120
0	450	-	-	-	189
1	449	50	343	2060	200
2	451	50	349	2095	190
3[a]	447	50	358	2150	190
4	451	48	329	1975	186
5[b]	449	50	341	2040	206
6	453	50	350	2100	221
7	453	48	332	1980	231
8	443	48	321	1915	233
9	452	130, 40	335	2030	239
10	453	135, 55	367	2180	220

[a]Discharged to a voltage of 2.53 V.

[b]Vibration tests.

* The results of the battery tests are given in Section III.D.

B. Gould Inc.

The program at Gould is directed toward the fabrication and testing of Li-Al/FeS cells; the development of electrode fabrication processes suitable for mass manufacturing, and the expansion and improvement of cell testing facilities. The improvements in Li-Al/FeS cell performance achieved by the Gould cells over the two years prior to this report period are illustrated in Fig. II-3; all the cells in this figure are bicells except for the multiplate cell G111-2.

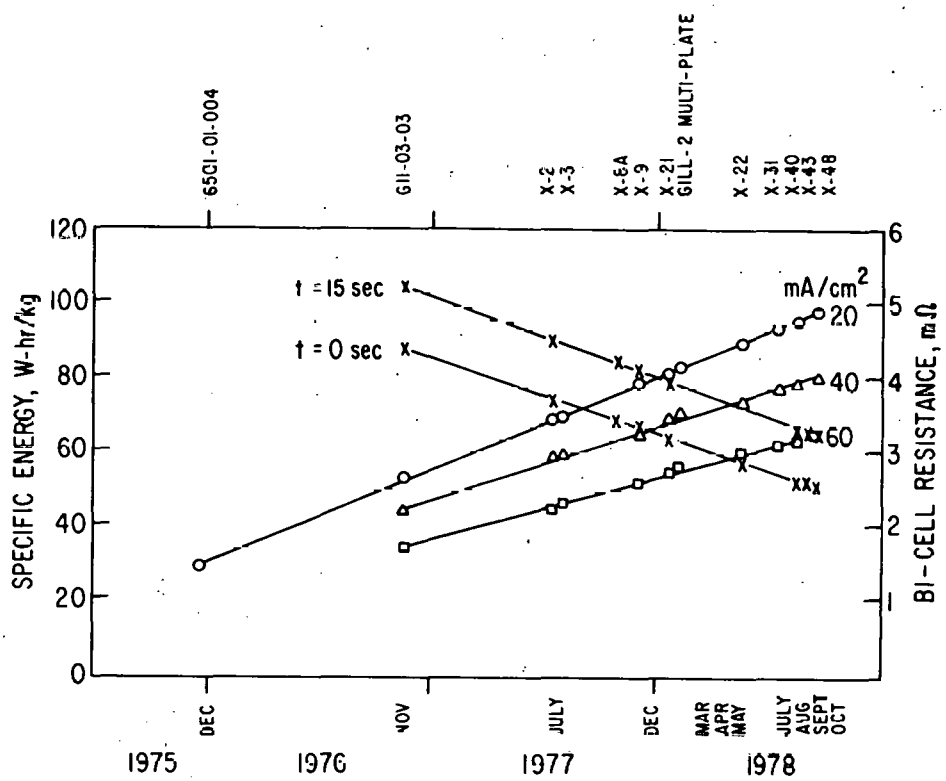

Fig. II-3. Performance of Li-Al/FeS Gould Cells Tested over the Past Two Years

1. Cell Development

One of the early priorities at Gould was the development of electrode designs that are suitable for mass-production. Testing of the first few X-series cells, which were built during September 1977 (see ANL-78-94, p. 196), indicated that cells could be operated with very simple, homogeneous slab electrodes with no detrimental effects on performance. Subsequently, Gould investigated potentially high-rate manufacturing techniques such as extrusion and powder rolling for the production of electrodes. In early 1978, Alcoa produced Li-Al alloy negative electrodes (discharged composition) by the extrusion technique, but these electrodes did not perform satisfactorily, probably on account of certain microstructural peculiarities. At present, experiments on positive electrode extrusion are in progress, and cold- and hot-powder rolling of both electrodes is being evaluated.

Recently, several experimental bicells have been fabricated with the electrode materials half-charged. This method of electrode assembly offers several advantages over assembly with uncharged or charged active materials. For example, the positive electrode of the half-charged cell can be less porous (*i.e.*, higher capacity loading) or thinner than that of the uncharged cell. The advantage of thinner electrodes is that they make cell assembly easier and produce compressive rather than tensile forces on the electrode separator, which is delicate and easily deformed during startup. Testing of the half-charged cells is under way.

Lithium-aluminum reference electrodes have been developed at Gould to identify the capacity-limiting electrode in an engineering cell by monitoring polarization; the reference electrodes could also aid in tracing the sources of high internal cell resistance in a cell by using well-defined current-interruption data at 0 and 15 sec.

A major task during this report period was the development of cell designs that can accomodate BN felt separators; this material has the potential for lower cost than that of the BN fabric previously used as a separator material. Since BN felt was not initially available in significant quantities from other sources, early felts were fabricated from scrap BN cloth fibers at Gould. The performance of bicells with such separators was excellent, although mechanical design problems usually resulted in early cell failures due to localized short circuits. Frozen (room temperature) cell resistances of 10^5 to 10^6 Ω were obtained (excluding localized short circuits), which are significantly higher than the 10^2 to 10^3 Ω observed with earlier bicells having BN cloth separators. Felt fabrication was time consuming, and this procedure was discontinued as soon as BN felt separators became available from Carborundum Co. (see Section II.D). The first problem in the use of felt sheet separators is material containment at the electrode perimeter. A simple 'U' channel of metal around the positive electrode perimeter was tested out in 11 experimental cells, but the fragile BN felt was easily crushed against the metal channel, resulting in short circuits. Subsequently, the positive electrode was wrapped with a flexible metal screen and then the separator was inserted; this technique proved to be successful and is employed in cells currently on test and being fabricated. Efforts are in progress to achieve a better definition of felt characteristics acceptable for cell construction.

2. Cell Testing

Over the past six months, about 20 experimental Gould Li-Al/FeS bicells were tested, and performance data for these cells are given in Appendix A.2. One of the more important performance parameters for electric-vehicle cells is specific energy, which is affected by the utilization of the active material in the limiting electrode. Cell testing during the last report period (ANL-78-94, p. 49) indicated that a Li-Al/FeS cell having carbon, cobalt, and excess iron powder added to the positive electrode and a LiCl-KCl electrolyte with a high LiCl content (>62.8 mol % LiCl) has a much higher positive electrode utilization than that of a baseline Li-Al/FeS-Cu_2S

cell. Consequently, the cells tested during this period had the above additives and LiCl-rich electrolyte. Figure II-4 shows the specific energy achieved by five such cells at current densities of 5 to 80 mA/cm^2. As can be seen in this figure, all of these cells achieved specific energies of >58 W-hr/kg, the highest being achieved by X-56A (93 W-hr/kg).* The longest operating cell tested in this report period was X-45, which operated for 123 cycles at the 3.5-hr rate before short-circuiting; the capacity decline for X-45 over its lifetime was only about 5%.

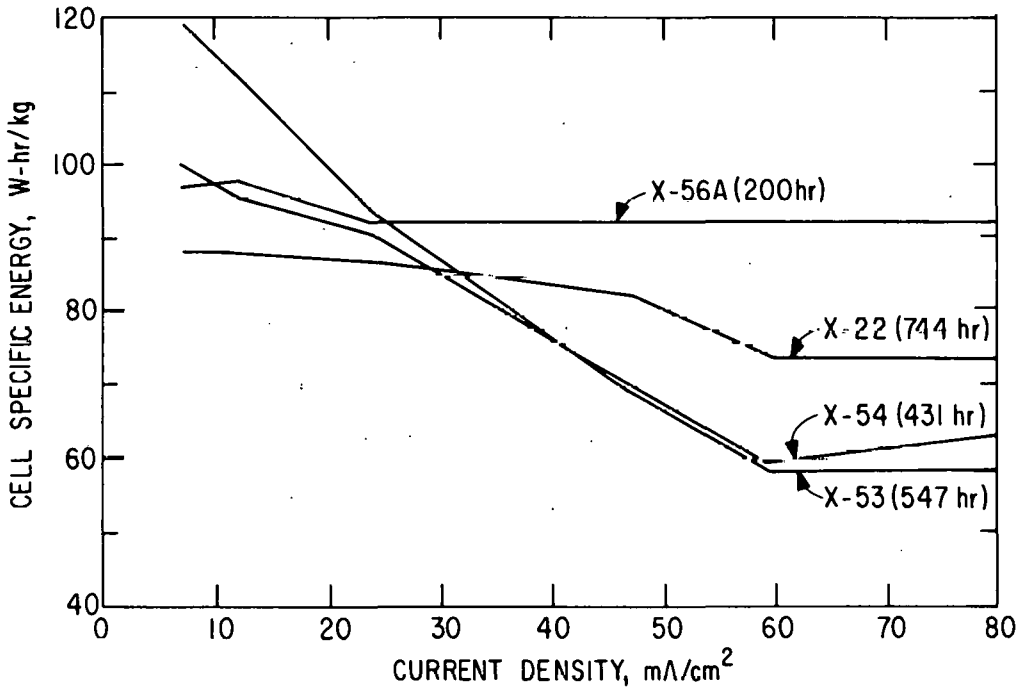

Fig. II-4. Specific Energy of Gould Li-Al/FeS Dicells

Present experimental bicells have ohmic resistances ($\Delta E/\Delta I$ at t = 0 sec) of 2.5 mΩ, which is a reduction in resistance of about 45% over that of previously tested baseline cells (see ANL-78-94, p. 52). In addition to a significant decrease in cell resistance, the weight of the current collector for these cells has been reduced by 65%. These data indicate that multiplate cells with resistances of <1.0 mΩ can be constructed.

3. Cell Testing Facilities

The increased cell fabrication capability at Gould has been matched by an expanded cell testing capability. The fill-formation facility†

* The higher specific energy of cell X-56A than that of cells X-53 and X-54 is believed to be due to the higher amount of excess iron additive (100 wt % *vs* 25 wt %) and assembly in the uncharged rather than the half-charged state.

† This facility is used to fill the cells with electrolyte and then electrochemically form the electrodes.

was adapted to handle either eight experimental bicells or four full-scale multiplate cells. A computer-controlled cell test facility has been built, and is capable of automatically cycling and gathering data from 10 cells. In addition, five single cell cyclers have been built.

At present, most of the cell hardware (can, current collector, seal parts, cell top, *etc.*,) is vendor-supplied to Gould; thus, it is possible to build a cell within a day to study a specific design problem. The full exploitation of this advantage required the capability to dissect a cell within a day or two after termination of operation to critically evaluate the design concept under test. Post-operational capabilities are in place, and improved equipment is presently on order.

4. Mark II Design and Cost Study

A design and cost study has been prepared for the Mark II electric-vehicle battery. Using a computer-assisted design analysis procedure, Gould evaluated 550 separate designs for Li-Al/FeS cells; this study was conducted to obtain a design for the Mark II cell that will result in maximum performance. The design variables included separator thickness and fiber density, current collector thickness, electrode porosity, and assumed utilization of the active materials in the electrode.

Manufacturing cost estimates were evaluated for material and hardware procurement and cost, electrode manufacture, and cell and battery assembly alternatives. These results were used to estimate the cost of batteries produced in pre-pilot, pilot, and full-scale manufacturing facilities. The study also identified the key areas where developmental work on the Mark II battery must be directed to achieve the performance and cost goals. The results of this study will be discussed in the next report.

C. Rockwell International

The Energy Systems Group of Rockwell International has been developing, fabricating, and testing Li-Si/FeS bicells for electric-vehicle applications and is conducting a detailed design/cost analysis of a 100 MW-hr energy-storage battery.

1. Electric-Vehicle Cell Development

a. Positive Electrode Development

Past efforts at electrode design and fabrication were directed to structures capable of withstanding the swelling forces generated by discharge of the positive electrode or charge of the negative electrode. The internal constraint required for this purpose was provided by bonding the external electrode components (nickel screen or current-conducting plate) to an internal structure (nickel vertical ribs). The positive electrode design is described in more detail in ANL-78-94, p. 66.

All positive electrode structures were fabricated with nickel, except where copper was used to provide added electrical conductivity

to a central current conductor. When copper was used, it was laminated between nickel sheets to protect it from corrosion. Corrosion of nickel components examined after cell tests was found to be unpredictable and was sometimes severe in isolated areas. The nickel-screen particle retainers were subject to intergranular attack. Since badly corroded areas were found in two cells outgassed at 450°C but not filled with electrolyte or placed in service, a possibility exists that the attack is due to chemical rather than electrochemical causes.

A small cell assembled with a positive-electrode current conductor of copper failed within 40 cycles due to poor coulombic efficiency. Post-test examination disclosed that the copper structure was severely corroded and that copper had been transferred to the negative electrode. A cell assembled with a positive electrode structure of nickel-plated copper has operated for over 370 cycles in 101 days with good coulombic efficiency (>98%).

b. Separator Development

Work has continued on the development of separators containing Li_3PO_4 and Li_4SiO_4, which were first described by Hu, Raistrict, and Huggins as lithium ion-conductive.[1] The optimum resistance to attack and good ionic conductivity were found with compositions containing 25 to 30 mol % Li_4SiO_4, and the balance of Li_3PO_4 (ANL-78-94, pp. 70-71). Sintered plates were prepared using this composition range (2-mm thick, 45 to 50% porosity). Small cells with 5 x 5 cm electrodes using these separators have sustained over 300 cycles without significant loss in coulombic efficiency.

A number of cells are presently being fabricated to test the practical benefits of the ion-conductivity of the Li_3PO_4- Li_4SiO_4 separator material. Tests will be made in cells using MgO powder separators, shown to be stable in tests made at ANL (ANL-78-94, p. 150) with Li-Al negative electrodes, and lithium-silicate-phosphate powder separators. The physical properties of the separators will be held as constant as possible. Tests will be made in cells with lithium silicon electrodes in one case, and with Li-Al electrodes in the other. Since MgO is not ion-conductive, measurements of internal resistance and FeS utilization should indicate the practical benefits of the ion-conductivity of the lithium silicate phosphate composition.

The stability of BN felt toward Li-Si electrodes has been questioned in view of the attack observed on BN fibers in tests involving simultaneous contact with liquid lithium and molten electrolyte. To resolve this matter, a small cell test was started using a BN felt separator. Despite an unpromising start (94% coulombic efficiency), the cell has now completed 240 cycles during which time the efficiency gradually improved and has since remained in the range of 97 to 98%. The improvement may be associated with improved wetting of the separator by electrolyte during cycling.

c. Cell Testing

Fourteen electric-vehicle Li-Si/FeS bicells (REVC series) were built and/or operated within this period. All had case-grounded negative electrodes (12.7 x 17.8 cm). Slightly smaller central positive electrodes of two types were investigated. One design was dual-faced, with 100- or 200-mesh nickel screen diffusion-bonded to vertical ribs spaced 3 mm apart. The second type employed a central-sheet current collector of copper laminated between nickel facing sheets (0.3-mm thick) to which vertical ribs were welded 6 mm apart. The active material depth for both electrodes was 0.48 cm. Nickel screen was also diffusion-bonded to the rib edges to provide constraint. The positive electrodes were loaded with a dry powder mixture of Li_2S and iron powder and had a capacity loading of 0.8 A-hr/cm^3. The negative electrodes had Type 430 stainless steel honeycomb core which was diffusion-bonded to a current-conductor back plate. After loading with 40- to 80-mesh $FeSi_2$ (uncharged cell) or Li_2Si (partially charged cell), the electrodes were sealed by welding an 80-mesh screen to the honeycomb structure. Separators consisted of fine (<200 mesh) or coarse (-40, +80 mesh) AlN used alone or in conjunction with ZrO_2 and/or Y_2O_3 ceramic cloth over the positive and negative electrodes, respectively. The electrolyte contained either 55 or 50 wt % LiCl and the balance KCl.

These cells were cycled routinely at current densities of 30 mA/cm^2 on charge and 60 mA/cm^2 on discharge, with variations in the discharge current density from 30 to 90 mA/cm^2. The upper cut-off voltage was 1.7 V, and the lower cut-off voltage was 1.0 V. The operating temperature was 450-500°C.

Performance data on the 14 cells* tested in this report period are presented in Appendix A.3. The discharge capacities of these cells were found to be highly temperature-dependent, with stable results being obtained only at a temperature in excess of 450°C. A significant improvement in positive-electrode utilization was achieved at all temperatures when the LiCl content of the electrolyte was increased from 50 to 55 wt %. The use of heavy copper current conductors (1B) or the presence of excess iron or nickel powder (12A and 2B) in the positive electrode offered little, if any, apparent benefit in cell performance. Cell resistances (t = 0 sec) varied from 2 to 4 mΩ, with cells 10A and 2B exhibiting the highest values.

The poor performance of 2B, assembled with a sintered lithium silicate phosphate separator, was the most difficult to explain. Initially attributed to the relatively dense separator, the low utilization observed at a very low current density discharge (5 mA/cm^2) indicated that poor electrical contact with one negative electrode was the probable cause. The relatively high active-material depth of the positive electrode (0.48 cm) was the principal cause of poor positive-electrode utilization; future cells will use a more practical thickness of 0.2 to 0.3 cm.

Construction of Cells 12A, 1B, and 2B in the partially charged condition (*i.e.*, substitution of Li_2Si for $FeSi_2$ in the negative electrode) increased their voltage from 1.22 to 1.34 V at a 60 mA/cm^2 discharge current density. The discharge voltage characteristics of Cells 9A-1 (uncharged) and 12A (partially charged) are shown in Fig. II-5.

*Cell designations: 1A to 8A, 9A-1, 9A-2, 9A-3, 10A-12A, 1B, 2B.

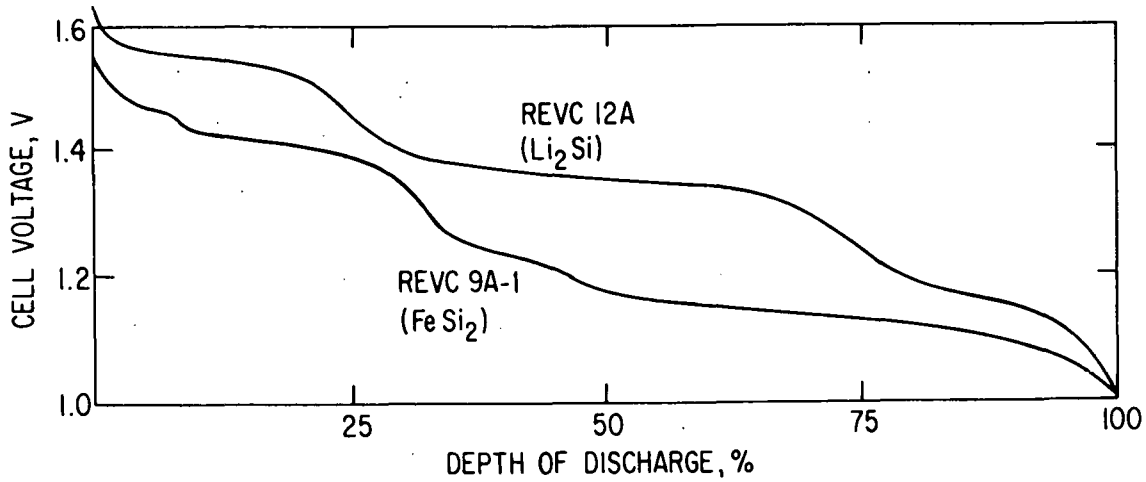

Fig. II-5. Voltage Characteristics of Uncharged and Partially Charged Cells

2. Cost for 100 MW-hr Energy-Storage Plant

A balance-of-plant (BOP) cost analysis was completed for a 100 MW-hr energy-storage plant (exclusive of cells and converter) for load-leveling applications. The basic design for such a facility is described in ANL-78-94, pp. 116-120. In this design, four 2.5 kW-hr cells are electrically connected in parallel to form a 10 kW-hr assembly, which is the basic replaceable unit of the plant. Twenty-four such assemblies are stacked in two sets of twelve to form a submodule; a module consists of six rows of six submodules each (864 cell assemblies) connected in series. Nominal dimensions for an uninsulated, assembled module are 12 x 2.8 x 6 m. In this plant design, two groups of six modules are arranged on each side of an electrical-power processing center.

Table II-4 presents the cost breakdown of this conservatively designed energy-storage plant. The total BOP cost is $80.25/kW-hr, which is significantly above the cost goal of $45-55/kW-hr. In this cost analysis, the contribution made to the total cost by the major battery functions are as follows: thermal management, $7.9/kW-hr; structural components, $30/kW-hr; power components, $32.4/kW-hr; and equalization, $19.2/kW-hr. Table II-5 presents a cost estimate for minor and major design changes in these battery function systems. As can be seen in this table, the designated minor changes would result in a 50% cost saving, with further changes resulting in another 25% cost saving. These plant design changes will require the use of taller modules (which will preclude the use of the plant in high seismic-risk areas), semiautomatic instead of completely automatic plant control, and more cells connected in parallel to reduce the equalization hardware required.

For the modified design (middle column of Table II-5), the costs were further separated into four categories: cost proportional to the number of cells in the plant (*e.g.*, primarily connection costs evaluated for 2.5 kW-hr cells), costs proportional to the current conduction network (*e.g.*, interconnectors and bus bars for 2.5 kW-hr cells), costs proportional

Table II-4. Cost Breakdown for 100 MW-hr Energy-Storage Plant

Description	Cost, $/kW-hr	Material Percent
Submodules		
Structural Steel	10.25	12.8
Copper Components	20.57	25.6
Ceramic Insulation	7.48	9.3
Miscellaneous	1.44	1.8
Subtotal	39.74	49.5
Modules		
Structural Steel and Sheet Metal	8.06	10.1
Thermal Control	2.59	3.2
Thermal Insulation	1.07	1.3
Equalization and T/C Wiring and Connectors	12.34	15.4
Subtotal	24.06	30.0
Control and Instrumentation		
Site Controller	1.82	2.3
Thermal Controllers	0.14	0.2
Circuit Protectors	3.38	4.2
Instrumentation (T/C)	0.44	0.5
Equalization Pallets	2.59	3.2
Subtotal	8.37	10.4
Ancillary Equipment		
Shelter (Hanger)	0.42	0.5
Gantry	1.17	1.5
Special Tools and Rack	0.28	0.4
Facility Lighting and Power	1.46	1.8
Bus Ducts	0.46	0.6
Subtotal	3.79	4.7
Field Installations		
Foundations	0.51	0.6
Mechanical Assembly	1.85	2.3
Electrical	0.83	1.0
Startup	0.34	0.4
Equalization Electrical	0.76	1.0
Subtotal	4.29	5.4
Total Balance-of-Plant	80.25	100.4

Table II-5. Plant Cost After Changes in Design

Functional Subsystem	Cost, $/kW-hr	Minor Change	Resulting Cost, $/kW-hr	Further Change	Resulting Cost, $/kW-hr
POWER					
Copper Components	18.3	Insulation Quality	10.3	Quantity	8.3
Insulation & Misc.	7.0	Quality	2.2	Quantity	1.2
Circuit Breakers	3.4	Fuses & Switches	0.8	None	0.8
Site Controller	1.8	Semiautomatic	1.4	Manual	0.4
Facility Power/Light	1.1	Smaller	0.8	Smaller	0.5
Installation	0.8	Less	0.7	Less	0.6
	32.4		16.2		11.8
EQUALIZATION					
Wiring & Connectors	14.3	Partial Reduction	7.3	Delete Added Circuitry	1.3[a]
Chargers & Controls	2.6	Quantity	1.6	Delete	0.0
Insulation & Misc.	1.5	Quality	0.7	Delete	0.0
Installation	0.8	Quantity	0.4	Delete	0.0
	19.2		10.0		1.3
STRUCTURES					
Submodule	10.2	Lighter, Quality	5.0	Delete	0.0
Module	6.0	Lighter, Quality	3.0	Smaller	2.0
Facility	1.9	Smaller	1.0	None	1.0
Installation & Misc.	1.9	Less	1.0	None	1.0
	20.0		10.0		4.0
THERMAL					
Tubes & Plenums	2.0	Delete	0.0	None	0.0
Blower Units	2.6	Smaller	1.5	None	1.5
Insulation	1.1	Quantity	0.8	None	0.8
T/C Instrumentation	0.9	On Module	0.5	None	0.5
Installation	0.8	Less	0.3	None	0.3
Facility Power	0.4	Less	0.2	None	0.2
Controllers	0.14	On-Off	0.1	None	0.1
	7.9		3.4		3.4
OTHER	0.8		0.7		0.7
TOTALS	80.3		40.3		21.2

[a]Residual for voltage measurement.

to the total cell weight (*e.g.*, structural supports, *etc.* for cells with a 80% energy (W-hr) efficiency and a specific energy of 60 W-hr/kg); and costs independent of the above. The costs for these four factors are given in Table II-6.

Table II-6. Costs for Modified Plant Design

Cost Factors	Cost, $/kW-hr
Proportional to number of cells	3.3
Proportional to conductor vol.	12.5
Proportional to cell weight	16.5
Independent of above	8.0

All aspects of the plant design require further study including the design specification, support structure concept, mode of operation, seismic requirements, materials of construction, and cell performance. In general, design margins must be reduced and reliability and maintenance influences on cost assessed. A number of design approaches are being considered for reducing the BOP costs, including the following:

(1) use of high-energy-density cells,

(2) elimination of external equalization,

(3) minimization of cooling requirements through use of high-efficiency (>90%) cells,

(4) optimization of cell capacity to minimize intercell connector cost and structure cost,

(5) use of bus-bar materials other than copper,

(6) use of inert atmosphere in battery module.

The methodology being used to assess the cost of the design approaches is based on the annualized bus-bar cost analysis.[2]

A perturbation analysis is currently in progress to determine the optimum combination of cell efficiency, cell size, and conductors in a 100 MW-hr storage plant. A simplified Shepard model for the cells is being used to relate cell efficiency and utilization of active materials to the shunt and series resistances of the cells for the analysis. Preliminary results from this analysis indicate that for cells of 110 W-hr/kg specific energy* at 5-hr discharge rate, the optimum cell size appears to be 2.5 - 5.0 kW-hr. This gives an energy efficiency of 82-85% for the system producing the minimum annualized cost.

*This is 90% of the specific energy goal for the Mark II battery cells.

D. Other Contracts

Work has continued at the Research Laboratories of the General Motors Corporation on lithium-alloy/FeS_2 cells with molten LiCl-KCl electrolyte. These investigations are concerned with the performance of the FeS_2 electrode as a function of the electrode thickness, porosity, and current collector, and the composition of the electrolyte. The results of these studies will be used in the development of a comprehensive mathematical model of the FeS_2 electrode.

Studies have continued at the Illinois Institute of Technology on the electroplating of molybdenum from molten-salt electrolytes, with the objective of developing low-cost, corrosion-resistant current collectors for FeS_2 electrodes. A different approach to corrosion-resistant current collectors for FeS_2 electrodes is being taken by investigators at the Institute of Gas Technology, who are studying methods of boronizing iron structures. It may be possible to form a protective coating of iron boride that could be made self-healing by the addition of a boronizing agent to the active material in the electrode.

The Carborundum Co. is continuing to develop a process for the fabrication of boron nitride felt to be used as an electrode separator material. A subcontract from ANL for this work is under negotiation.

III. CELL AND BATTERY TESTING

Argonne is testing cells fabricated by ANL and industrial contractors. The ANL cells have designs that are expected to reduce cost and/or improve performance. Most of the industrial cells were fabricated by Eagle-Picher as part of the Mark IA battery program, which was described earlier in this report. In addition, ANL is testing a 6-V battery fabricated by Eagle-Picher for the Mark IA program.

A. Cell and Battery Testing Facilities

(G. L. Chapman, J. D. Arntzen, V. M. Kolba

A laboratory is being prepared and equipped for testing two 60 kW-hr batteries. Batteries will be tested under a variety of modes, *e.g.*, discharges and charges at constant current or constant power; discharges that follow a driving profile such as a SAE J-227 profile;[3] or charges at constant voltage and cell equalization after bulk charging; these tests will employ computer-controlled power supplies. This facility was described in ANL-78-94, pp. 89-90, and will be used to test the first full-scale lithium/metal sulfide battery (Mark IA).

During this report period, the system hardware was made operational as a complete unit, although some refinements in software have yet to be finished. The hardware for the watchdog backup system, which protects the battery in the event of primary system failure, is essentially complete, and software is being prepared. Tests of the overall primary system have been carried out in which series-connected lead-acid batteries were used as a substitute for the lithium/metal sulfide battery. In these tests, the battery was cycled in various modes of operation. The computer controlled charge and discharge rates as well as current level, monitored battery and individual cell voltages, determined open-circuit time, commanded equalization when required, and stored and printed out performance data on command.

Construction of a facility capable of simultaneous lifetime testing of up to 50 cells for the electric-vehicle program is essentially completed. The emphasis will be placed on the testing of cells fabricated by industrial contractors to acquire statistical data on the performance of these cells. The facility consists of 50 modules, each containing one cell and cycler, and a data acquisition system for processing the cell data (see ANL-78-94, pp. 90-97).

B. Testing of ANL Cells

(H. Shimotake, F. J. Martino, T. W. Olszanski, T. D. Kaun, L. G. Bartholme)

Over the past six months, ANL has fabricated and tested 22 engineering-scale cells. A summary of the performance data for these cells is presented in Appendix A.4. The cells were assembled in the charged, uncharged, or semi-charged state. For most of the cells, the electrodes are pressed mixtures of active materials and electrolyte, the separators are BN felt, and the electrolyte is LiCl-KCl eutectic. The cells have designs that

are expected to reduce cost, and/or improve lifetime and performance at high discharge current densities (>75 mA/cm^2). Whenever advances in cell technology are demonstrated, these advances are incorporated into the contractor cells.

1. Bicells with Pressed Electrodes

For the past several years, Cu_2S has been added to the positive electrode of Li-Al/FeS cells to eliminate the formation of J phase, which produces diffusional overvoltage and poor electrical performance. Post-test examinations of cells of this type (see Section IV.C) have indicated, however, that cell failure is sometimes caused by deposition of copper in the separator. Recent studies (ANL-78-94, pp. 122-125) have indicated that increasing the LiCl content of the electrolyte above that of the eutectic and/or using a high initial positive-electrode loading (1.4 to 1.6 A-hr/cm^3)* may significantly improve cell performance without adversely affecting lifetime. Both of these approaches have been investigated with the M-series cells; these cells have cold-pressed electrodes assembled in the charged state and BN felt separators. The cell characteristics and performance for this series are given in Table III-1.

Table III-1. Cell Characteristics and Performance Data for M-Series Cells

	M-8	M-9	M-10	M-11	M-12
Cu_2S Added to FeS, mol %	0	16	0	0	16
LiCl Content of Electrolyte, mol %	67	58[a]	58[a]	67	58[a]
Pos. Elec. Loading, A-hr/cm^3	1.4	1.6	1.4	1.6	1.4
Specific Energy,[b] W-hr/kg	59	65	42	53	53
Specific Power,[c] W/kg	62	76	66	75	70
Cycle Life	347	244	300	365	202

[a]Eutectic composition.

[b]Measured at a current density of 75 mA/cm^2.

[c]Peak power sustainable for 15 sec at 50% discharge.

Three of the M-series cells, M-8, -10, and -11, operated for over 300 cycles with good electrical performance. Of these three cells, two had a positive capacity loading of 1.4 A-hr/cm^3--Cell M-8 (LiCl-rich electrolyte) and Cell M-10 (eutectic electrolyte). In comparison with Cell M-10, M-8 had a significantly higher active-material utilization, and consequently a higher specific energy (59 *vs* 42 W-hr/kg). In addition, the capacity decline of Cell M-8 was significantly less than that of M-10 (8% decline in

*Measured with cell fully charged.

350 cycles *vs* 28% in 300 cycles). Mechanical problems with the cell containing LiCl-rich electrolyte and a positive-electrode loading of 1.6 A-hr/cm^3 (Cell M-11) resulted in a capacity decline of 38% in 365 cycles; therefore, LiCl-rich electrolyte does not appear to have beneficial effects on the capacity retention of a cell with a 1.6 A-hr/cm^3 loading.

The performance data for the M-series cells indicate that specific power is improved by the use of a positive-electrode loading of 1.6 A-hr/cm^3. This effect can be easily seen by comparing the specific powers listed in Table III-1 for Cells M-9 and M-12 or M-8 and M-11. At 50% depth of discharge, the power improvement resulting from the higher capacity loading is only about 9% for the cells with Cu_2S additive, but about 30% for the cells with the LiCl-rich electrolyte. Thus, for cells with a positive-electrode loading of 1.6 A-hr/cm^3, LiCl-rich electrolyte appears preferable to adding Cu_2S to the positive electrode to improve specific power.

The fabrication of positive electrodes with high positive loading densities requires a reduction of the electrolyte volume fraction to accommodate the active material. In the two Li-Al/FeS-Cu_2S cells, the initial volume fraction of electrolyte at full charge was 0.43 for Cell M-12 (1.4 A-hr/cm^3) and 0.39 for Cell M-9 (1.6 A-hr/cm^3). Of the two cells with LiCl-rich electrolyte, the volume fraction of electrolyte was 0.49 for Cell M-8 (1.4 A-hr/cm^3) and 0.42 for Cell M-11 (1.6 A-hr/cm^3). Performance data indicated that the positive-electrode utilization* of Cell M-9 was 10% lower than that of M-12 (57 *vs* 67%) and that the utilization* of Cell M-11 was 20% lower than that of M-8 (54 *vs* 74%). Therefore, a positive-electrode loading of 1.6 A-hr/cm^3 appears to have a detrimental effect on utilization. This effect has been attributed to the higher electrolyte volume in the positive electrodes of Cells M-8 and M-12. In the cells with LiCl-rich electrolyte, the higher utilization of Cell M-8 in comparison with M-11 resulted in a higher specific energy (59 *vs* 53 W-hr/kg). However, for the cells with the Cu_2S additive, the higher utilization obtained from Cell M-12 did not produce a higher specific energy (see Table III-1); mechanical difficulties encountered with Cell M-12 probably account for its unexpectedly low specific energy.

Present Li-Al/FeS cells have a positive current collector made of low-carbon steel; however, it was believed that the use of a nickel current collector in the positive electrodes of this type of cell would improve performance and lifetime.† Therefore, two similar bicells (hot-pressed electrodes assembled uncharged and BN felt separators), one with a nickel current collector (R-47) and the other with a low-carbon steel current collector (R-48), were constructed and tested. To date, Cells R-47 and R-48 have operated for 112 and 147 cycles, respectively, and have attained about the same performance: specific energy of 56 W-hr/kg at the 4-hr rate (72 mA/cm^2), capacity decline of less than 1%, and cell resistance of 4.5 mΩ at 50% depth of discharge (3.8 mΩ at 20% depth of discharge). Testing of these cells will continue in order to determine the long-term effects (>300 cycles) of these current collector materials.

---

*Measured at a current density of 75 mA/cm^2.

†Nickel has a lower resistivity and corrosion rate (ANL-77-68, p. 41) than those of low-carbon steel.

2. Bicells with Carbon-Bonded Electrodes

Over the past few years, carbon-bonded positive electrodes have been under development as an alternative to those made by pressing techniques. In the carbon-bonded electrode, the particulate active material is supported in a matrix of pyrolyzed carbon. This structure is formed by the pyrolysis (450-550°C) of a paste-like mixture of active material (*e.g.*, FeS or FeS_2), a volatile pore-forming agent (ammonium carbonate), a binder (furan resin*), and a carbonaceous filler.

Cell KK-15 was the only bicell with a carbon-bonded electrode operated during this report period. This cell had essentially the same design characteristics as Cell M-8, including a positive-electrode loading of 1.4 A-hr/cm^3 and LiCl-rich electrolyte. In Cell KK-15, however, the positive electrode was carbon-bonded (10 vol % carbon) and the positive-electrode frame was eliminated. This cell operated for 245 cycles, and performance was as follows: a specific energy of 70 W-hr/kg at the 4-hr rate, and a specific power of 80 W/kg at 50% depth of discharge (104 W/kg at 3% depth of discharge). A cell resistance of 2.9 to 3.1 mΩ at 50% discharge produced stable specific power throughout discharge. Testing of this cell was ended due to an accidental overcharge. During the next period, a cell with a carbon-bonded positive electrode having an initial capacity loading of 1.2 A-hr/cm^3 at full charge and 15 vol % carbon will be tested.

3. Bicells with MgO Powder Separators

Earlier work (ANL-77-75, p. 35; ANL-78-21, p. 41) had indicated that nonconductive ceramic powders are a possible low-cost alternative to the BN fabric and felt that are currently being used as electrode separators in Li/MS_x cells. The purpose of these investigations is to evaluate the use of MgO powder separators in engineering-scale Li-Al/FeS cells. Two techniques, vibratory compaction and hot-pressing (see ANL-78-94, p. 134), were used to form the powder separators. In cells with a vibratory-compaction separator, it is necessary to use frames and screens on both the positive and negative electrodes to maintain a smooth electrode/separator interface during cell assembly and operation. In cells with hot-pressed separators, however, only the negative electrodes require frames and screens.

During this report period, we tested two Li-Al/FeS bicells with MgO powder separators--PW-9 and -16. The separator was formed by the hot-pressing technique in Cell PW-9 and by the vibratory-compaction technique in Cell PW-16. Cell PW-16 also had a LiCl-rich electrolyte to improve performance.

After 744 cycles, Cell PW-9 is continuing to operate with stable performance. The active-material utilization is 33% at a current density of 52 mA/cm^3, and the coulombic efficiency is 98%. Cell PW-16 was operated for 330 cycles and then operation was terminated due to the end of testing. At the termination of operation, this cell had a coulombic efficiency of 98% and a capacity decline from the initial value of 19%. The results of these performance tests and previous ones (ANL-78-94, p. 134) indicate that powder separators may be a viable alternative to BN felt or fabric, and that the method of formation of the powder separator has little, if any, effect on cell performance.

*A product of Quaker Oats Chemical Co., Morton Grove, IL.

4. Multiplate Cells

The goals for the Mark II battery require that it attain a higher performance and lower cost than those of Mark IA. Consequently, separators of BN felt and MgO powder, both of which are potentially inexpensive, are now being tested at ANL in multiplate cells (three positive and four negative electrodes). The early bicell studies provided a basis for the design of the multiplate cells.

As with bicells, use of BN felt in sheet form appeared to be the most practical approach for the multiplate cell. One of the major problems anticipated during extended operation of multiplate cells with BN felt separators was unequal electrode operation (through electrode dissimilarities) causing uneven stress on the separator. This problem is especially acute because presently available BN felt is delicate (96% porosity), though much stronger than earlier samples. Thus, the BN felt was given structural support through the use of fine screen (200 mesh) at the faces of both the positive and negative electrodes; this support was intended to reduce electrode surface irregularity and possible rupture of the felt.

Two multiplate Li-Al/FeS cells with BN felt separators, K-MP-1 and M-MP-3, were tested. The electrode design for Cell K-MP-1 was based on that of bicell KK-15, which had a carbon-bonded positive electrode with an initial loading of 1.4 A-hr/cm^3 at full charge and no positive-electrode frame. The other cell, M-MP-3, was similar in design to Cell M-8, which had pressed electrodes and an initial positive-electrode loading of 1.4 A-hr/cm^3. The design for Cell M-MP-3 is graphically presented in Fig. III-1.

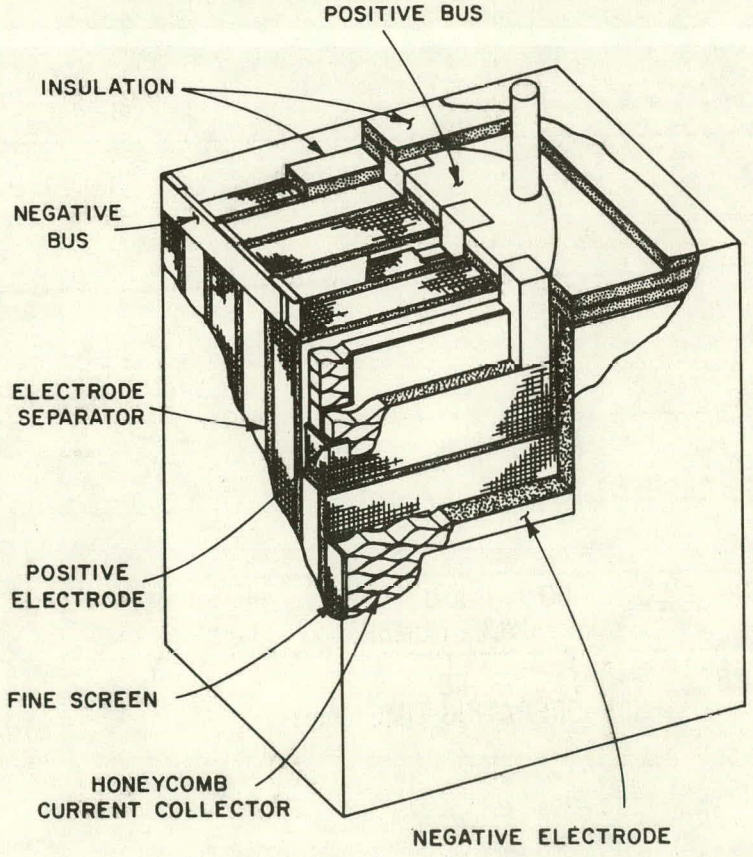

Fig. III-1. Design of ANL Multiplate Cell

The performance of Cells K-MP-1 and M-MP-3 is summarized in Table III-2. Cell K-MP-1 operated for 42 cycles at which time it developed short circuits, while Cell M-MP-3 is continuing to operate after 85 cycles with only a 2.5% capacity loss (see Fig. III-2). Both of these multiplate cells attained performance levels slightly better than those of their respective bicells, even though neither multiplate cell was optimized for maximum performance.

Table III-2. Performance Data on Two Multiplate Cells

	K-MP-1	M-MP-3
Pos. Elect. Util.,[a] %	77	50
Specific Energy,[a] W-hr/kg	79	65
Cell Resistance,[b] mΩ	1.1	1.14
Specific Power,[b] W/kg	101	80
Cycle Life	42	>85[c]

[a]Measured at a current density of 75 mA/cm^2.

[b]15 sec pulse at 50% discharge.

[c]Operation still in progress.

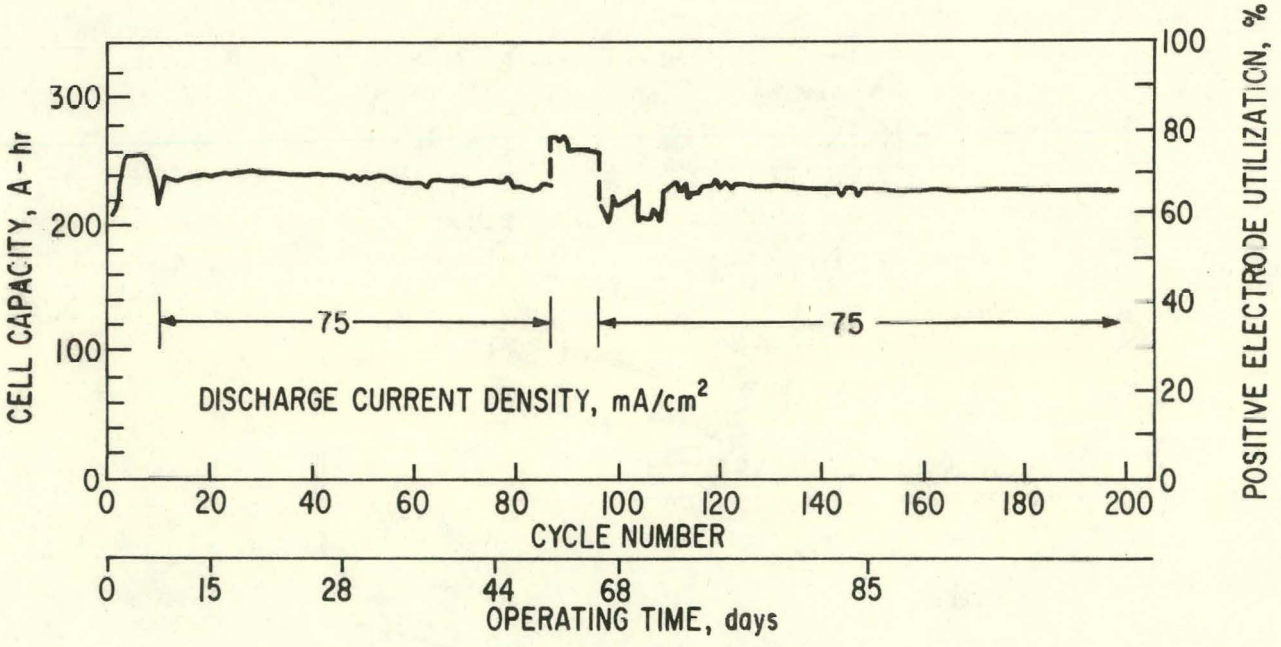

Fig. III-2. Capacity of Cell M-MP-3

The lower lifetime and somewhat higher performance of Cell K-MP-1 in comparison with that of M-MP-3 can be partially attributed to the elimination of the positive-electrode frames, which allowed the construction of a more compact cell.

A third multiplate Li-Al/FeS cell, which has a vibratory loaded separator of MgO powder, has been operated through four cycles. This cell is expected to achieve a specific energy of 50 W-hr/kg at the 4-hr rate.

C. Testing of Industrial Cells at ANL

(V. M. Kolba, T. D. Kaun, P. F. Eshman, W. A. Kremsner, G. W. Redding, J. L. Hamilton)

In this report period, a number of industrially produced cells were tested at ANL, most of which were fabricated by Eagle-Picher for the Mark IA program (see Section II.A). The test results of the Eagle-Picher cells are discussed below.

1. Continued Cycling after Cell Failure

A battery composed of series-connected cells must continue to operate after individual cells have exceeded the normal discharge cutoff voltage; otherwise, battery life will be limited to that of the shortest-lived cell. Thus, two Mark IA cells (EPMP-7-027 and -060) were cycled long after a marked decline in their coulombic efficiency. The cells were cycled with a 4-hr discharge and an 8-hr charge, each amounting to about 300 A-hr of capacity. The cells operated in reverse voltage during discharge. One of the cells (-029) operated in reverse voltage for 90 cycles, and for the last 50 cycles the reverse voltage peak has been -1.44 V. The other cell has been operated in reverse voltage for 60 cycles, and for the last 30 cycles the reverse voltage has been -1.64 V. We did not see a trend toward a dead short circuit (no resistance) or an open circuit. These tests indicate that a battery can be cycled long after operation of some of the cells has terminated. A battery voltage loss equivalent to the output of two cells will occur for each cell that is badly deteriorated and run into voltage reversal.

2. Thermal Tests

The effects of operating temperature on cell capacity have been investigated previously (ANL-78-94, p. 104). During this report period, three Li-Al/FeS multiplate cells--EPMP-7-060, -091, -162--were operated at temperatures of 425 to 475°C. The effect of these temperatures on cell capacity is shown in Table III-3. As can be seen in this table, in the temperature range studied, cell capacity increases with increased operating temperature. However, operation at high temperatures for long periods is expected to increase the corrosion rates of the FeS cell components, thereby shortening the cell lifetime. For the Mark IA battery, the optimum operating temperature appears to be 460-470°C.

Table III-3. Effects of Temperature on Capacity of Three Li-Al/FeS Cells

	Capacity, A-hr					
	420°C	425°C	450°C	460°C	470°C	475°C
EPMP-7-060	-	-	257	-	307	-
EPMP-7-091[a]	200	-	290	320	-	-
EPMP-7-162[a]	-	250	315	-	-	335

[a] Cu_2S added to positive electrode.

3. Driving Profile Tests

One of the Eagle-Picher Mark IA cells (EPMP-7-071) was cycled in the laboratory for 60 deep cycles under simulated driving conditions (the SAE J-227 driving profile[3]). During each cycle, the driving profile, which includes acceleration, cruise, and coast, is repeated every 72 seconds until the cell capacity is completely discharged; and then the cell is charged for the next cycle. For 35 of the cycles, the driving profile had constant power acceleration (140 W maximum power). Under these conditions, the cell would discharge about 305 A-hr each deep cycle. (This was close to the 4-hr discharge capacity for this cell, 320 A-hr.) For the balance of the profile testing, more severe driving conditions were used (constant acceleration with a 240 W maximum power). Under these conditions, the cell achieved the full power of 240 W over about 65% of its discharge capacity (200 A-hr). This cell failed after 118 deep cycles due to a mechanical failure. Post-test examination of the cell showed no unusual conditions which could be related to the severe simulated driving conditions under which the cell was cycled.

4. Improvements in Cell Performance

During the developmental stage of the Mark IA program (Section II.A), it was discovered that (1) the Eagle-Picher multiplate cells were frequently failing due to swelling of the cell can which resulted in extrusion of active material from the positive electrode* and (2) that the cell power was lower than that required by the Mark IA goals. Efforts at ANL to resolve these problems are described below.

a. Cell Swelling

A frequent failure mode of the Mark IA developmental cells was a short circuit caused by a bowing out of the edges and bottom of the cell can, which allowed extrusion of the active material from the positive electrodes. This effect leads first to a loss of capacity and coulombic efficiency, and finally to a short circuit. The extrusion of active material occurred over

*See Section IV.C for a more detailed description of the cell failure modes of Eagle-Picher's cells.

several cycles; thus, this type of cell failure was not caused by a large force generated in the positive electrode during a single cycle.

To achieve the very high specific and volumetric energy density goals for these cells, a large fraction of the cell volume is filled with active materials, cell hardware, and electrolyte. The electrolyte expands about 20% when it melts, leaving less gas volume inside the cell and thereby generating a higher gas pressure. As an example, in Cell EPMP-7-094, 74.2% of the electrolyte plus gas volume was occupied by electrolyte before it was melted; with the electrolyte molten, this volume was 88.1%. The gas volume decrease from 25.8% to 11.9% causes a factor of 2.2 increase in the gas pressure. If the cell is sealed at room temperature and then heated to 450°C, the pressure is increased by an additional factor of 2.6. Since the feedthrough is not completely gas tight, this pressure is relieved gradually. Because of the time required to heat the cell to operating temperature (several hours), the temperature effect on gas pressure is probably small. However, melting of the electrolyte takes place rather quickly once the eutectic temperature is reached, resulting in a pressure surge. This pressure surge was noted experimentally when a pressure gauge was attached to Cell EPMP-7-094 and the cell was cycled. Furthermore, this cell was operated for 74 deep cycles with the edges, bottom, and major faces restrained; post-test examination showed that the edges of the positive electrodes were essentially in perfect condition.

Figure III-3 shows the effect of electrolyte volume prior to melting on the pressure differential, *i.e.*, the internal cell pressure after the electrolyte melts divided by the internal cell pressure prior to electrolyte melting. In the case of Cell EPMP-094 (0.74 electrolyte volume prior to melting), the pressure inside the cell prior to melting is about 1 atm (absolute), and after melting the pressure is about 2.2 atm (absolute). Thus, the pressure differential across the can wall after melting is about 2.2 atm, which is sufficient to deform the thin wall can. As illustrated in Fig. III-3, the extent of the pressure increase is largely a function of the available void space after the electrolyte filling operation, which was not closely controlled in most of the Mark IA developmental cells. For the Mark IA battery, the force on the cell edges will be controlled by closely regulating the amount of electrolyte added to the cells, and the battery cell tray is being designed to provide cell-surface restraint.

As part of the experiment with Cell EPMP-7-094 to measure cell pressure, gas samples of the internal cell atmosphere were taken during the first cycle. These samples showed 2% (by volume) H_2 and 1.6% CH_4 in the helium atmosphere. Gas samples from another cell during its first cycle have shown essentially the same result. In this later test, sampling is continuing with cycling but results are not yet available. Gas releases of this small magnitude when the cell electrolyte melts have little effect on the pressure level. However, since hydrogen diffuses rather rapidly through the insulating jacket wall at operating temperature (discussed later), it is important to determine if the cells are a continuing source of hydrogen in the battery.

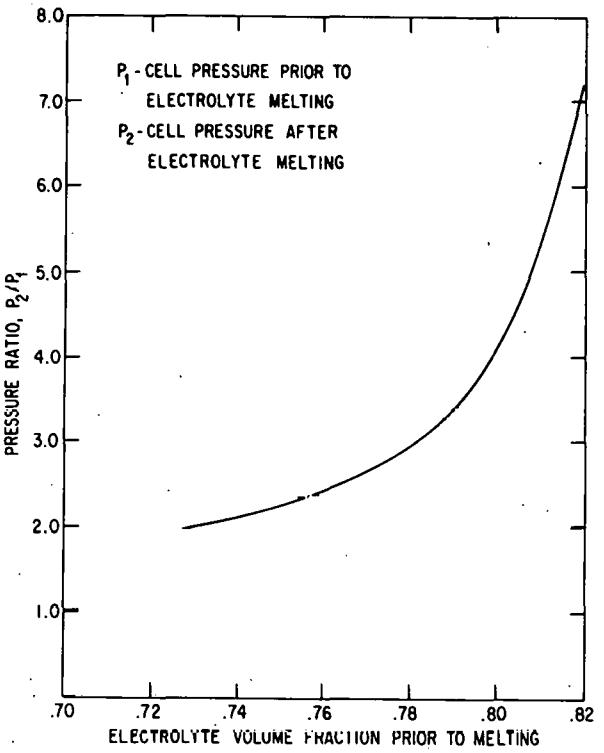

Fig. III-3. Increase in Cell Pressure Related to Electrolyte Melting Operation

b. Power

The power requirements for the Mark IA battery are 30 kW at 50% depth of discharge. At this discharge depth, the Mark IA cell must attain a power output of at least 250 W at a discharge current of 300 A, which is the motor-controller limit for the Mark IA test van.

Figure III-4 shows the power output as a function of discharge current for three Eagle-Picher cells--EPMP-7-067, -071, and -091. At 50% discharge, Cell EPMP-7-091 attained a power of 220 W at a current of 300 A, which is clearly below the Mark IA power goal; the cell resistance is 1.65 and 1.79 mΩ at 5 and 50% discharge, respectively. To improve the power characteristics of Cell EPMP-7-071, the negative terminal was bypassed, and the negative electrode connection made directly through the negative-electrode bus bars.* This cell achieved a somewhat higher power (240 W at a current of 300 A) and a lower cell resistance (1.4-1.5 mΩ) than those of Cell EPMP-7-071; however, the cell power was still below the Mark IA goal. For Cell EPMP-7-067, both the positive and negative electrode connections were made directly to their respective bus bars. At 15% discharge, this cell attained a power of 315 W at a current of 300 A, and a cell resistance of 1.05 mΩ.

*See upper portion of Fig. III-6 for an illustration of location of typical negative and positive terminals and bus bars.

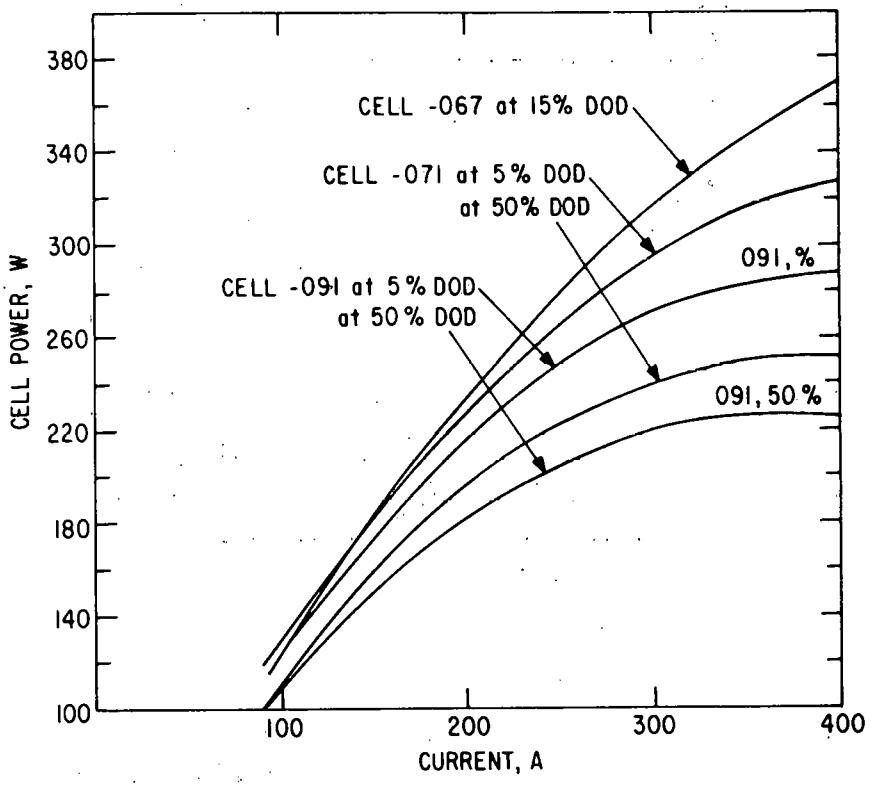

Fig. III-4. Power for Three Multiplate Cells

As a result of the low power attained by Eagle-Picher Mark IA cells, ANL made resistance measurements on the components of a number of cells. As a result, several recommendations were made to Eagle-Picher on modifications in their Mark IA cell design that improved power capabilities. Figure III-5 shows the resistances obtained by various modifications in the components of the Eagle-Picher cells. The current collectors in the first Mark IA cells were honeycomb structures (about 1.3 cm honeycomb cell size) woven from 0.0075-cm thick mild-steel (AISI 1010) ribbons. About half of these ribbons were connected to the electrode bus bars. Cell resistance was decreased by about 0.1 mΩ through the following changes in this structure: decreasing the honeycomb-cell size by half, increasing the ribbon thickness to 0.0125 cm, and connecting all the honeycomb ribbons to bus bars. This modification is indicated by symbol R_{EC} in Fig. III-5. A thicker and wider positive bus bar and improved techniques for welding the current collector ribbons to the positive bus bar (R_{PB}) gave a resistance decrease of about 0.05 mΩ. The connection between the positive terminal and the bus bar was improved (components redesigned and welding improved), and this modification (R_{PT}) resulted in a decrease in resistance of about 0.1 mΩ. Changes in the connection between the negative bus bar and lead ribbons resulted in only small resistance improvements (R_{NB}). The largest resistance improvement, 0.2 mΩ, came from adding a copper overlay to the top of the cell to lower the resistance path between the negative bus bar and the intercell connector (R_{NT}). These changes have been implemented by Eagle-Picher in the final fabrication of Mark IA cells (see Fig. III-6), and the resistance is now in the range of 1.1-1.2 mΩ, which should increase the peak power well above the Mark IA goals.

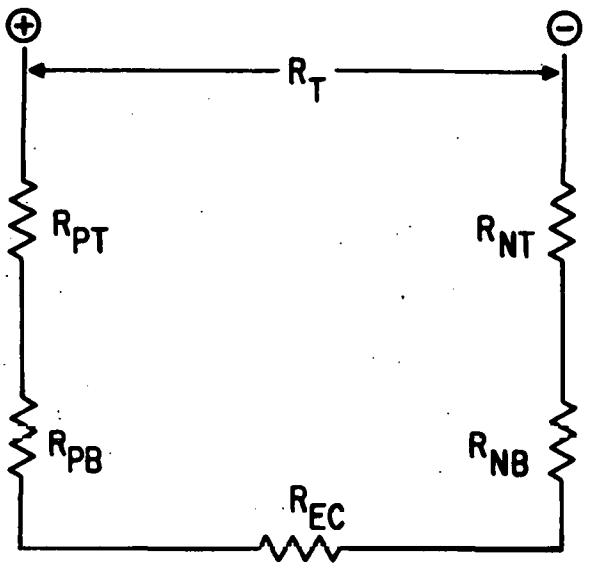

Fig. III-5. Resistance Mapping for Eagle-Picher Multiplate Cells

	Symbol	Resistance, mΩ	
		Standard Design	Modified Design
Electrode couples at full charge state[a]	R_{EC}	0.85-0.95	0.73-0.83
Positive bus bar connection	R_{PB}	0.05-0.1	0.025-0.05
Positive cell terminal	R_{PT}	0.25-0.30	0.15-0.20
Negative bus bar connection	R_{NB}	0.05-0.1	0.05-0.025
Negative cell terminal connections	R_{NT}	0.25-0.30	0.075-0.1
Total Cell	R_T	1.45-1.75	1.0-1.23

[a]Add 0.1 mΩ for 50% depth of discharge.

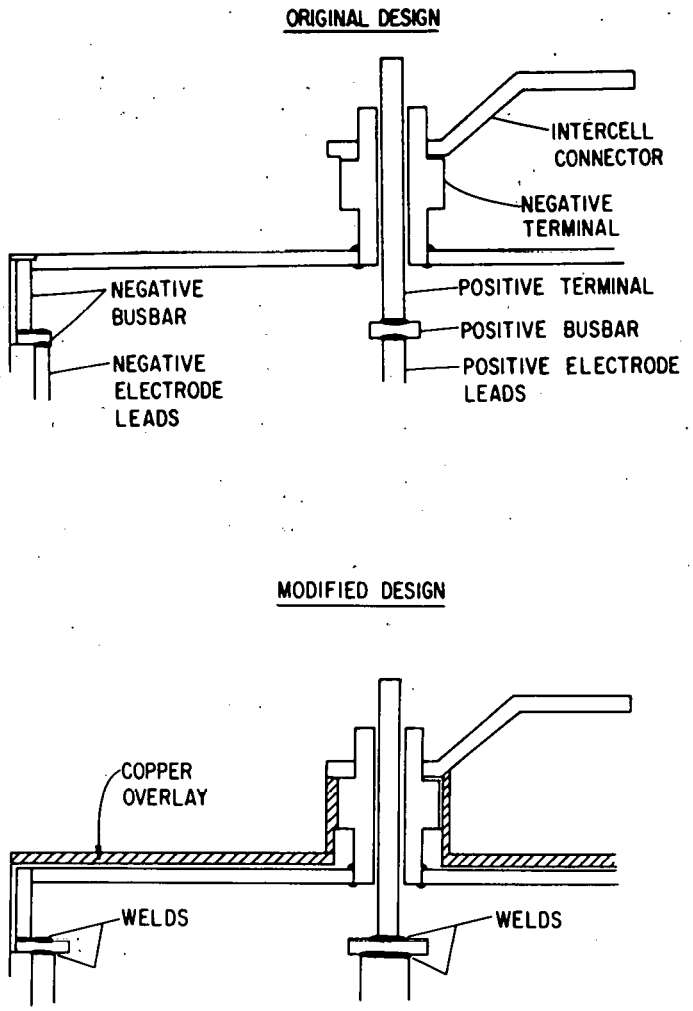

Fig. III-6. Design Changes to Improve Resistance in Multiplate Cells

D. 6 V Battery Tests

(V. M. Kolba, J. L. Hamilton, G. W. Redding, M. K. Farahat, E. R. Hayes, G. L. Chapman, W. H. DeLuca)

The 6-V lithium/metal sulfide battery module fabricated by Eagle-Picher (see Section II.A) is being tested at ANL.

During the laboratory testing of the 6-V module, small amounts of hydrogen were found in the vacuum annulus of the insulating case. The main source of hydrogen is probably Raybestos insulation between the cells, which apparently undergoes slow thermal decomposition, producing water vapor. The water vapor would react with various metals in the system to form hydrogen, which diffuses through the inner wall of the vacuum annulus. Some hydrogen may also be evolved from the cells; tests are in progress to obtain qualitative information on this source (Section VII.C). The problem with hydrogen is being controlled by periodic purging of the battery with argon and pumping on the vacuum annulus.

The 6-V battery module, which contains five cells, has now undergone 58 deep discharge cycles (70 A on discharge and 40 A on charge) in the laboratory with less than 5% loss of capacity and 7.6% loss of energy (from 1.63 to 1.51 kW-hr). It has been difficult to equalize the cells in this battery because of the high resistance in the lead wires. During five cycles, beginning on cycle 27, battery cycling was programmed to simulate actual driving conditions (J2276 Cycle C driving profile[3]). The energy output of the driving cycle tests was 1.65 kW-hr (best cycle).

After laboratory testing, the module was connected in series to the present 144-V lead-acid propulsion battery in a Volkswagen van, and road tested for one hour (without regenerative braking). At the end of one hour, the internal temperature of the 6-V module had decreased from 475 to 470°C. (The full-scale 40 kW-hr Mark IA battery will heat up slowly during discharge). The performance of the battery was excellent. On-board instrumentation was used to monitor electrical interactions between the module and the propulsion system of the van; no adverse effects were observed. Testing of the module with the ANL designed charger-equalizer resulted in complete equalization of all five cells.

IV. CELL PERFORMANCE AND LIFETIME SUMMARY

During this period, we determined the average performance and lifetime of recently operated Li-Al/FeS cells of similar design. These determinations are made to give some idea of the typical performance and lifetime being attained by Li-Al/FeS cells. Cell status tests are planned to establish the status of the development of various cell designs. In addition, 44 cells were subjected to post-test examinations to provide information on cell failure mechanisms. These results are evaluated and appropriate recommendations made for improving cell performance.

A. Electrical Performance and Lifetime
(E. C. Gay)

Table IV-1 lists the average performance and lifetime of three series of cells tested during this report period. The M-series is three state-of-the-art bicells with felt separators (namely, M-8, -10, and -11); and the PW-series is three bicells with MgO powder separators (namely, PW-8, -9, and -10). Both of these series were tested at ANL (see Section III.B). The EPMP-series is 10 multiplate cells with BN fabric separators (namely, EPMP-7-017, -031, -046, -055, -056, -057, -062, -063, -075, and -086); these cells were fabricated and tested by Eagle-Picher Industries, Inc. (Section II.A). Also included in Table IV-1 is the I-series, which is five Eagle-Picher bicells with BN fabric separators (namely, I3B1, I3B2, IB4, I3C2, and IB6); these cells were operated at ANL during 1977-78. For comparison purposes, we computed the average performance of this series at an arbitrarily selected lifetime of 336 cycles; the average lifetime is actually much longer. As expected, the highest specific energy was achieved by the EPMP-series multiplate cells; however, these cells also had the highest decline in specific energy with cycling. The cause of this performance decline will be discussed later in this section.

Table IV-1. Average Performance and Lifetime of Li-Al/FeS Cells

Series Designation	Specific Energy,[a] W-hr/kg	Initial W-hr Eff.,[b] %	Cycles	Percent Decline[c]		
				Specific Ener.	A-hr Decline	W-hr Decline
M-series	53	81.3	337	13.3	3	0
PW-series	40.7	84.3	281	9.2	0	6.2
EPMP-series	99.1	79.5	186	29.4	8.1	11.0
I-series	62	82.2	336[d]	13.6	1.2	2.8

[a] Based on current density of about 0.038 A/cm^2.

[b] Based on at least 10 cycles at the 5-hr discharge rate.

[c] Decline from maximum at 5-hr discharge rate.

[d] Arbitrarily chosen for comparison purposes.

The performance and lifetime for six Li-Al/FeS bicells (I-series) are listed in Table IV-2. The design for these cells was similar for the pairs I3B1 and I3B2, I3C1 and I3C2, and IB4 and IB6; the design variations among these three pairs included electrode thickness, capacity loading, and thickness of the positive terminal rod. As can be seen in this table, the average performance and lifetime for these cells meet the projected performance and lifetime for the Mark IA bicell, except for the energy and specific power. The energy difference (0.11 *vs* 0.15 kW-hr) is not considered to be significant, especially since an energy of 0.40 kW-hr has been achieved by multiplate Li-Al/FeS cells built for the Mark IA program. The specific power of the Mark IA multiplate cells has also been significantly improved by advances in technology, and the incorporation of these advances into the bicell design should result in higher specific power.

Table IV-2. Performance and Lifetime of I-series Li-Al/FeS Bicells

Cell No.	Sp. Energy,[a] W-hr/kg	Vol. Energy,[a] W-hr/L	Sp. Power,[b] W/kg	Energy, kW-hr	Cycle Life
I3B1	64	164	-	0.13	896
I3B2	60	130	23	0.10	505
I3C1	44	102	27	0.076	222
I3C2	62	140	-	0.11	527
IB4	62	154	-	0.12	1273
IB6	62	154	23	0.12	782
Avg.	59	140	24	0.11	700
Projected for Mark IA Bicells	50	115	35	0.15	700

[a]Based on a current density of about 0.038 A/cm^2.

[b]Peak power sustainable for 15 sec at 50% depth of discharge; measurements made for only one cell of each design pair.

B. Cell Status Tests
(H. Shimotake)

Two sets of ten status cells, one with BN felt separators and the other with MgO powder separators, are being built. These cells are being tested to obtain performance and lifetime data on at least six similar cells. For each set of cells, we are using consistent electrode pressing and cell assembly techniques, and all operating conditions will be held constant. The results from these tests will be used to establish the status of the development of various cell designs and to aid in the selection of the optimal design for the Mark II battery.

1. Cells with Felt Separators
(F. J. Martino, W. Moore*)

For these tests, ten Li-Al/FeS bicells are being built with a design similar to that of M-8 (see ANL-78-94, pp. 122-125). The essential features of this cell are as follows: separator of BN felt, initial positive capacity density of 1.4 A-hr/cm^3 at full charge, no additives to positive electrode, and a 67 mol % LiCl-33 mol % KCl electrolyte. This particular cell design was chosen because of this cell's performance. After 350 cycles, Cell M-8 had only an 8% decrease from the initial specific energy (60W-hr/kg at the 4-hr rate). This rate of specific energy decline is well below the Mark II goal of <20% after 500 cycles. Recently, this basic cell design was used for a multiplate cell (see Section III.B), which demonstrated similar performance stability after 110 cycles to that of the bicell.

The electrodes for the status cells will be fabricated by the cold-pressing technique, the positive electrode having a theoretical capacity of 123 A-hr and the negative electrode having a theoretical capacity of ∿170 A-hr.

2. Cells with Powder Separators
(T. W. Olszanski, C. Ruiz†)

For these status tests, ten Li-Al/FeS bicells are being built with a design similar to that of PW-16 (ANL-78-94, p. 134). The essential features of this design are as follows: separator of MgO powder, initial positive capacity density of 1.1 A-hr/cm^3 at partially charged condition, no additives to positive electrode, and a 67 mol % LiAl-33 mol % KCl electrolyte. The performance of this cell is discussed in greater detail in Section III.B.

C. Failure Mechanisms
(J. E. Battles)

Post-test examinations are conducted on engineering-scale cells (fabricated by industrial contractors and by ANL) to determine cell failure mechanisms, in-cell corrosion reactions, and electrode morphology (*i.e.*, microstructure, active material distribution and utilization, reaction uniformity, impurities, and cross-contamination of electrodes). These results are evaluated, and appropriate recommendations are made for improving cell performance and lifetime.

1. Cell Failure Mechanisms

Post-test examinations have been completed on 22 multiplate cells fabricated by Eagle-Picher for the Mark IA battery program and 20 bicells fabricated by ANL and industrial contractors; the results of these examinations are discussed below.

---

*Student from Illinois Institute of Technology.

†University of Puerto Rico.

a. Multiplate Cells
(F. C. Mrazek, N. C. Otto, J. E. Battles)

Twenty-two multiplate cells were examined; operation was terminated because of electrical short curcuits in 12 cells and declining coulombic efficiency in seven cells.* Three cells had completed the scheduled testing without failure. A summary of the failure mechanisms is listed in Table IV-3. A short circuit (or partial short circuit) was identified in each of the cells whose operation was terminated due to declining coulombic efficiency; one of the cells that had reached the end of testing was also found to have developed short circuits. Therefore, 20 of the multiplate cells had developed short circuits.

Table IV-3. Cell Failure Mechanisms for Multiplate Cells

Causes	No. of Cases
Extrusion of active material from positive electrode	7
Short circuit in electrical feedthrough	4
Metallic deposits in separator	3
Equipment malfunction	3
Difficulty in cell assembly	2
Rupture in separator	1
End of test[a]	3

[a]One of these cells was found to have a short circuit which was caused by a metallic deposit in the separator.

In the seven cells with extruded active material, five of them developed a short circuit at the cell bottom where the material extruded through a rupture in the retainer screen and the overlapping BN fabric cups and made contact with the cell can. This rupture is apparently caused by the bulging of the edges of the cell cans, which act to restrain the electrodes and the BN fabric cups. The bulging of the cell cans has been attributed to gas pressure (see Section III.C.2). In the remaining two cells, one developed a short circuit at the top where extrusion forced the retainer screen into contact with a retainer plate at the top of the negative electrodes, and the other cell short-circuited near the bottom where it appears that the retainer screen of the positive electrode ruptured and the broken wires were forced through the separator.

*Generally indicative of a developing short circuit.

Four cell failures have been caused by short circuits in the electrical feedthroughs. In three feedthroughs, the short circuits were across the top of the upper insulator and were caused by corrosion due to the presence of electrolyte in this area. The electrolyte was apparently from a source outside of the feedthrough since there was no evidence of electrolyte migration through the BN powder seal. In the fourth feedthrough, the short circuit occurred because the lower insulator had broken, apparently during fabrication.

Metallic deposits across the separator were the cause of short circuits in three cells. The wetting agent $LiAlCl_4$ (see ANL-78-94, p. 158) was used on the separator of two of these cells. The amount of $LiAlCl_4$ used was greater than needed to obtain electrolyte wetting of the separator, thereby resulting in significant metallic deposits as the $LiAlCl_4$ dissociated and/or was reduced by lithium. This effect has not been observed in other cells that used the minimum amount of the wetting agent. The short circuit in the third cell was caused by a combination of Li-Al, copper, and iron deposits across the separator, and was probably initiated by the cell evacuation during the electrolyte filling process.

Appendix B.1 provides a summary of the post-test examination for each of the multiplate cells. The following general observations were made from the post-test examinations: the typical negative electrodes expanded in thickness by 20-25%, the separators and negative electrodes were deficient in electrolyte, and varying degrees of Li-Al agglomeration occurred in the negative electrodes. Electrolyte deficiency and Li-Al agglomeration are believed to be important factors in the capacity decline observed in these cells (see Table IV-1).

b. Bicells
(F. C. Mrazek, N. C. Otto, J. E. Battles)

During this period, 20 engineering bicells (fabricated by both ANL and industrial contractors) were subjected to post-test examinations. A summary of the cell failure mechanisms is presented in Table IV-4; this table also includes all vertical prismatic cells that have undergone post-test examination to date. Cell operation has been terminated principally because of electrical short circuits, although in a few cases loss of capacity, broken conductors, or declining coulombic efficiency were the causes. A more detailed description of the causes of bicell failure is provided in Appendix B.2.

For the combined total, the major causes of short circuits are extrusion of active material (25 cells), cutting of separators by the honeycomb current collector (22 cells), and cell assembly difficulties (12 cells). Most of the cells with cut separators were fabricated before the recommendation had been made to add protective screens, which have proved effective in preventing this problem. Extrusion of active material appears to have been solved in the cells with newer designs. Cell assembly difficulties included misaligned (or broken) electrodes, misplaced (or skewed) separators, and contact of ZrO_2 cloth (conductive after reaction with lithium) with both electrodes; as can be seen in the column of cell failure mechanisms for this report period, cell assembly problems appear to

Table IV-4. Failure Mechanisms of Bicells

Mechanism	Number of Cases		
	This Period	FY 78	Total[a]
Extrusion of active materials (inadequate confinement)	3	5	25
Metallic copper deposits in separator[b]	1	3	13
Separator cut by honeycomb current collector	2	11	22
Equipment malfunction[c]	0	2	10
Short circuit in feedthrough	2	4	9
Cell assembly difficulties	0	10	12
Broken positive-electrode conductor	0	0	2
Declining coulombic efficiency	2	1	11
Unidentified short circuits	0	3	5
Loss of capacity & poor utilization	2	3	5
Metallic[d] and/or sulfide deposits across separator	2	4	9
End of test	4	6	12
Ruptured BN felt separator & non-uniform expansion of electrodes	2	0	2
TOTAL	20	52	137

[a]All cells that have undergone post-test examinations to date.

[b]FeS cells with Cu_2S additive; one cell used a copper current collector.

[c]Overcharge, temperature excursion, or accidental polarity reversal.

[d]Other than copper.

have been resolved, mainly as a result of better quality control. In summary, the major causes of cell failure before this report period appear to have been eliminated by modifications in cell design and better quality control. The mechanism involved in the loss of capacity is being studied, but has not been identified as yet.

2. Copper Deposition in Electrode Separators
(N. C. Otto, J. E. Battles)

Copper sulfide is being added to the positive electrode of Li-Al/FeS cells to improve performance. However, post-test examinations have shown that copper deposits in the electrode separator cause declining coulombic efficiency, and in some cases complete short circuits. Microscopic examinations have determined that elemental copper is precipitated in the separator, but mechanism(s) for the phenomena is unknown at this time. This reaction is assumed to continue as long as the cell is cycled, ultimately resulting in cell failure.

Seven Eagle-Picher bicells* were examined to determine the depth of copper penetration into the electrode separator and the morphology of the copper deposits. In cells with short operating times (<208 days), the copper particles are generally about 5 μm in diameter and rather densely arranged within the separator (no more than about 500 μm from the positive electrode). The electrolyte in this same area has a pronounced copper hue under polarized light, thereby indicating the presence of a significant amount of sub-microscopic sized copper particles. This observation has been confirmed by scanning electron microscope (SEM) examinations. The depth of copper penetration into the separator is generally fairly uniform. In cells with longer times of operation, the copper particles are generally slightly larger and the depth of penetration more variable. Also, the copper hue of the electrolyte under polarized light is much less pronounced, thus indicating fewer sub-microscopic particles.

Figure IV-1 shows the penetration of copper into the separator (*i.e.*, across the separator thickness) found in these seven cells at post-test examination; as can be seen in this figure, the copper penetration increases with increasing cell operating time. This copper deposition probably causes a decline in coulombic efficiency when the amount present reaches a sufficient level. Chemical analyses will be performed to determine whether the amount of copper in the separator also increases with cell operating time; metallographic evidence suggests that the amount of copper deposited in the separator per cycle decreases with an increase in operation time.

In most cells the BN cloth separator is compressed to about 1.6 mm in thickness after a short period of cell operation. If this observation is assumed to be true, then the data in Fig. IV-1 indicate complete penetration of the separator in slightly less than 20,000 hr (833 days). Thus, this type of cell cannot be expected to operate longer than approximately two years before a substantial decrease in coulombic efficiency occurs. For a cell with a BN felt separator, which normally has a compressed thickness of 1.0 mm, the expected cell lifetime would be even shorter, about 10,000 hr (420 days).

---

*These are Li-Al/FeS-Cu_2S bicells with BN fabric separators.

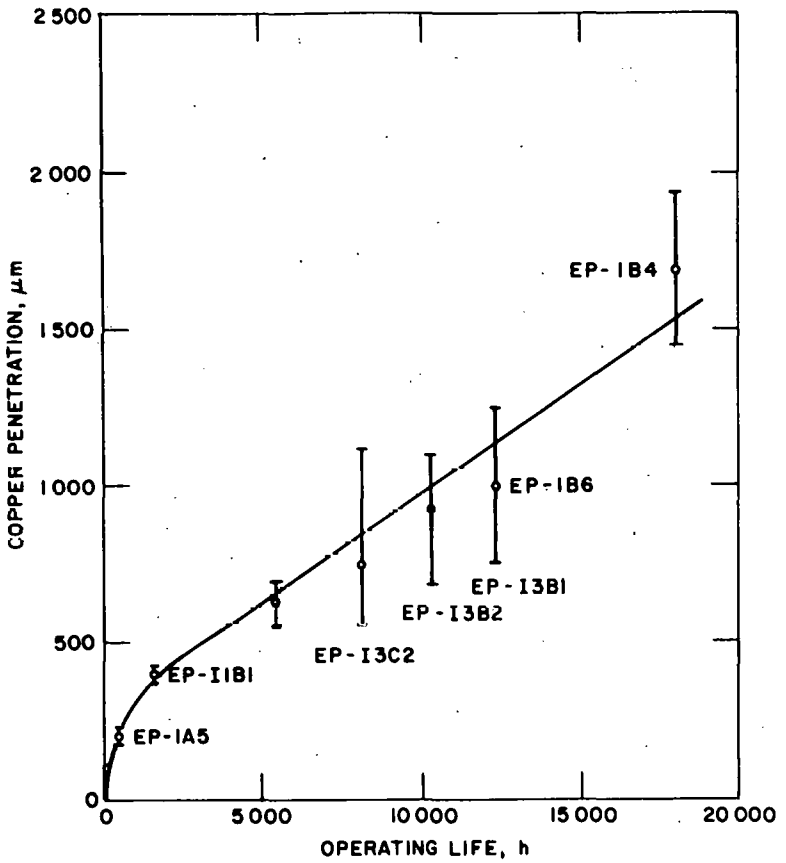

Fig. IV-1. Penetration of Copper into Separators of Li-Al/FeS-Cu_2S Cells

3. Lithium Gradient in Negative Electrodes
(F. C. Mrazek, J. E. Battles)

Previous (ANL-77-35, p. 44) metallographic and chemical analyses indicated that a significant lithium concentration gradient existed in some Li-Al electrodes; this observation was confirmed by ion microprobe mass analysis (IMMA)* of Li-Al electrodes from bicells (ANL-78-94, p. 160). The results showed that the lithium concentration across the thickness of the electrode was fairly uniform in a discharged electrode, and exhibited a substantial lithium gradient in charged electrodes (*i.e.*, lithium enriched in the front portion of the electrode). During this period, a similar study was conducted on electrodes from two Eagle-Picher multiplate cells--EPMP-7-032 and -035. One cell was fully discharged (EPMP-7-035) at a current of 70 A, the other fully charged (EPMP-7-032) at a current of 40 A.

---

*Performed by D. V. Steidl, Chemical Engineering Division at ANL.

Determination of the lithium gradient for the metallic Li-Al structure in a matrix of LiCl-KCl electrolyte is very difficult. Variations in the Li-Al ratio within the electrode prevent bulk chemical analyses, and the microscopic examination is not quantitative since the optical difference is negligible for Li-Al containing between 10 at. % and 50 at. % lithium (the lithium concentration normally occurring in cycled negative electrodes). The only method or instrument capable of determining the Li to Al ratio within the Li-Al structure is IMMA.

Figures IV-2a and -2b show the microstructures of the charged and discharged electrodes, respectively. (The white region is Li-Al, the grey is electrolyte, and the black is void.) The charged electrode shows the typical skeletal microstructure found in cycled Li-Al electrodes; an enlarged view of this fine metallic structure is shown in Fig. IV-2c. This electrode also showed considerable Li-Al agglomeration in the center; an enlarged view of this agglomeration is shown in Fig. IV-2d. In the discharged electrode (Fig. IV-2b), the center portion showed considerable evidence of the original Li-Al particles indicating this region has experienced little or no cycling.

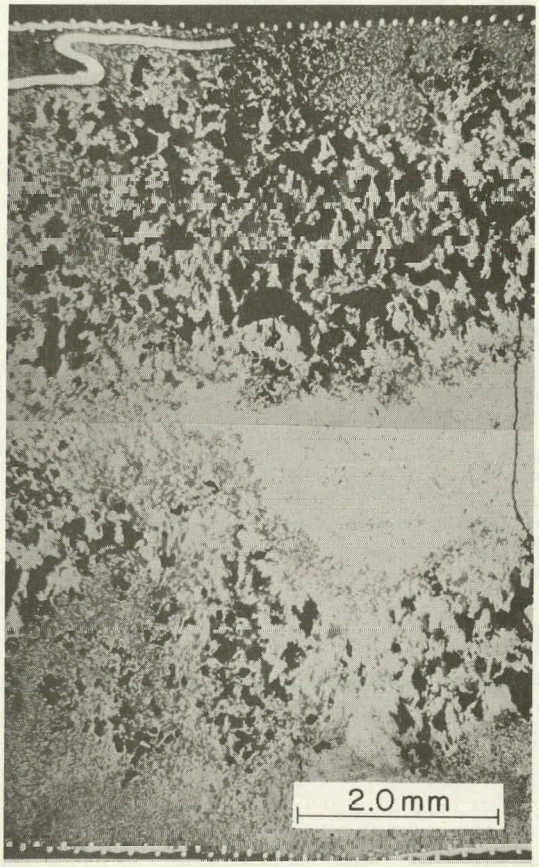

a. Full thickness of the charged electrode.

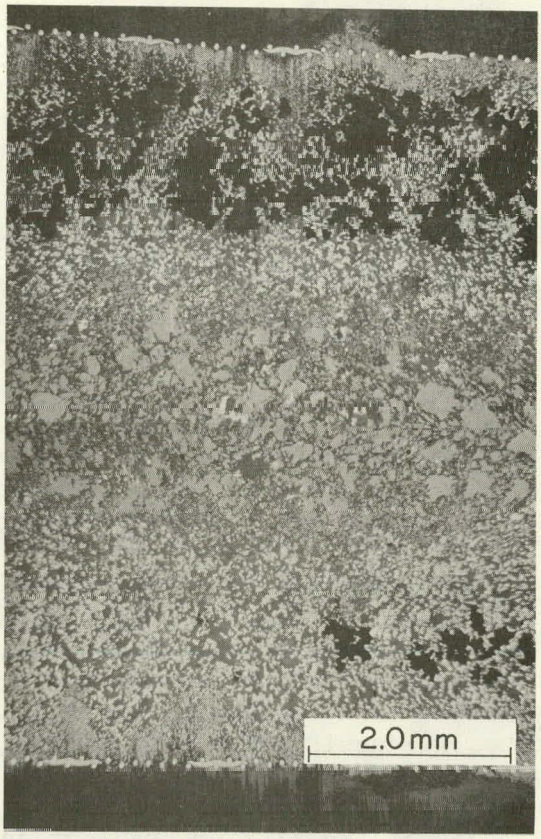

b. Full thickness of the discharged electrode.

Fig. IV-2. Microstructure of Charged and Discharged Negative Electrodes

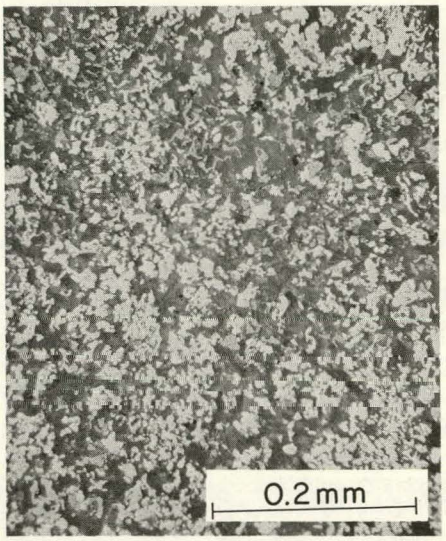

c. Example of the typical fine metallic structure observed in negative electrodes

d. Example of the agglomerated metallic structure

Fig. IV-2 (Contd)

Microstructure of Charged and Discharged Negative Electrodes

The results of the IMMA analysis for lithium gradients are shown graphically in Figs. IV-3 and -4 for the charged and discharged electrodes, respectively. The morphologies of the cross-sectional areas selected for IMMA analysis are not typical of the total electrodes, but were intentionally chosen to show the undesirable effects of Li-Al agglomeration. In the fully charged electrode (Fig. IV-3), a low lithium concentration (10-20 at. %) was found in the agglomerated Li-Al in the central portion of the electrode, and the area near the electrode face was enriched in lithium. Once agglomeration had occurred, lithium transport into and out of these massive metallic areas during cycling was comparatively slower than that for the low-density, skeletal structure which is normally present. In the fully discharged electrode (Fig. IV-4), the middle portion showed a high lithium concentration, while the remainder was fully discharged ($\sim$8 at. % Li). The slopes of the lithium gradient appear more gradual in the charged electrode (Fig. IV-3) than in the discharged electrode (Fig. IV-4), presumably because of the additional time allocated for charging.

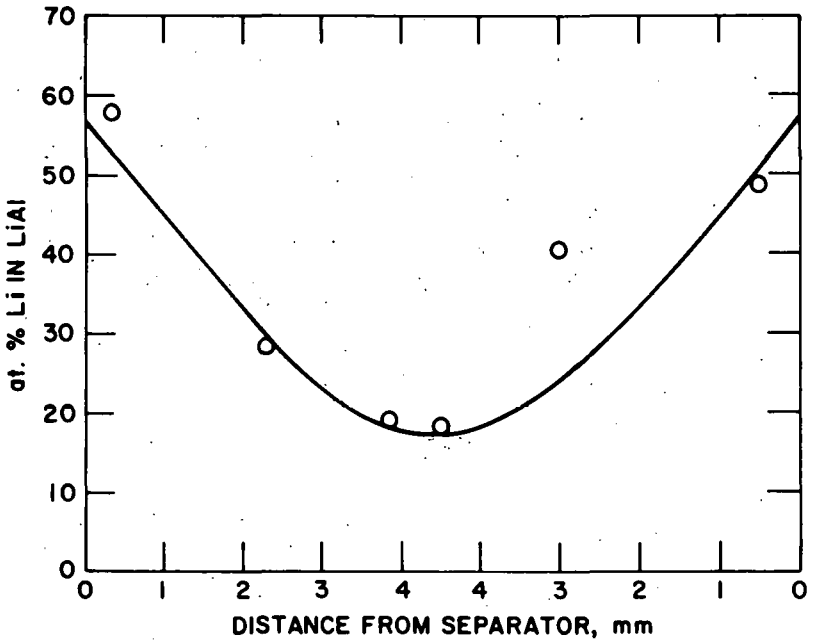

Fig. IV-3. Lithium Gradient in Negative Electrode from Charged Cell (EPMP-7-032)

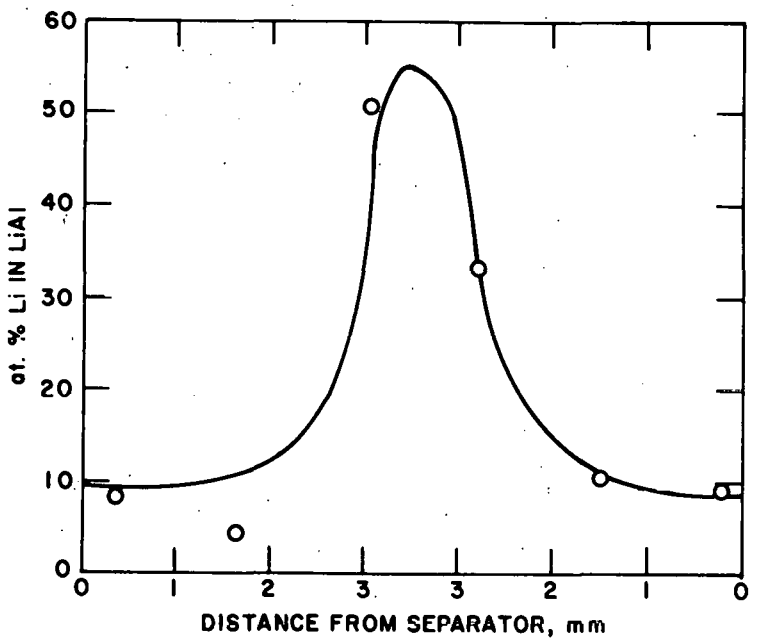

Fig. IV-4. Lithium Gradient in Negative Electrode from Discharged Cell (EPMP-7-035)

The mechanism for the agglomeration of Li-Al is unknown at this time. This behavior is unusual since an initially solid Li-Al electrode will form the typical skeletal microstructure during normal cycling. Also, the retention of lithium in the center portion of the discharged electrode is unusual. Both conditions could be factors in capacity loss observed in multiplate cells, since the charge and discharge cut-off potentials would be reached before complete utilization of the lithium. Additional analyses of the type described above should provide further insights into the causes of Li-Al agglomeration and lithium concentration gradients in Li-Al/FeS cells.

V. CELL DEVELOPMENT

Developmental efforts are in progress to improve the performance of the Li-Al/FeS cell for electric-vehicle applications. Studies conducted in this report period include the following: development of a cell model that relates cell performance to design characteristics and mode of operation, development of reference electrodes for polarization measurements in cells and other electrochemical data, and tests of small-scale and engineering-scale cells to determine optimum cell designs.

A. Cell Modeling Studies

(E. C. Gay, W. E. Miller, F. J. Martino)

Engineering cell modeling studies were conducted with the objective of developing empirical equations that relate cell performance to the design characteristics of the cell and the mode of cell operation. Design characteristics that affect cell performance include electrode thickness, active material composition, state of charge, volume fraction of electrolyte in the electrode, separator properties, cell resistance, and cell compactness. Operating modes that affect performance include charge and discharge cutoff voltages, charge and discharge rates, and temperatures.

For this model, very general empirical equations were developed to fit FeS and FeS_2 bicell and multiplate cells, the coefficients in the equations being determined by multiple regression analysis. This model, and a check of its accuracy, are described below. Future modeling studies will be directed to developing equations that relate cycle life to cell design and operating mode.

1. Model Development

The model to predict cell performance (*i.e.*, specific energy and specific power) was developed from the performance of the following engineering-scale Li-Al/FeS and Li-Al/FeS_2 bicells: 19 Eagle-Picher bicells, 5 ANL bicells,* and 2 Gould bicells. Multiple regression analyses were used to develop equations of the general form,

$$\hat{y} = b_0 + b_1x_1 + b_2x_2 + b_3x_3$$

where b_0, b_1, b_2 and b_3 are constants; x_1, x_2 and x_3 are independent cell design or operating variables, and $\hat{y}$ is the dependent variable.

The range of values of the variables that were used in the model is shown in Table V-1. Using multiple regression analysis, we developed the following equation to predict the cell specific energy (W-hr/kg):

$$\begin{aligned} SPE = {} & 2.0710 - 0.37414FSUBL + 14.408TSUBLR \\ & - 1.2149VOLT1R - 1.0586\ VOLT2R \\ & + 1.4718F/LMUL - 20.790LTLV1R + 47.968LOGV1R \end{aligned} \quad (1)$$

*These are M-series and KK-series bicells (see Section III.B).

Table V-1. Variables Used in the Regression Analysis for Cell Model

Cell Variable	Range
Fraction of Charge	0.05-1.0
Electrode Area	270-1806.5 cm
Separator Thickness	2.0-6.4 mm
Limiting Electrode[a] Thickness	0.20-0.63 cm
Counter Electrode Thickness	0.25-1.0 cm
Average Cell Resistance	1.7-13.3 mΩ
Discharge Current Density	0.01-0.18 A/cm^2
Charge Current Density	0.03-0.04 A/cm^2
Limiting Electrode Capacity Loading	0.64-1.45 $A\text{-}hr/cm^3$
Cu_2S Composition[b]	0-25 wt %

[a] If the positive electrode limits capacity, then its half-thickness is used for this factor (the thickness of two negative electrodes equals that of one positive electrode).

[b] An additive used in the positive electrode to improve performance.

where FSUBL = F/L = percent utilization of the limiting electrode*

TSUBLR = TL = limiting electrode thickness/separator-retainer thickness

VOLT1R = V1R = OCV - DCO/$A_e i_D \bar{R}_c$ †

VOLT2R = CCO - $A_e i_D \bar{R}_c$ - DOC/$A_e i_c \bar{R}_c$ †

MUL** = 0.01 (theor. cell capacity) (OCV - DCO)/cell weight

F/LMUL = product of F/L and MUL

LTLV1R = natural logarithm of product TL and V1R

LOGV1R = natural logarithm V1R

* The electrode that limits cell capacity.

† OCV is the open-circuit voltage (V); DCO is the discharge cutoff voltage (V); A_e is the limiting electrode area (cm^2); i_D is the discharge current density (A/cm^2); and R_c is the average cell resistance (Ω).

‡ CCO is the charge cutoff voltage (V) and i_c is the charge current density (A/cm^2).

** This is the only parameter that is not dimensionless (W-hr/kg).

For the specific power (W/kg), the multiplate regression analysis produced the following equation:

$$\text{LOG (SP)} = 0.28259 + 0.86170 \text{ LOG (PF)} + 0.12012 \text{ LOG (CF)} + 0.31889\text{FCCF} \quad (2)$$

where PF = $(\text{OCV})^2/(4\bar{R}_c W)$*

CF = charge factor†

FCCF = fully charged correction factor‡

2. Check of the Model

As can be seen in Figs. V-1 and -2, the calculated and measured performance for the cells used in the multiple regression analysis are in good agreement. As a further check of the model, the performance of five Li-Al/FeS multiplate cells (four fabricated by Eagle-Picher and one by Gould) and 11 upper-plateau Li-Al/FeS bicells (fabricated by Gould) was determined, and these values compared with those predicted by the model. As

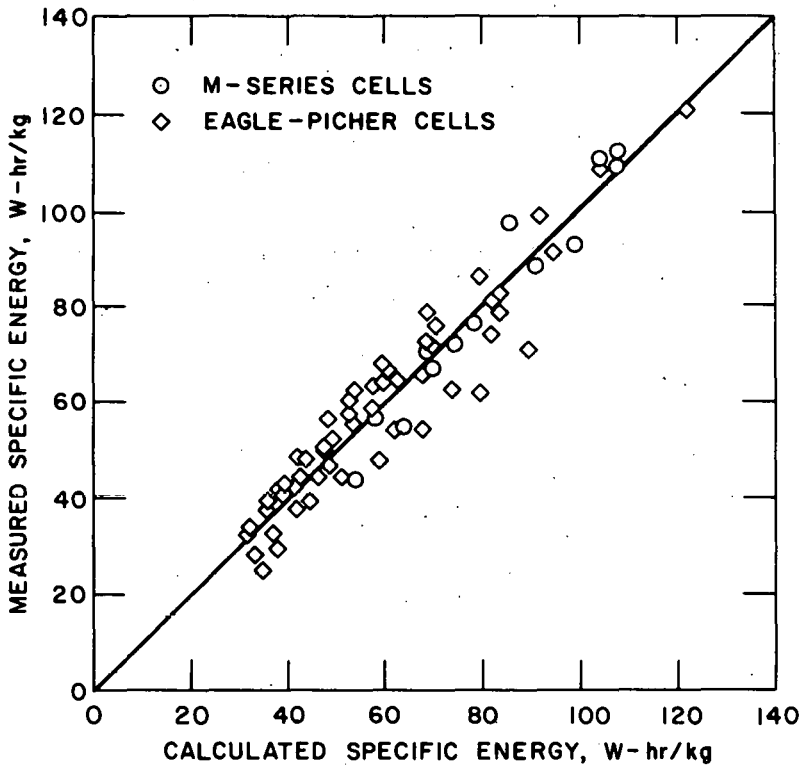

Fig. V-1. The Measured and Calculated Specific Energy for 26 Lithium/Metal Sulfide Cells Used in the Multiple Regression Analysis

*OCV is the open-circuit voltage (V); $\bar{R}_c$ is the average cell resistance (Ω); and W is the cell weight (kg). PF is in dimensions of W/kg.

†This factor is assumed to be 1.0 at full charge, 0.5 at 50% discharge, and 0.05 at full discharge, *i.e.*, discharged to the cutoff voltage which is normally 0.9-1.0 V.

‡This factor is assumed to be 1.0 at full charge and 0.05 at any state of discharge.

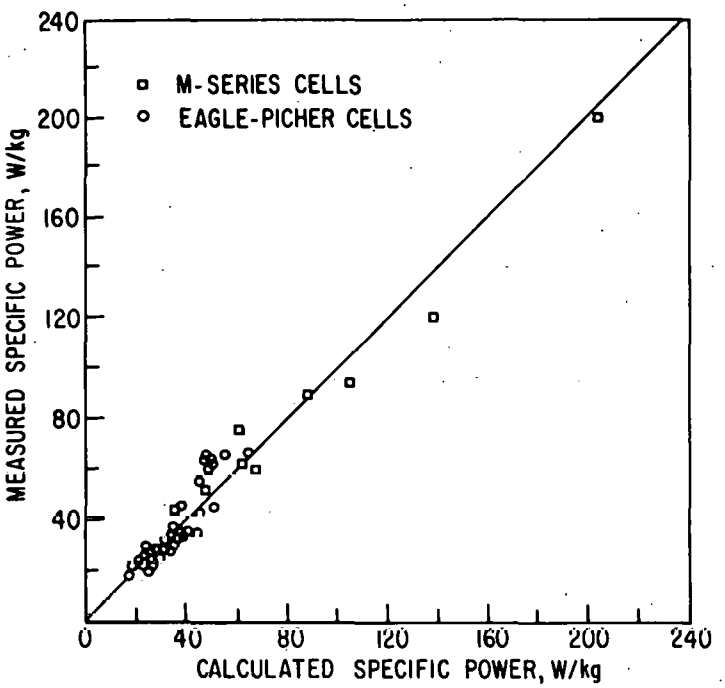

Fig. V-2. The Measured and Calculated Performance for 26 Lithium/Metal Sulfide Cells Used in the Multiple Regression Analysis.

can be seen in Figs. V-3 and -4, there is good agreement between the predicted and the actual performance of these 16 cells. Statistical analysis of the error included normal distribution and scatter tests, both of which gave favorable results.

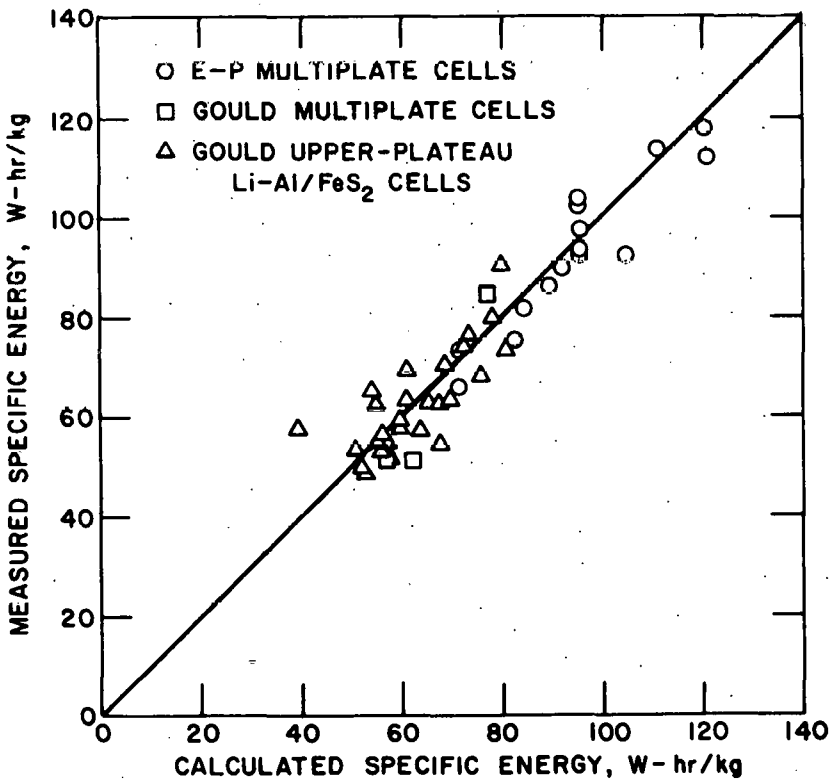

Fig. V-3. Calculated and Measured Specific Energy of 16 Lithium/Metal Sulfide Cells Not Used in Development of the Model

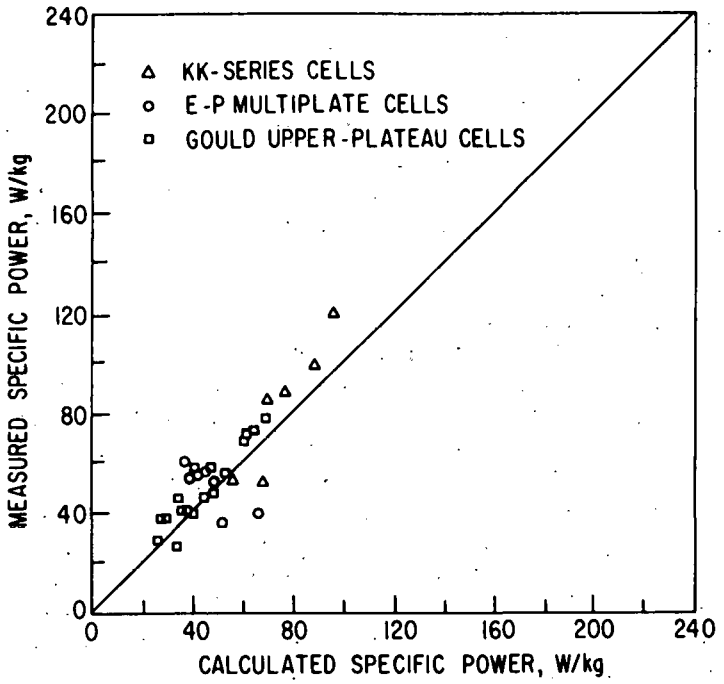

Fig. V-4. Calculated and Measured Specific Power of 16 Lithium/Metal Sulfide Cells Not Used in Development of the Model.

B. Reference Electrode System
(L. Redey*)

Small-diameter (3 mm) reference electrodes have been developed for polarization measurements in engineering cells and for other electrochemical investigations.

1. Development

The reference electrodes must be electrochemically stable, and possess a suitable geometry with adequate mechanical strength. Long-term stability tests have been completed on five electrode couples: Li-Al/Li^+, Li-Bi/Li^+, Ni/Ni_3S_2/$S^=$, Ag/Ag_2S/$S^=$, and Ag/AgCl. In some cases these systems have been investigated by others[4-7]. All potential values presented in this section are given *vs* the two-phase ($\alpha + \beta$) Li-Al (40-45 at. % Li) alloy electrode.[4] Large (3 to 5 A-hr) Li-Al electrodes were found to show a very stable potential in LiCl-KCl melts, but were impractical as reference electrodes because of their size.

On the basis of these tests, the Ni/Ni_3S_2 system was found to be the most suitable for the reference electrode couple. This reference electrode was fabricated using BeO tubing (0.3-cm dia) and a Y_2O_3 diffusion barrier; the design is shown in Fig. V-5. The Ni_3S_2 can be formed spontaneously on the surface of nickel wire in LiCl-KCl eutectic saturated with Li_2S, and the Ni/Ni_3S_2 couple reaches a stable potential within 2-3 days. With intermittent anodic polarization, one can develop a more stable electrode in a couple of hours. The electrochemical system used in this study can be described as follows:

* Technical Institute of Budapest.

$Ni/Ni_3S_2/LiCl\text{-}KCl$, Li_2S (sat'd)/LiCl-KCl/Li(Al)/Fe

The value of the mean potential at 425°C for four Ni/Ni_3S_2 reference electrodes was 1.3605 V. We have been collecting information on this system for about nine months. Taking the extreme values observed during our experiments into consideration, the uncertainty of the mean is less than ±1.5 mV. The potential shift was usually not more than a few tenths of a millivolt per day and was within a ±0.5 mV range for the individual electrodes.

Although the Ni/Ni_3S_2 electrode has a stable potential during long-term tests (6 months), a slow potential shift could influence the accuracy of the measurements. To avoid this uncertainty, a second electrode system, aluminum wire intermittently charged with lithium, will be used to obtain a well-defined potential. This charging technique can be characterized by the potentials recorded during the procedure (see Fig. V-6). The constant potential value indicated by the consecutive steady-state, open-circuit values correspond to the well-defined potential of the two-phase Li-Al alloy. This series of potential values can be obtained with a reproducibility of ±1 mV on new aluminum wires or on the same wire with the consecutive charging procedures. After a period of time, depending on the quantity of lithium deposited, the steady-state potential of this alloy electrode shifts up toward positive values, but a repeat of the intermittent charging technique can again achieve the well-defined value.

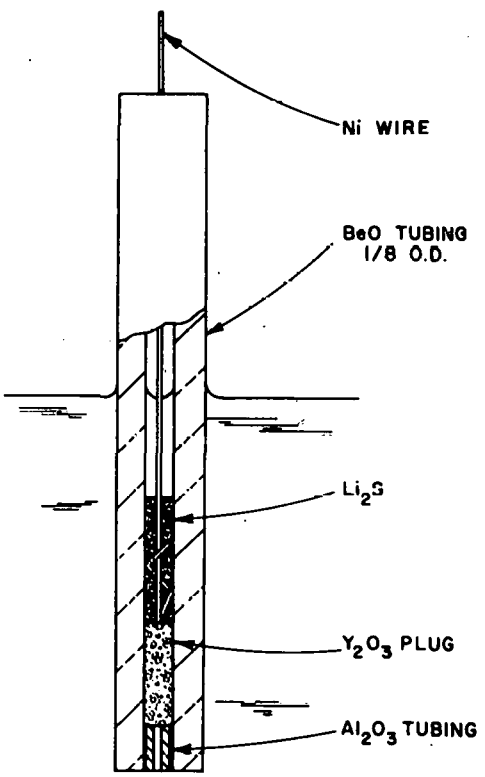

Fig. V-5. Reference Electrode Design

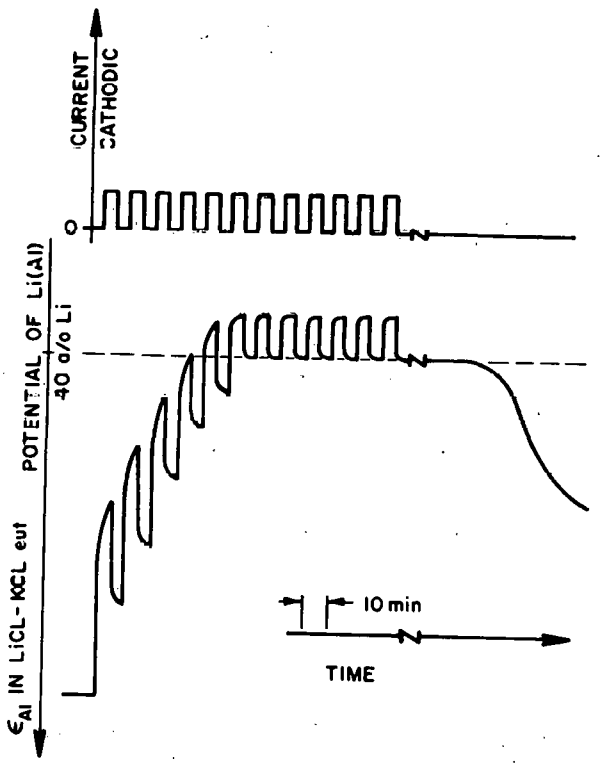

Fig. V-6. Typical Diagram Obtained During Intermittent Charging of an Al Wire With Li

2. Application
(F. J. Martino, K. E. Anderson, L. Redey)

Measurements will be made with reference electrodes in three different size cells: large- (~100 A-hr) and intermediate-scale (5-15 A-hr) prismatic cells and small tubular cells. To evaluate the polarization of the electrodes in the large engineering cells, an automatic data acquisition system (DAS) is being built. The DAS can be programed to obtain either IR-free or IR-included potential data, as well as the relaxation characteristics of the electrodes as a function of current, state of charge, and cycle number.

Eight reference electrodes have been incorporated into a bicell with a design similar to that of M-8 (Section III.B). The reference electrodes are positioned at various levels and locations relative to the positive and negative electrode interface. The information obtained from these studies will be valuable in future cell designs and will also be used to determine single reference electrode placement in future engineering cells for routine electrode polarization measurements aimed at identifying the limiting cell electrode.

A Ni_3S_2 reference electrode has been placed at the interface of the electrodes in an intermediate-scale LiAl(12 A-hr)/FeS_2(10 A-hr) cell with horizontally mounted electrodes. Measurements made with this reference electrode are being used to investigate the performance and capacity retention characteristics of the Li-Al/FeS_2 system. Preliminary results indicate the following: (1) when the cell was operated at 25 mA/cm^2, the capacity was limited by the positive electrode, and (2) no capacity decline occurred during the first 14 cycles (cutoff voltages of 1.9 and 1.0 V for charge and discharge, respectively). The reference electrode system seems to be working perfectly.

Small (0.6-cm dia) tubular-type cells, which contain reference electrodes, are being developed to obtain electrochemical cell data, *e.g.*, electrode polarization and current distribution for a one-dimensional cell model being developed by J. Newman and R. Pollard.[8] Data obtained from the model will be used to help optimize large-scale engineering cells.

C. Parametric Studies
(H. Shimotake, F. J. Martino, L. G. Bartholme, K. E. Anderson)

Cell tests are in progress to optimize the performance of the Li-Al/FeS cells; some of the tests conducted during this report period are discussed below.

1. Small-Scale Cell Studies

Studies have been conducted on 11.3 A-hr Li-Al/6.5 A-hr FeS cells containing the following amounts of Cu_2S additive to the positive electrode (in wt %): 0, 5, 10, and 20. In addition, a small-scale Li-Al/Cu_2S cell was tested for comparison purposes. All of these cells had LiCl-KCl eutectic electrolyte and were operated at current densities of 50 to 200 mA/cm^2.

The results of these tests indicated that increasing the Cu_2S concentration in the positive electrode increased its utilization. In addition, at current densities above 100 mA/cm^2, the positive-electrode utilization decreased only slightly with increased current density. The Li-Al/Cu_2S achieved the highest utilization (~90%) of the cells tested, and the current density had almost no effect on utilization.

Another small-scale cell was tested to determine the effect of LiCl-rich electrolyte (54 wt % LiCl-KCl) on the performance of a Li-Al/FeS-10 wt % Cu_2S cell. The results indicated that the positive-electrode utilization of this cell was about the same as that of similar cells containing the eutectic electrolyte. It should be cautioned that the cell with the LiCl-rich electrolyte was operated in the flooded state (*i.e.*, a large excess of electrolyte), which may have eliminated the benefits obtained from using the Cu_2S additive.

2. Engineering-Scale Cells

During start-up, R- and M-series bicells* are cycled at discharge current densities of 37, 74, and 110 mA/cm^2 (which correspond to discharge rates of about 8-, 4-, and 2-hr, respectively). Fig. V-7 shows the positive-electrode utilization as a function of discharge current density for these two series. Of the five M-series cells, M-8 (LiCl-rich electrolyte, 1.4 A-hr/cm^3 loading) is much less dependent upon current density than its counterpart, Cell M-11 (LiCl-rich electrolyte, 1.6 A-hr/cm^3 loading) or the other three M-series cells, M-9 (Cu_2S additive, 1.6 A-hr/cm^3 loading), M-10 (no additive, 1.4 A-hr/cm^3) and M-12 (Cu_2S additive, 1.4 A-hr/cm^3 loading). This effect is probably due to the high electrolyte volume fraction (0.49) of Cell M-8.

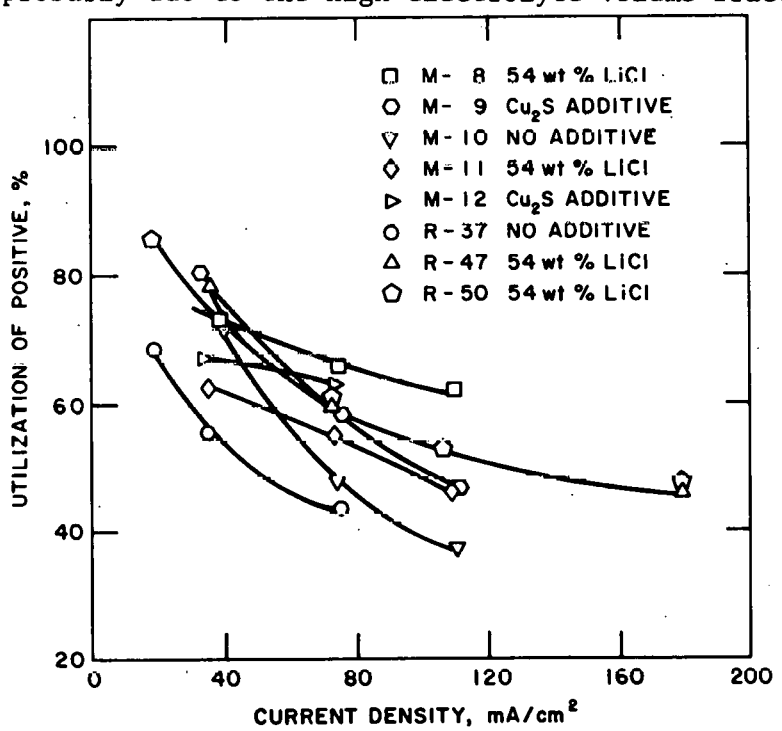

Fig. V-7. Utilization *vs* Current Density of FeS Cells

*Performance data and design description of these cells are presented in Section III.B.

To test the effect of positive-electrode thickness on active-material utilization, Cell R-50 was built with a design similar to that of R-47 (nickel current collector); the only significant difference between the two cell designs was that the positive-electrode thickness of R-50 was 20% less (same capacity loading) than that of R-47. Somewhat surprisingly, at any given current density, the positive-electrode utilization for both cells was about the same. However, since a given hourly discharge rate corresponds to a lower current density for a thinner-electrode cell, the active-material utilization of Cell R-50 was higher than that of R-47 for any given hourly discharge rate. Further tests are planned on the effect of positive-electrode thickness on utilization.

Typically, M-series cells achieve cell resistances of 3.1 to 4.5 mΩ (electrode area, 270 cm^2) depending on the state of charge. Prior to power pulse tests and intermittently during cycling, cell resistances are monitored through use of a 1-sec current interrupt. During these intervals, it is apparent that the cell resistance increases during discharge; a typical discharge may vary by 1 mΩ between 3% and 75% depth of discharge (as rated prior to power pulse tests). Cell resistance has also been found to increase during discharge for the R- and PW-series cells.

VI. MATERIALS AND COMPONENTS DEVELOPMENT

The objectives of this part of the program are (1) to provide solutions to chemical and electrochemical problems that arise in the development of cells and batteries, (2) to develop improved compositions for electrodes and electrolytes, (3) to acquire a basic understanding of the chemistry and electrochemistry of cells, and (4) to improve the performance of various cell components (*e.g.*, separators, current collectors, and other cell hardware).

A. Electrode Development

Cell-chemistry studies are being conducted on the Li-Al electrode and iron sulfide electrode. The studies performed during this period are reported below.

1. Studies of Li-Al Electrodes
(A. K. Fischer, K. E. Anderson)

Testing of multiplate cells has indicated a significant capacity decline with cycling (Section IV.A), and post-test examinations indicated that the capacity decline may be partly due to metallic agglomeration in the center of the Li-Al electrodes (Section IV.C.1). Studies of the lithium gradient in a discharged negative electrode from a multiplate cell indicated a high lithium concentration in this agglomerated region (Section IV.C.4); thus it is believed that not all of the lithium had been consumed in cell reactions when the cutoff voltage had been reached. The formation of the agglomerated Li-Al is believed to be due to pressure changes, which arise from the formation of less dense Li-Al from the denser aluminum in the electrode. A ratchetting effect on the pressure is expected--the pressure increasing locally as Li-Al forms during charge and decreasing when lithium is lost during discharge.

To investigate Li-Al agglomeration further, we are operating cells having small working electrodes of solid aluminum* and large counter electrodes of porous Li-Al to eliminate any effects from metal sulfide. The polarization of the test electrode will be measured. Solid rather than porous electrodes are being studied because (1) a solid structure is more reproducible than a porous one and (2) the pressure changes that are suspected to cause the agglomeration are better trapped and their effects should be revealed more clearly if they cannot be relieved. The sequence of physical changes will be followed by metallographic examination of the solid electrodes from the cells at various stages of charge or discharge and after various numbers of cycles. The current density of charging and discharging will also be an important variable. In addition to yielding information on the morphology changes, the experiments will also provide information on the composite effect of the various diffusion processes that operate in the Li-Al electrode.

---

*Solid Li-Al electrodes will be investigated in later experiments.

Variations in electrolyte composition on the Li-Al electrode surface at different stages of charge and discharge have been predicted[9,10] and observed (ANL-75-1, p. 108). Precipitation of KCl as Li^+ ion as locally consumed during charging at an LiAl electrode is followed by dissolution of KCl on discharging. This process is seen as possibly involved in a pressure rise within the electrode that can lead to metallic compaction. Consequently, another important part of the study is the examination of morphology changes as a function of electrolyte composition.

Since hydrogen was recognized some time ago as a product of cell processes, some consideration was given to the implications of a recent study of the Li-Al-H system by the Fusion Reactor Research Group from the Chemical Engineering Division at ANL (ANL-78-42, p. 47). It was concluded that, at the observed hydrogen pressure ($\sim$30 torr), there is a strong likelihood that LiH would precipitate from the Li-Al electrode. The best cure for the problem is probably to take steps to remove hydrogen sources from the cells before assembly. This would entail thorough drying of materials, particularly the separators, of water and alcohol.

Studies are continuing on additives to the porous Li-Al electrode that may result in sustained high capacities during extended cycling. As mentioned previously, the decreasing capacity presently observed in Li-Al electrodes may be due, in part, to morphological changes of the active material during cycling. The present study is focused on the use of zinc additive (15 wt %) to the binary alloy as a means of controlling or modifying these morphological changes. Earlier preliminary studies have indicated that the morphology of the Li-Al-Zn electrode was much different from that observed for a Li-Al electrode. The particles of this zinc containing alloy electrode were coarser and appeared to have a three-dimensional structure that had better and more uniform electronic conduction pathways than those observed in the binary Li-Al alloy electrode.

The electrochemical performance (capacity density) of a LiAl-15 wt % Zn electrode was determined, and its capacity retention evaluated through 200 cycles. The cell design (see ANL-78-94, p. 182) utilized horizontally mounted electrodes, a LiAl-15 wt % Zn electrode with a theoretical capacity of 10 A-hr, and a liquid-lithium counter electrode with a theoretical capacity of 16 A-hr. In general, the cutoff potentials were 0.15 V during charge and 0.70 V during discharge (all cutoff potentials cited are IR-free voltage *vs* lithium). The capacity density of the electrode at constant current was used as a measure of electrochemical performance. The effect of the additive on the capacity retention of the electrode was assessed by measuring the rate of capacity-density decline at a current density of 0.05 A/cm^2 during cycling.

Performance data from this study, along with performance data from the first 50 cycles of a baseline binary LiAl alloy electrode which was investigated earlier (ANL-78-94, p. 183), are presented in Table VI-1. The lithium utilization achieved with the Li-Al-Zn electrode during the first 50 cycles was less than that achieved with the Li-Al electrode. After 200 cycles, the utilization of the Li-Al-Zn electrode dropped to a mere 28% of theoretical, whereas the Li-Al electrode had a utilization of 81% of theoretical at 200 cycles. These results clearly indicate that the 15 wt % zinc additive does not improve the performance of the Li-Al electrode. The

Table VI-1. Performance Characteristics of LiAl and Li-Al-Zn Alloy Electrodes During the First Fifty Cycles of Operation

Charge Rate, A/cm^2	Discharge Rate, A/cm^2	Capacity Density, $A\text{-}hr/cm^2$		Lithium Utilization, % of Theoretical	
		Li-Al	Li-Al-Zn	Li-Al	Li-Al-Zn
0.050	0.050	0.60	0.51	92.3	75.8
0.050	0.100	0.58	0.50	89.2	74.8
0.050	0.200	0.55	0.49	84.6	71.8
0.050	0.300	0.53	0.44	81.9	65.4
0.100	0.050	0.52	0.39	80.2	58.0
0.100	0.100	0.50	0.37	76.6	55.0
0.100	0.200	0.50	0.35	76.6	51.7
0.100	0.300	0.43	0.33	65.6	48.0

poor performance of the Li-Al-Zn electrode is very probably related to its coarse particle structure which creates a low particle surface area for lithium transport. This conclusion is in agreement with the performance improvements for the Li-Al electrode observed earlier with indium additives (ANL-78-94, p. 183), which tended to increase the surface area of the structure of the Li-Al electrode material. Future studies in this area will be directed toward the evaluation of the indium additive.

2. Chemistry of FeS Electrodes

(Z. Tomczuk, M. F. Roche)

Previous cell-chemistry studies of the FeS electrode (ANL-77-17, pp. 45-46) established that the initial discharge of FeS in LiCl-KCl eutectic electrolyte proceeded in four stages:

$$FeS \rightarrow LiK_6Fe_{24}S_{26}Cl \text{ (J phase)} \quad (1)$$

$$FeS \rightarrow Li_2FeS_2 \text{ (X phase)} \quad (2)$$

$$X \rightarrow Li_2S + Fe \quad (3)$$

$$J \rightarrow Li_2S + Fe \quad (4)$$

Attempts to establish the charge sequence, however, could not determine if X or J phase formed first on charge since both phases formed when electrodes containing Fe and Li_2S were charged. Nevertheless, the likely charge sequence was thought to be:

$$Li_2S + Fe \rightarrow X \rightarrow J \rightarrow FeS \rightarrow Fe_{(1-x)}S \quad (5)$$

The $Fe_{(1-x)}S$ phase was found only in cells which were overcharged (>1.6 V). Further cell-chemistry studies of the FeS electrode are reported below.

a. Cell Studies

In previous Li/FeS cell studies (ANL-75-1, p. 103), two plateaus were observed on the time *vs* current curves during charge, corresponding to the formation of J phase and FeS respectively. For a cell at 438°C and a current density of 21 mA/cm^2, the transition from J phase to FeS was reported to be 1.87 V *vs* Li or 1.57 V *vs* Li-Al. During discharge, only one plateau was observed on the time *vs* voltage curves for these cells; thus the potential of the FeS to J phase transition could not be measured. In studies performed in this report period, two 2 A-hr Li-Al/1 A-hr FeS cells (eutectic electrolyte) were operated at current densities of 6 to 12 mA/cm^2 and 444°C, and two plateaus were again observed on the time *vs* voltage curves during charge. The J phase to FeS transition was found to occur at 1.62 V, which is only slightly above that observed earlier. During discharge of the cell, two plateaus were seen in the time *vs* voltage curves; one of these plateaus was very short (∿7% of total capacity) and occurred at approximately 1.4 V. The short plateau is believed to be associated with the FeS to J phase transition, but the reason that it was not observed in the earlier studies is uncertain. It has been suggested that the higher current density used in earlier cells produced this discrepancy between the curves. The present results also suggest that there is a large overpotential associated with the J and FeS transition during charge.

A third cell utilizing an LiCl-LiBr-LiF electrolyte was tested to elucidate the phases formed in the FeS electrode when J phase is not present. When the LiAl/LiCl-LiBr-LiF/FeS cell was operated at 490°C and cycled at a current density of 12 mA/cm^2 between 1.0 and 1.6 V, two distinct plateaus were observed. Operation of the cell was terminated during a 12 mA/cm^2 charge at approximately the 50% charge point, and the positive electrode was rapidly removed. Metallographic examination of the electrode revealed only the presence of X phase. The results of these studies are consistent with the Li-Fe-S phase diagram (ANL-78-94, p. 16), and suggest that the discharge reactions are simply

$$FeS \rightarrow X \qquad (6)$$

$$X \rightarrow Li_2S + Fe \qquad (7)$$

b. Cyclic Voltammetry Studies

Cyclic voltammetry studies were carried out to investigate the effects of electrolyte composition and temperature on the reactions of the FeS electrode. The FeS electrodes were cycled at a slow scan rate (0.015-0.020 mV/sec) to ensure high resolution of the current peaks associated with each of the electrode reactions. Electrode reactions which give rise to voltage plateaus in constant-current cycling produce current peaks in a cyclic voltammogram of this type.

A three-electrode cell consisting of an FeS working electrode, an Li-Al counter electrode, and an Li-Al (42 at. % lithium) reference electrode was used for the voltammetry experiments. In these experiments, the LiCl content of the electrolyte and cell operating temperature were varied as follows: 52.8 mol % LiCl at 389, 425, and 451°C; 63.8 mol % LiCl at 435°C; 66.6 mol % LiCl at 433, 440, and 451°C; and 74.4 mol % LiCl at 478 and 495°C. In addition, a voltammetry cell was operated with an electrolyte of

LiF-LiCl-LiBr eutectic at temperatures of 484, 492, and 495°C. The voltage range examined in the voltammetry studies was 0.98 to 1.606 V for all systems except the 66.8 mol % LiCl electrolyte one, which had a voltage range of 1.00 to 1.70 V.

A typical voltammogram obtained for the FeS electrode in the eutectic electrolyte at an operating temperature of 451°C is shown in Fig. VI-1.* As can be seen in this figure, a smooth peak is obtained on discharge and a doublet is obtained on charge. This result and the above cell studies suggest, therefore, that only one species (J phase) is being discharged, and the two species formed during charge lead only to J-phase formation with the cutoff voltages used (<1.6 V). However, because the discharge peak is so large, it is possible that an additional electrochemical reaction is included in what appears to be one peak in the figure.

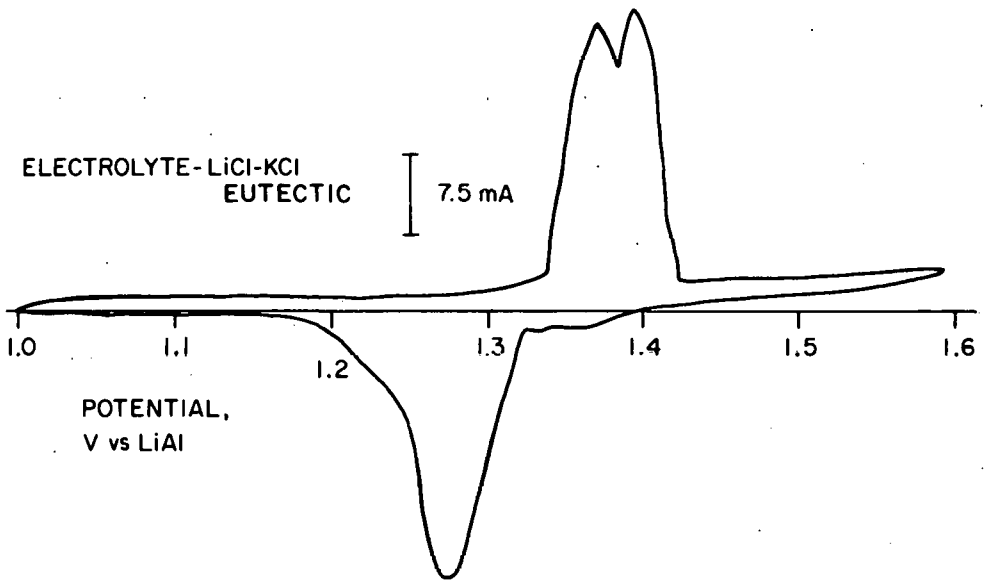

Fig. VI-1. Voltammogram for FeS Electrode in LiCl-KCl Eutectic

In general, the voltammograms of the FeS electrode in LiCl-KCl eutectic indicated that, with increasing temperature, the potentials for the observed reaction peaks decreased and the reaction peaks were completed over a narrower voltage range; this result suggests that the reaction kinetics improve with increasing temperature.

Figure VI-2 shows a voltammogram obtained for the FeS electrode in 66.6 mol % LiCl-KCl electrolyte (operating temperature, 451°C). Voltammograms at a lower scan rate than that used for Fig. VI-2 indicated that at least three species are involved in both the discharge and the charge reactions. Moreover, the voltage difference between the first two charge peaks increased with increasing temperature, thereby indicating that the first species formed is more stable as the temperature is increased. However,

*Charge reactions are shown above the horizontal line and discharge reaction below.

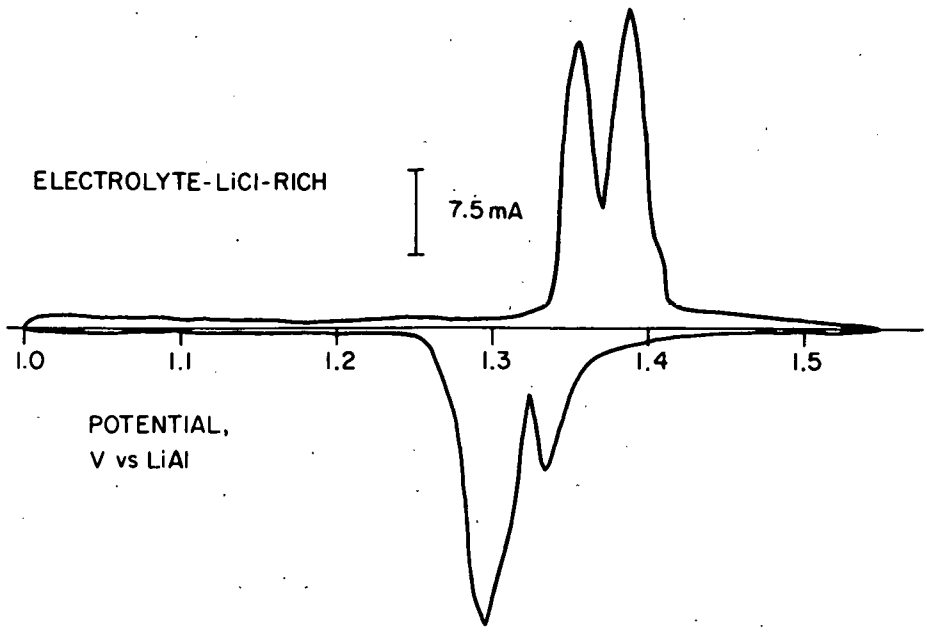

Fig. VI-2. Voltammogram for FeS Electrode in LiCl-rich (66 mol %) Electrolyte

the identity of the first species could not be determined. If the species is assumed to be X phase, then it can be concluded that X is more stable than FeS with increased temperature. The voltammograms also indicated that as the LiCl content of the electrolyte was increased above that of the eutectic at 450°C, the reactions were completed over a narrower voltage limit, indicating better kinetics.

The voltammogram obtained with the LiF-LiCl-LiBr eutectic indicated that three reactions occurred on discharge, which are believed to correspond to

$$FeS \rightarrow X \tag{8}$$

$$FeS \rightarrow Li_2S + Fe \tag{9}$$

$$X \rightarrow Li_2S + Fe \tag{10}$$

Upon continuous cycling, only one discharge-charge peak could be observed, indicating that the reaction was simply

$$FeS \rightleftarrows Li_2S + Fe \tag{11}$$

The latter condition was achieved only after considerable operation time, when some Li_2S from the electrode was probably lost by dissolution into the bulk electrolyte.

c. Thermodynamic Calculations

On the basis of the results from the above cell and cyclic voltammetry studies, previous studies (ANL-78-94, p. 179; ANL-77-17, p. 47), and free energy data available in the literature, we were able to propose a

series of reactions and to calculate the cell potentials for the phase transitions of the Li-Al/FeS cell. These reactions are as follows:

$$2Fe + J + 6Al + 5LiCl \rightleftarrows 26FeS + 6KCl + 6LiAl \quad (12)$$

$$13Li_2FeS_2 + 11Fe + 6KCl + 20Al \rightarrow J + 5LiCl + 20LiAl \quad (13)$$

$$26Li_2S + 24Fe + 6KCl + 46Al \rightleftarrows J + 5LiCl + 46LiAl \quad (14)$$

$$Fe + Li_2FeS_2 + 2Al \rightleftarrows 2FeS + 2LiAl \quad (15)$$

$$Li_2S + 2Al + Fe \rightleftarrows 2LiAl + FeS \quad (16)$$

$$2Li_2S + Fe + 2Al \rightleftarrows Li_2FeS_2 + 2LiAl \quad (17)$$

Of the six proposed reactions, all have been observed to be reversible except for reaction (13). The cell potentials calculated for the above reactions are presented in Fig. VI-3 (the dashed lines are extrapolated data; the reactions do not occur at these temperatures). Additional cell tests to verify the calculated cell potentials for these reactions are being conducted. Preliminary results indicate, however, that precise determination of the emf for these reactions will be extremely difficult.

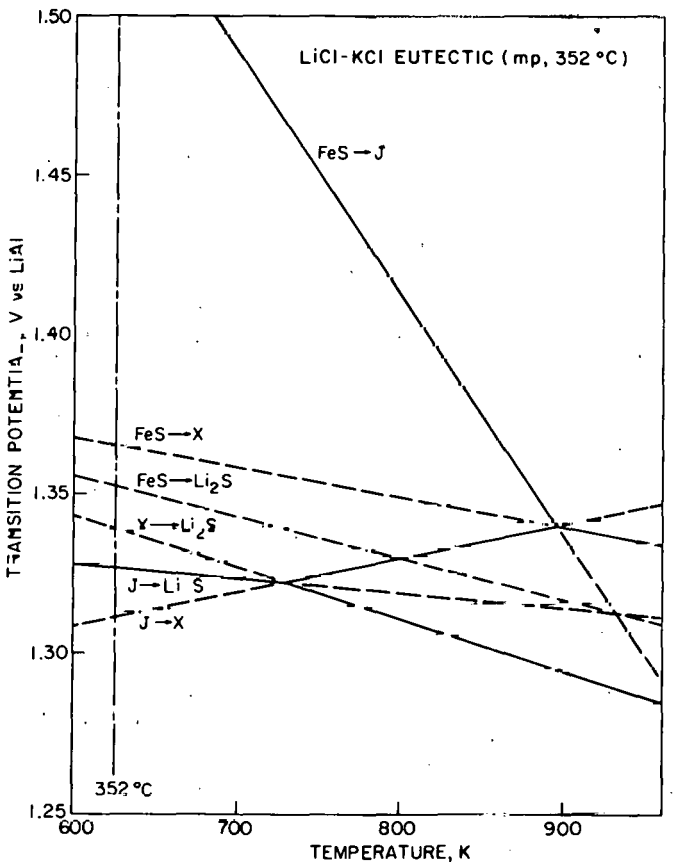

Fig. VI-3. FeS Electrode Reactions and their Calculated Cell Potentials

3. Chemistry of FeS_2 Electrodes
(A. E. Martin, Z. Tomczuk)

During the operation of an Li-Al/FeS_2 cell, the composition of the FeS_2 electrode traverses the Li_2S-FeS-FeS_2 triangle and the Li_2S-Fe-Li_2FeS_2 triangle in the Li-Fe-S phase diagram (see ANL-78-94, p. 167). The phase relations in the latter triangle are simple and have been known for some time. The phase relations in the former triangle are more complicated and have been the subject of considerable study at ANL.

Powders of Li_2S, Li_2FeS_2, FeS and FeS_2 were equilibrated with LiCl-KCl molten salt at 450°C in graphite crucibles in an inert-atmosphere glovebox. The salt, which was present in an amount approximately equal in weight to the powders, served as an inert vehicle to facilitate equilibration. Corrections were made to overall powder compositions for minor weight losses which were assumed to be sulfur. The products were examined metallographically and by X-ray diffraction* to identify the phases that were present. The phase diagram for the Li_2S-FeS-FeS_2 triangle, with appropriate phase designations, is presented in Fig. VI-4; composition fields have been drawn from the data defining two-phase and three-phase fields; the single phases are essentially the same as previously reported. The points C, D, E, and F

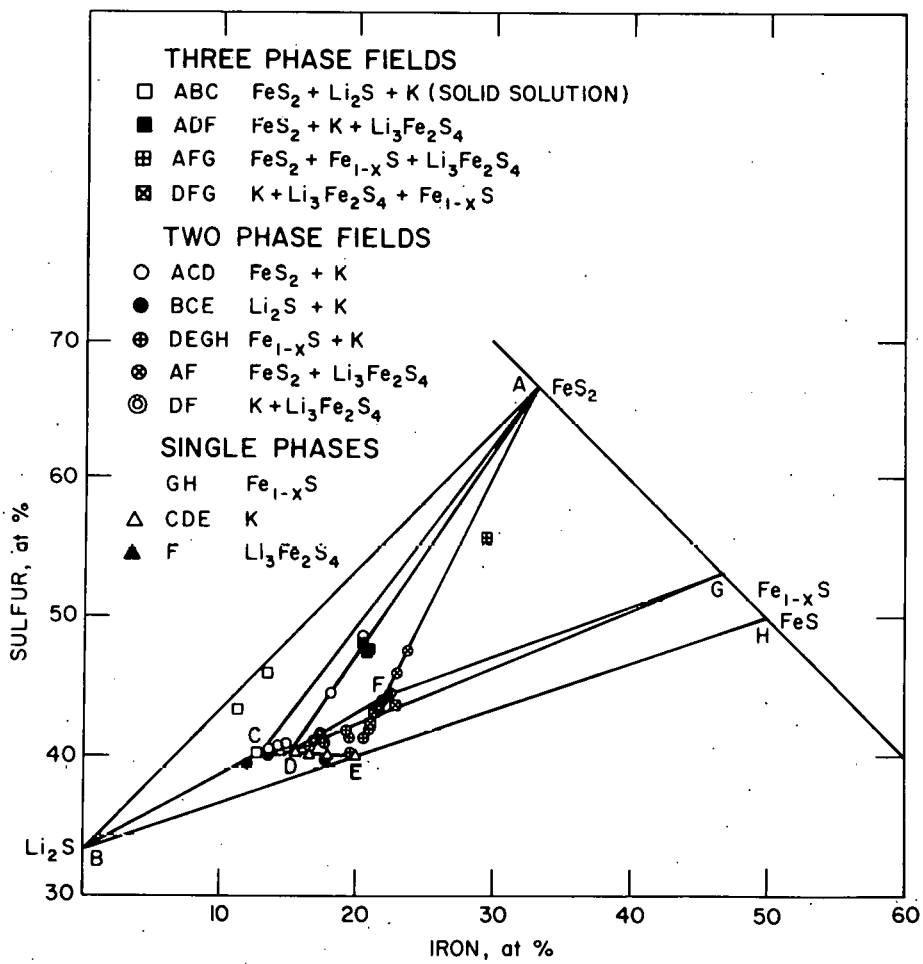

Fig. VI-4. The Li_2S-FeS-FeS_2 Triangle of the Li-Fe-S Phase Diagram

*X-ray diffraction analysis reported in this section was performed by B. S. Tani, Analytical Chemistry Laboratory at ANL.

correspond to Y phase ($Li_7Fe_2S_6$), W phase ($Li_{12}Fe_4S_{11}$), X phase (Li_2FeS_2) and Z phase ($Li_3Fe_2S_4$), respectively. The line CDE appears to correspond to a solid solution; no abrupt change in metallographic appearance occurs in this composition region. Room-temperature X-ray diffraction data on samples in the CDE region were not useful in confirming whether this solid solution exists. It is possible that future X-ray diffraction data obtained with special equipment will resolve this question.

Previous cyclic voltammetry studies (ANL-77-68, p. 48) indicated poor electrochemical reversibility by the FeS_2 electrode in the voltage range of 1.5 to 2.0 V. In the FeS_2 voltammogram, the major discharge peak begins at 1.74 V, which is the potential observed on the upper voltage plateau of Li-Al/FeS_2 cells; however, the major charge peak begins at 1.86 V, which is close to the potential required for oxidation of Li_2S to sulfur. Thus, cell tests were carried out to further investigate the phases formed in the FeS_2 electrode during discharge and charge.

In a continuing effort to understand the electrochemistry of the FeS_2 electrode during charge, we tested three small cells (Z-7, -8, and -9) at selected cutoff voltages. The test cells had 4 A-hr LiAl negative electrodes, 1 A-hr FeS_2 positive electrodes, and an electrolyte of LiCl-KCl eutectic. Each cell was operated for at least ten cycles at a current density of 25-30 mA/cm^2 and cutoff voltages of 2 V (charge) and 1 V (discharge). Cell temperatures varied between 407-419°C. Cell operation was stopped after a normal charge followed by trickle charging (less than 1 mA/cm^2) at a selected voltage for approximately 18 hr. The selected charge voltages for Cells Z-7, -8 and -9 were 1.786, 1.85 and 1.64 V, respectively.

The results of these cell tests and others in this series, summarized in Table VI-2, indicate that, under these cell conditions, it is not possible to form FeS_2 at the potential of 1.76 V, which is the emf observed on the upper voltage plateau in Li-Al/FeS_2 cells. The results also indicate that $Fe_{1-x}S$ is formed in the transition region between Z phase and FeS_2. When FeS_2 does form at a higher potential, it is found to grow on the $Fe_{1-x}S$ material.

Table VI-2. Summary of the LiAl/FeS_2 Cell Results

Cell Designation	Charge Potential *vs* LiAl, V	X-Ray Findings		Metallographic Findings
		Major Phase	Minor Phase	
Z-1	1.53	X	J	X + trace of J
Z-9	1.64	$Fe_{1-x}S$	$\bar{Y}$ and $\bar{X}$ Z possible	$\bar{X}$ + $Fe_{1-x}S$ some Y and Z
Z-2	1.72	Z	-	Z
Z-7	1.786	Z	-	Z + 5% $Fe_{1-x}S$
Z-3	1.82	Z	FeS_2 + $Fe_{1-x}S$	-
Z-8	1.85	FeS_2	$Fe_{1-x}S$	FeS_2 + trace $Fe_{1-x}S$ and Z

Ancillary studies were carried out during the early cycling of Cell Z-7 to investigate the phases formed during low current density discharges and to determine the effect of discharge cutoff voltage on the reversibility of the FeS_2 upper plateau. When Cell Z-7 was discharged at a current density of 2 mA/cm^2, five distinct breaks in the time *vs* voltage curves were observed; thus five reactions were taking place during discharge. The voltages and the reaction assignment for these breaks are given in Table VI-3. The results of these investigations are in agreement with the peaks observed for the cyclic voltammetry studies reported in ANL-78-94, p. 169, but indicate that further work is necessary on the Li-Fe-S phase diagram before the phase relationships in the Li-Fe-S system are completely resolved. The present phase diagram predicts that the transitions on discharge for the FeS_2 electrode are $FeS_2 \rightarrow Z \rightarrow W + Fe_{1-x}S \rightarrow Li_2FeS_2 \rightarrow Li_2S + Fe$.

When Cell Z-7 was charged from the fully uncharged condition, the normal irreversible upper plateau at ∿1.86 V was observed. However, when the cell was discharged to a 1.60 V cutoff, two charge plateaus were observed: one occurring at the reversible emf (1.74 V) and the other occurring at the irreversible emf normally observed during charging of $LiAl/FeS_2$ cells. Surprisingly, the lengths of the two plateaus were equal. An explanation for the above results is not available, but one possibility is that there may be two structural forms of the Z phase. The results of these studies are in general agreement with earlier cyclic voltammetry and cell tests (ANL-78-94, p. 175) in which similar observations were reported.

Table VI-3. Voltages Observed During Discharge of Cell Z-7

Reaction Assignment	Emf *vs* LiAl
$FeS_2 \rightarrow Li_3Fe_2S_4$	1.74
$Li_3Fe_2S_4 \rightarrow W + Fe_{1-x}S$	1.64
$W + Fe_{1-x}S \rightarrow T$[a]	1.56[b]
T[a] $\rightarrow Li_2FeS_2$	1.54 to 1.32
$Li_2FeS_2 \rightarrow Fe + Li_2S$	1.32

[a]The product is designated as T because the composition of the reaction product is not known.

[b]The total observed capacity for this reaction was ∿2% of the total.

4. Physical Properties of Electrode Materials
(A. K. Fischer)

Investigations of the physical properties of the electrode materials are being conducted to supply the information needed for cell and battery development and optimization. Mathematical modeling of the cell is especially dependent on such data. Therefore, electronic conductivity and entropy data were gathered for the different electrode

materials. Conductivity and entropy values of the different materials were obtained from the literature. Entropy values not available were calculated by established estimation procedures.

a. Electronic Conductivity

Pridmore *et al.*[11] have reported that the n-type conductivity at room temperature of naturally occurring pyrite covers five orders of magnitude, from 0.0037 to 530/Ω-cm. The published distribution curve of conductivity *vs* numbers of samples shows a peak at about 10/Ω-cm. The variation arises from deviations from stoichiometry and from impurity content. Between room temperature and 450°C, the conductivity of FeS_2 appears to rise somewhat less than one order of magnitude;[12] therefore, the range of conductivity of FeS_2 at cell operating temperature is about 0.04 to 5000/Ω-cm, with the peak of the distribution curve corresponding to about 100/Ω-cm. However, decomposition of FeS_2 may be a problem above 280°C according to some authors.[13]

For FeS (or $Fe_{1-x}S$), the conduction can be n-type with excess iron or p-type with excess sulfur, and the magnitude of the conductivity is variable. In molten FeS, the conductivity values range from 400/Ω-cm for stoichiometric FeS to 4850/Ω-cm for iron-rich material.[14] For solid non-stoichiometric $Fe_{1-x}S$, the conductivity below 150°C is markedly anisotropic in single crystals. However, the curves for the conductivities at 450°C parallel and perpendicular to the C axis appear to be merging and show about 1100 and 2700/Ω-cm, respectively.[15] For a polycrystalline sample, some intermediate value might be expected. Pyrrhotite (Fe_7S_8) has been reported to have a conductivity of 62 to 5000/Ω-cm.[16]

The existing data for the conductivities of the iron sulfides appear to support the assumption that the ratio of their electronic conductivities to that of the electrolyte[17] is large. Such an assumption is involved in some of the modeling of the cell that is being done by Newman and Pollard.[8]

It would probably be most practical, if any conductivity measurements on positive-electrode species are made, to measure the conductivity of X, J, and Z phases, rather than that of FeS and FeS_2, because these phases are involved over a large part of the cell cycle.

b. Entropy and Entropic Heat

Entropic heat effects in an operating cell have a strong bearing on the thermal management of the system (how much insulation is needed, how much cooling, if any, must be provided, *etc.*). Some of the data needed to calculate the thermal effects are in the literature. Important values that are not in the literature are the absolute entropies of X, J and Z phases. Estimates of the entropies (S) of these species were made by the Latimer method.[18] In the case of LiAl, the value was derived from the data of Yao *et al.*[19] Table VI-4 lists the entropies for species of interest.

Good agreement was found between reported observations and calculated (from the entropies) values of the slopes of emf *vs* temperature curves for several upper plateau and lower plateau processes. In the case of

Table VI-4. Entropies of Species Involved in Lithium-Iron Sulfide Cells

Substance	S_{298}, cal/mol deg	S_{723}, cal/mol deg	Source
Fe(s)	6.529	12.678	Ref. 20[a]
Al(s)	6.769	12.392	Ref. 20[a]
Li(ℓ)	8.113	14.504	Ref. 20[a]
Li(s)	6.954	12.992	Ref. 20[a]
S(ℓ)	8.444	15.838	Ref. 20[a]
S(s)	7.631	13.787	Ref. 20[a]
LiCl(s)	14.173	25.324	Ref. 20[a]
KCl(s)	19.733	31.232	Ref. 20[a]
Li_2FeS_2(s)	31.6	62.1	Estimated[b]
Li_2S(s)	14	32	Estimated[b]
FeS_2(s)	12.65	31.12	Ref. 21[a]
FeS(s)	-	32.2	Ref. 22
$Li_3Fe_2S_4$(s)	59.0	114.0	Estimated[b]
$LiK_6Fe_{24}S_{26}Cl$(s)	466.0	824.9	Estimated[b]
$KFeS_2$(s)	32.8	58.0	Estimated[b]
$FeCl_2$(s)	19.8	35.4	Estimated[b]
LiAl(s)	-	21.8	Refs. 19, 20

[a]Interpolated for 723 K.

[b]Estimates for S_{298} for the solid compounds were made by the Latimer method.[18] This step was regarded as accounting for the entropy effects associated with compound formation from the elements. Values of S_{723} were obtained by adding to S_{298} the entropy changes for the constituent solid elements between 298 K and 723 K as given by the JANAF tables.[20]

the upper-plateau reaction in its simplest form,

$$2\ LiAl + FeS_2 \rightarrow FeS + Li_2S + 2\ Al \qquad (18)$$

the calculated value of dE/dT is 0.31 mV/deg. However, since the discharge of FeS_2 is known to proceed through Z phase, another reaction to describe the upper-plateau process is

$$2\ LiAl + \frac{4}{3}\ FeS_2 \rightarrow \frac{2}{3}\ Li_3Fe_2S_4 + 2\ Al \qquad (19)$$

for which the calculated value of dE/dT is 0.34 mV/deg. The experimental value for this upper-plateau is 0.33 mV/deg (ANL-77-17, p. 47*). Thus, the experimental and calculated values agree better for reaction (19) than (18). For the lower plateau, a simple representation of the reaction is

$$2\ LiAl + FeS \rightarrow Fe + Li_2S + 2\ Al \qquad (20)$$

for which the calculated dE/dT is -0.14 mV/deg. However, since X phase is known to be involved in this process

$$2\ LiAl + 2\ FeS \rightarrow Li_2FeS_2 + Fe \qquad (21)$$

The calculated dE/dT for reaction (21) is -0.18 mV/deg, which is in good agreement with the experimental value of -0.16 mV/deg (ANL-77-17, p. 47). In addition, the calculated value of the entropic heating of a cell at 450°C is 0.13 W/A for reaction (21) and 0.10 W/A for reaction (20). These values agree fairly well with a value of 0.104 W/A observed in an experiment with a cell designed with special instrumentation for the specific purpose of measuring heat balances.[23]

B. Separator Development
(J. E. Battles)

The electrode separator is a key component of the cell, and must meet several requirements, including compatibility with the electrode materials and electrolyte, adequate mechanical strength, acceptable cost, suitable porosity and thickness, and lack of electronic conductivity. Because the BN cloth separators† currently used are expensive, efforts have been directed toward the development of BN felt, ceramic powder, and porous, sintered ceramic separators.

1. Characterization of BN Felt Separators
(R. B. Swaroop)

A shipment of BN felt sheets (2-mm thick) was received from Carborundum Co. The quality of these felts was then assessed before and after stabilization, which is a high-temperature (1750°C) treatment in nitrogen to decrease the residual B_2O_3 content. The thickness, basis weight, burst strength, and handling for cell assembly of sixteen randomly selected felts were measured both before and after stabilization. Table VI-5 shows these measurements for ten felt separators. As-received felts had thicknesses of 1.90 to 2.35 mm, an average basis weight of 34.5 mg/cm^2, and an average burst strength of 4.5 kPa/mm. As expected, the basis weight of stabilized felts decreased to an average value of 29.8 mg/cm^2 as a result of oxygen loss; however, the low burst strength and handling difficulties of stabilized felt were unexpected. This property decline is believed to be due to weaker bonds as a result of the long exposure of felts (~6 months) to room environment

*A value of 0.35 mV/deg was initially determined for the upper plateau reaction, but this value has been subsequently refined to 0.33 mV/deg.

†Boron nitride cloth separators have been successfully used in cells of approximately 2.5 years life.

Table VI-5. Characterization of BN Felts (Batch IV) Before and After Stabilization

Felt No. D244-	Thickness, mm		Basis Wt, mg/cm^2		Burst Strength, kPa/mm		Cell-Assembly Handling[a]	
	Before	After	Before	After	Before	After	Before	After
29B2(T)	2.01	2.03	36.91	31.20	3.48	1.67	E	F
31B2(M)	2.05	2.10	36.05	30.62	3.41	1.47	E	D
32B1(T)	2.36	2.38	34.64	29.45	3.00	1.45	E	F
30B1(B)	1.88	2.08	35.75	28.97	4.20	1.82	E	F
40-B	1.96	1.98	32.80	28.48	5.70	2.04	E	D
39B2(T)	2.26	2.25	33.04	28.87	4.51	1.84	E	D
37B2(M)	2.31	2.30	33.43	30.42	3.85	2.27	E	E
37B1(T)	2.18	2.18	33.57	30.91	4.36	2.29	E	E
21(T)	1.96	2.15	34.01	-	7.65	1.60	E	D
38B1(M)	2.36	2.41	34.20	29.40	4.54	2.00	E	F
Average:	2.13	2.20	34.44	29.81	4.47	1.84	-	-

[a]The symbols used for this separator property are as follows: E, excellent; F, fair; and D, difficult.

before stabilization. Therefore, BN felts should be protected from the ambient environment until they have been stabilized. An additional shipment of 200 sheets of BN felt was also received during this period; these felts are presently being characterized.

Stress-strain measurements were made on BN fabric and BN felt to estimate the thickness of the separator during cell operation. As indicated in Fig. VI-5, the compression of the fabric resulting from an applied pressure is not the same as that of felt. At stresses of 210-245 kPa (30-35 psi), the pressure at which FeS material has been found to flow significantly (ANL-78-45, p. 43), the compression of the felt was approximately 40% and 60% of the original thickness, respectively. Furthermore, felts at stresses above ∿175 kPa (∿25 psi) have been observed to deform plastically (permanently). Similar measurements will be continued on BN fabric and felt at higher stress levels in order to understand their deformation behavior.

Two separator materials, MgO powder and BN felt, were evaluated in small-scale, prismatic (7.6 x 12.7 cm) cells; the design of these cells was discussed in ANL-77-75, p. 34. The MgO powder separators were cast as 1.8-mm thick plates of the desired size from an equal mixture of MgO powder (-60 + 120 mesh) and eutectic salt. This MgO-salt mixture was cast in a steel mold by raising the mold temperature to above the melting point of the electrolyte (352°C) and then cooling. The cast MgO powder separator

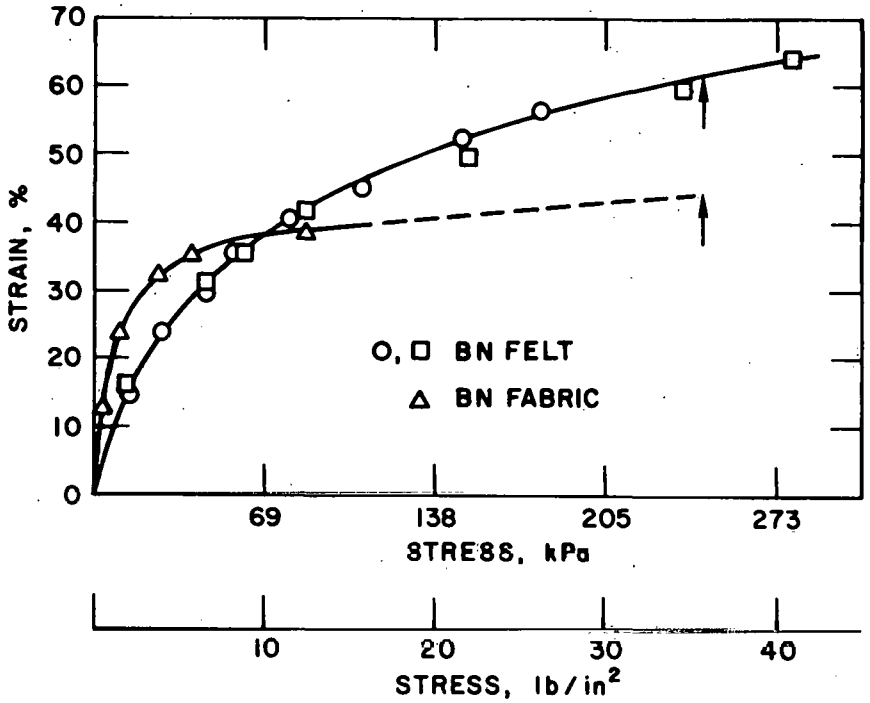

Fig. VI-5. Stress-Strain Measurements on BN Fabric and Felt

offers an inexpensive fabrication technique* for preparing easily handled separators. Cell SC-31 was assembled using the pre-cast MgO powder separators and was operated for 122 cycles (99 days). This cell achieved excellent performance in comparison to previously operated cells with MgO powder separators. A coulombic efficiency of greater than 98% was maintained for the first 90 cycles. Figure VI-6 shows the active-material utilization of cell SC-31 along with two other cells, one with a vibratory-loaded MgO powder separator (SC-21) and the other with a BN felt separator (SC-27); the utilization of SC-31 was higher than that of cell SC-21 (MgO powder) but lower than that of cell SC-27 (BN felt). The data in Fig. VI-6 also indicate that good performance can be obtained at low current densities (<60 mA/cm^2) by cells with MgO powder or plate separators. Post-test examination of cell SC-31 revealed that the separator plate had been reduced in thickness by 22% (from 1.8 to 1.4 mm) and in porosity by 20% (from 50 to 40%).

Another separator-test cell (SC-30) was assembled with a 3.2 mm-thick felt separator that had been pre-wetted with ∿14 mg/cm^2 of $LiAlCl_4$ powder.† The wetting agent facilitated separator wetting by the electrolyte during start-up and did not appear to have a detrimental effect on cell performance. Two other separator-test cells (SC-33 and SC-34) were assembled with BN felt separators with unstabilized BN bonds. One cell is still

*Patent request letter by F. Mrazek and J. Battles to H. Glenn, Jan. 4, 1979.

†This wetting agent is discussed in ANL-78-94, p. 158.

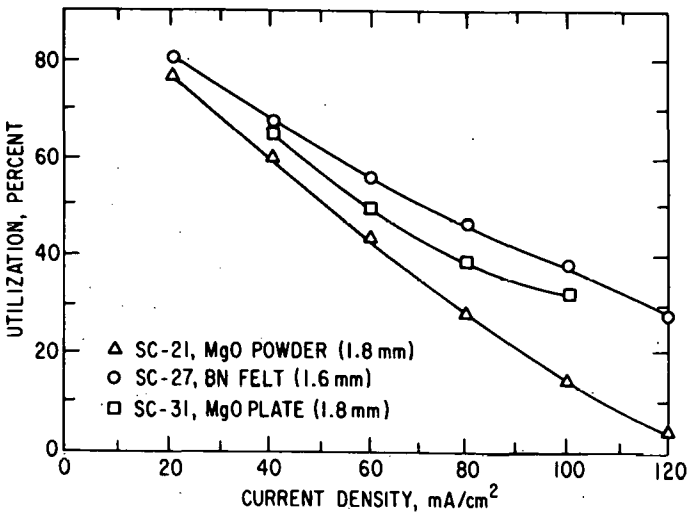

Fig. VI-6. Utilization Performance of Separator-Test Cells SC-21, SC-27 and SC-31

showing good performance characteristics after 120 cycles (1800 hr). The good performance shown by this cell indicates that BN felts with unstabilized BN bonds are suitable for testing in developmental cells.

2. Porous, Sintered Ceramic Separators
(G. Bandyopadhyay, J. T. Dusek, and T. M. Galvin)*

Procedures are being developed to fabricate porous, sintered ceramic separators, which are then being evaluated by in-cell tests. Four cells were fabricated and tested using porous, sintered ceramic separators: Cells MS-1 and MS-2 (Y_2O_3) and Cells MS-3 and MS-4 (MgO). The fabrication techniques for these separators were reported in ANL-78-94, p. 150. The method of fabrication and the physical characteristics of the separators used for in-cell testing are given in Table VI-6; Figure VI-7 presents pore-size information on sintered plates of Y_2O_3 (60.7% porosity) and one of MgO (45% porosity). The active-material utilization as a function of discharge current density of these separator cells is shown in Fig. VI-8. For comparison, this figure includes the performance data for SC-21 (MgO powder separators, ∿1.8-mm thick) and SC-25 (BN felt, ∿1.25-mm thick). Of the six cells shown in this figure, the BN-felt cell exhibited the best active-material utilization at current densities of 20 to 120 mA/cm^2. This is probably due to the higher pososity (and therefore lower internal resistance to ionic flow) of the felt separators. Of the four MS-series cells, MS-1 and -2 had higher utilizations than those of MS-3 and -4. This result may also be related to the higher porosity of sintered Y_2O_3 separators as compared to that in MgO separators.

*Materials Science Division, ANL.

Table VI-6. Processing Conditions and Physical Characteristics of the Sintered Separators Used for In-Cell Testing

Cell No.	Theor. Capacity, A-hr	Separator Plate No.	Composition	Calcination Temp., °C	Calcination Time, hr	Sintering Temp., °C	Sintering Time, hr	Porosity, %	Average Pore Diameter,[a] μm	Cumulative Pore Volume,[a] cm^3/g	Thickness, mm
MS-1	35.7	115	Crushed Y_2O_3-nitric acid plaster and 12% binder	1250	~8.5	1500	No Hold	50.6	-	-	2.47
		125	Crushed Y_2O_3-nitric acid plaster and no binder	1250	~8.5	1440	No Hold	51.3	0.76	0.1364	2.13
MS-2	50.0	179	Calcined Y_2O_3 foam mixed with 10% as-received Y_2O_3	1550	13	1450	6	50.8	0.50	0.2997	1.50
		180	Calcined Y_2O_3 foam mixed with 10% as-received Y_2O_3	1550	13	1450	6	60.1	0.50	0.2997	1.47
MS-3	35.7	201	Calcined MgO mixed with ~5% as-received MgO	1450	~2.8	1400	5	42.2	-	-	1.93
		202	Calcined MgO mixed with ~5% as-received MgO	1450	~2.8	1400	5	38.5	-	-	1.88
MS-4	50.0	217	Calcined MgO mixed with 6.7% as-received MgO	1450	4	1420	~3.3	33.8	-	-	1.78
		218	Calcined MgO mixed with 6.7% as-received MgO	1450	4	1420	~3.3	44.2	0.74	0.291	1.74

[a] These values were determined from plates that are similar to the separators which were actually used in-cell.

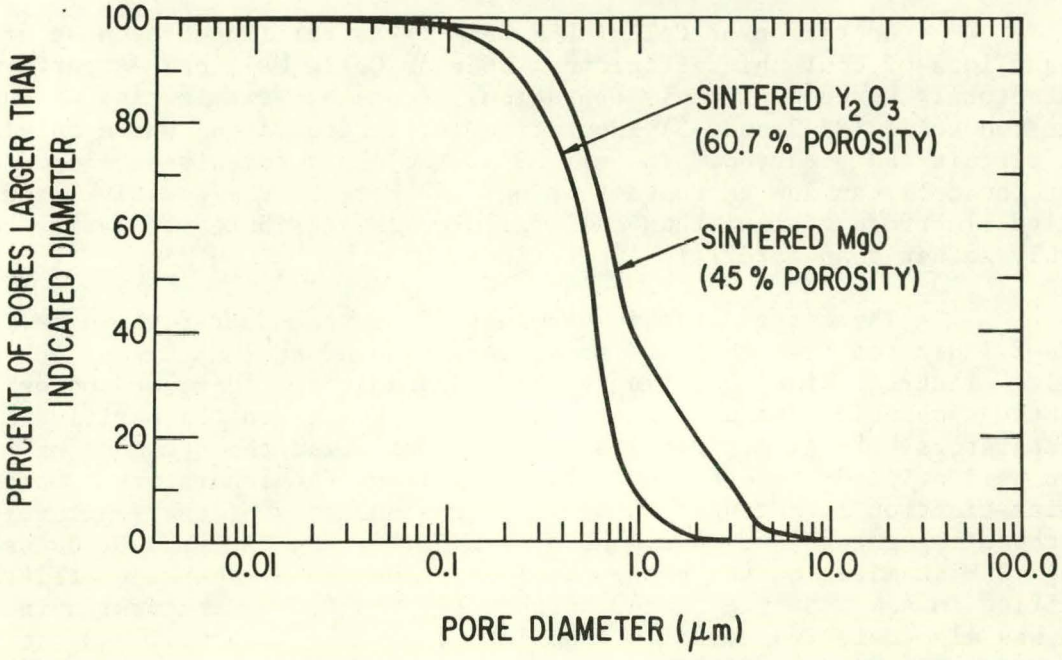

Fig. VI-7. Pore Sizes and Pore-Size Distribution in Sintered Separator Plates

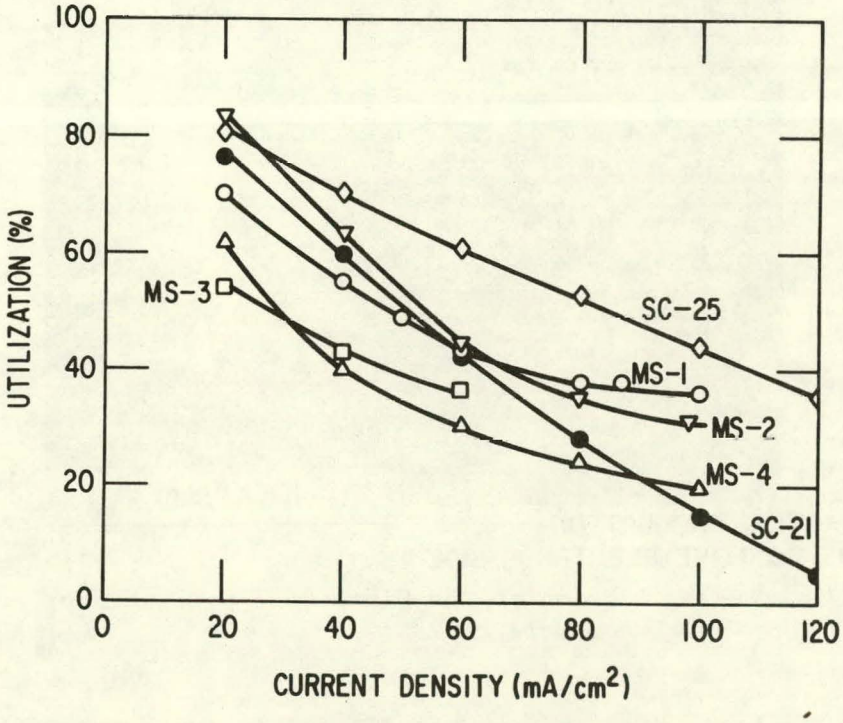

Fig. VI-8. Active-Material Utilization of Six Separator-Test Cells

Operation of Cells MS-2 and -3 was terminated because of a significant loss of coulombic efficiency; whereas Cells MS-1 and -4 performed satisfactorily throughout their operation. Post-test examination of the former two cells (MS-2 and -3) identified the general areas where an electrical short circuit had occurred. In Cell MS-3, the short circuit developed at the top of the cell can due to contact being made between the positive- and negative-electrode frames; thus cell failure was attributed to faulty cell assembly rather than materials limitations.

The metallographic examination of the separators in Cells MS-1 and MS-2 indicated that the Y_2O_3 separators reacted to some extent on the positive electrode side (see Fig. VI-9). In addition, increased porosity, indicating possible damage of the separator, appeared on the positive side of the separators. X-ray diffraction analysis indicated the presence of Y_2O_2S and an unidentified phase on the positive side of the separators. Using scanning electron micrographs (SEM) and X-ray analyses of the fracture surfaces from these separators, we were unable to identify the reaction products. Through SEM examination the presence of small hexagonal-shaped platelets was identified in some isolated areas of the Y_2O_3 and MgO separators. Since Y_2O_2S was also detected in cells (ANL-78-94, p. 161) that used Y_2O_3 felt or Y_2O_3 powder separators, yttria is considered an unsatisfactory material for long-term performance of the Li-Al/iron sulfide cells.

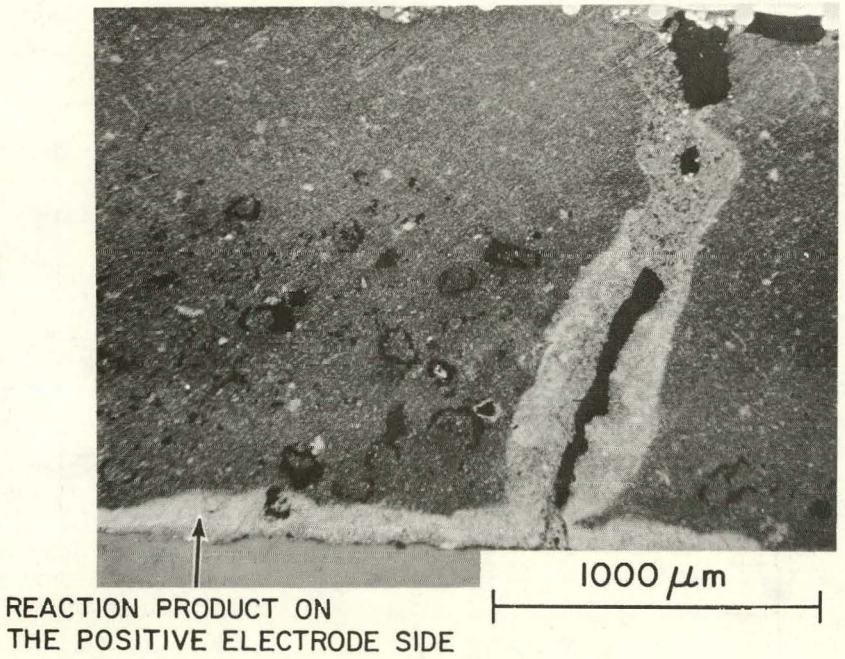

Fig. VI-9. Section of the Sintered Y_2O_3 Separator from Cell MS-2

In Cells MS-3 and -4, metallographic and X-ray diffraction examinations showed no evidence of chemical reaction between the active materials and the sintered MgO separators. These results indicate that sintered MgO separators are probably suitable for application in Li-Al/FeS battery systems. The low utilization in these cells was attributed to the low porosity (~40%) of their separator. However, one should be able to fabricate sintered MgO separators with porosities up to ~60% (as was obtained for Y_2O_3

plates) by following the processing technique described in ANL-78-94, p. 150. This porosity is still considerably lower than that in BN felts (~90% porosity); MgO separators with this porosity will be heavier than BN felt of the same thickness (densities of MgO and BN are 3.58 and 2.20 g/cm^3, respectively). Despite these drawbacks, sintered MgO separators should be considered as promising candidates for use in Li-Al/FeS battery systems due to their low-cost potential.

C. Current Collector Development
(J. E. Battles)

The corrosiveness of the active materials in the positive electrodes (FeS and FeS_2) and the molten electrolyte places severe restrictions on the materials that can be used for current collectors. Iron has been found to be a satisfactory current-collector material in Li-Al electrodes, and can be used for a limited period (<1 yr) in FeS electrodes; nickel, iron-based alloys, and several other materials are under investigation for longer-term use in FeS electrodes. The only current-collector material that has been used successfully in FeS_2 electrodes is molybdenum, which is expensive and difficult to fabricate; alternatives such as protective coatings for inexpensive metals are under investigation.

1. Current Collector Materials for FeS Electrodes
(J. A. Smaga)

The development of experimental alloys has been one phase of the overall effort to obtain corrosion resistant and economically priced replacements for the low-carbon steel current collectors presently used in FeS electrodes. Three of these experimental alloys have been fabricated into sheet form by outside vendors. These iron-base alloys--designated ANL-5-0, ANL-10-20, and ANL-15-30--contain nominal additions of 4.5 wt % Mo; 10 wt % Mo-20 wt % Ni; and 15 wt % Mo-30 wt % Ni, respectively. Some of the key physical properties of these alloys are listed in Table VI-7.

Table VI-7. Physical Properties of the ANL Alloys

Physical Properties	ANL-5-0	ANL-10-20	ANL-15-30
Corrosion Rate, μm/yr	11	+9[a]	+18[a]
Oxidation Potential, V *vs* Li	2.25	2.47	2.42
Resistivity, 10^{-6} Ω-cm	25.4	78.0	92.4
Hardness,[b] R 15 T	53	84	77
Density, g/cm^3	8.08	8.89	~9.0

[a]The positive sign indicates the deposition of a thin iron layer as the predominant reaction.

[b]The Rockwell 15 T surface hardness scale.

Alloy ANL-5-0 is a binary alloy near the solid-solution limit of molybdenum in iron. X-ray diffraction analysis determined that this alloy has a body-centered-cubic crystal structure with a lattice parameter of 2.875 Å. Samples of this alloy in both the as-received and annealed form experienced minimal corrosion attack in the FeS-salt environment. The average corrosion rate for these samples was 11 μm/yr, which is 40 to 50 times lower than the corrosion rates found for iron or low carbon steel in similar tests. In the annealed condition the ambient resistivity of this alloy is twice that of fully annealed low carbon steel. Voltammetry measurements made on this alloy in LiCl-KCl eutectic at 425°C indicate that its oxidation potential (onset of rapid anodic dissolution) is 2.25 V *vs* Li, which is 0.1 V higher than the theoretical value for iron.

For alloy ANL-10-20, the addition of nickel combined with proper heat treatment allows an increase in the molybdenum concentration without producing a two-phase alloy. X-ray diffraction analysis determined that this alloy has a face-centered-cubic structure with a lattice parameter of 3.56 Å. This alloy showed a slight weight gain in static corrosion tests due to the deposition of iron from the FeS-salt environment. The higher alloy content of ANL-10-20 increases the oxidation potential by an additional 0.22 V and results in significant solid-solution hardenability, as measured on the Rockwell 15 T surface hardness scale. The increased molybdenum and nickel concentration also increases the resistivity to 78.0 μΩ-cm, which is similar to that of Type 316 stainless steel.

The above two alloys were fabricated by the Cabot Corp., which reported no fabrication difficulties. Alloy ANL-15-30 was obtained at an earlier date from AMAX Specialty Metals Corp. This vendor experienced great difficulty in working the as-cast ingot into final sheet form. Metallography and SEM analysis* of intermediate rolling samples revealed that the ingot was never homogeneous. A Mo-rich (>40 wt %) second phase caused the fabrication difficulties and was never fully eliminated by the successive hot-rolling steps. A series of in-house solution anneals indicated that the alloy could be homogenized, but the required time at temperature would produce a mechanically weakened alloy due to excessive grain growth. As a result, the properties listed in Table VI-7 are not optimum values. In static corrosion tests, ANL-15-30 developed layers of iron deposits. The somewhat lower oxidation potential and hardness values of ANL-15-30, in comparison to ANL-10-20, suggest that its molybdenum concentration in the primary phase is slightly lower. The higher resistivity of ANL-15-30 is expected on the basis of both the higher total alloy content and the presence of a second phase.

All three of these alloys show the necessary corrosion resistance for application in FeS electrodes. At this time, however, ANL-5-0 appears to offer the best combination of corrosion resistance, formability, and low cost with the smallest penalty in increased electrical resistivity and weight. Future alloy development work will center on further refinements of the basic ANL-5-0 alloy, and present expectations are that this alloy will be used for current collectors in the Mark II battery.

---

*W. Shinn, Chemistry of Irradiated Fuels Group at ANL.

2. In-Cell Testing of Current Collector Materials
(J. A. Smaga)

Static corrosion tests (ANL-77-75, p. 35; ANL-78-94, p. 139) have been used to identify candidate materials which may be suitable for application as positive-electrode current collectors and frames. Subsequently, in-cell corrosion tests were conducted to evaluate the candidate materials identified by the static corrosion tests. Small-scale, prismatic cells (7.6 x 12.7 cm) were used in this study.*

The results of the cell tests that have been completed thus far are summarized in Table VI-8. Commercially pure nickel was evaluated in a series of six Li-Al/FeS cells (3C-1, 2, 4, 5, 8 and 9). Cells 3C-1, -2, -4, and -5 were assembled in the semi-charged state; three of the cells had a 1.7 V charge cutoff voltage and one (Cell 3C-5) had a 1.6 V charge cutoff. The nickel components from all four of these cells exhibited the same type of corrosion reaction, namely, minor surface attack (<6.4 μm) except in localized areas (10-30%) which underwent severe intergranular attack that penetrated more laterally than perpendicularly to the surface; the mechanical strength was also severely impaired by this attack. The mean corrosion rates for Cell 3C-5 (13 μm/yr for the collector and 21 μm/yr for the frames) were substantially lower than the 100 to 300 μm/yr range of rates obtained for the other three cells. This low corrosion rate for 3C-5 was attributed to a declining reaction rate with cycling, and possibly to a poor utilization of active material. The latter performance characteristic of 3C-5 resulted from the use of a lower charge cutoff potential and the attainment of a higher internal resistance than those of the other two cells.

Cells 3C-8 and 3C-9, both of which had nickel current collectors and frames, were assembled in the fully charged condition and were operated with a 1.65 V cutoff. Cell 3C-8 had 20 wt % Cu_2S added to the positive electrode and LiCl-KCl eutectic electrolyte; Cell 3C-9 used 54 wt % LiCl-46 wt % KCl electrolyte and no positive-electrode additives. Examination of these cells revealed iron deposition onto a virtually unattacked nickel substrate and no evidence of intergranular attack. X-ray diffraction analysis confirmed that the deposit was α-Fe and indicated that some interdiffusion had occurred between the iron layer and nickel substrate. Microscopic measurements gave average deposit thicknesses of 5 μm for 3C-8 and 7 μm for 3C-9, which correspond to corrosion rates of +20 μm/yr and +30 μm/yr, respectively. Iron was also deposited on the nickel screens used as particle retainers for these cells. The effect of the iron deposition on the mechanical properties of these nickel components appears to be minimal.

The detrimental intergranular attack on the nickel current collectors was observed only in cells assembled in the semi-charged state, regardless of whether the charge cutoff voltage was 1.6 or 1.7 V. This corrosion mechanism was not observed in the two cells assembled fully charged and using a 1.65-V cutoff voltage. Thus, the charge state of the initial positive electrode mix, not the charge cutoff potential, was responsible for the severe localized attack. Furthermore, it is concluded that nickel has the necessary corrosion resistance for long life in FeS electrodes of cells assembled in the charged state.

*See ANL-77-75, p. 35, for the general design of this cell.

Corrosion testing was also conducted on two Li-Al/FeS experimental cells, 3C-10 and -11, which had components constructed of ANL-5-0 (Fe-4.5 wt % Mo) and ANL-10-20 (Fe-10 wt % Mo-20 wt % Ni) respectively. Both of these cells were assembled charged, operated for one month, and then examined. The corrosion rates for the iron-base alloys are presented in Table VI-8.

Table VI-8. Performance Data and Corrosion Results for Test Components of 3C Series Cells

Description		Lifetime	Mean Corrosion Rates,[a] μm/yr		Comments
Cell No.	Test Material	Days/Cycles	Collector	Frame	
3C-1	Nickel	76/184	110	110	Minimal attack over most exposed surface. Severe lateral intergranular attack over 10 to 30% of the component surface.
3C-2	Nickel	31/43	170	240	
3C-4	Nickel	35/50	240	280	
3C-5	Nickel	153/281	13	21	
3C-8	Nickel	91/169	+20	+20	5-μm Fe deposition layer.
3C-9	Nickel	91/132	+30	+30	7-μm Fe deposition layer.
3C-10	ANL-5-0	31/56	<15	<15	No measurable attack.
3-C-11	ANL-10-20	31/63	+15	+15	1.5-μm Fe deposition layer.
3C-3	Hastelloy B	31/38	610	950	General corrosion attack, the rate of which was lowest under the conducting rod and highest at the lower corners.
3C-6	Hastelloy B	31/97	690	1000	
3C-7	Hastelloy B	74/102	300	330	

[a]Values preceded by "+" represent the rate of formation for an adherent reactor layer.

For the ANL-5-0 alloy components, micrometer measurements with a 0.1 mil precision indicated no change in material thickness. This corresponds to a maximum possible corrosion rate of 15 μm/yr. Microscopic examination also showed little evidence of corrosive attack. A 200-mesh stainless steel screen was used in conjunction with the iron-base alloy frames, and no evidence of a detrimental galvanic reaction between the two metals was noted. For the ANL-10-20 alloy components, micrometer measurements indicated a slight increase in thickness. Microscopic examination showed evidence of iron deposits which coated about 50% of the examined area and had a maximum thickness of 2.5 μm, corresponding to an average deposition rate of 15 μm/yr. The observed deposition effect was comparable to that discussed for Cells 3C-8 and -9 and was expected on the basis of static corrosion tests. The iron deposition layer should not impair the mechanical or electrical properties of these components. The low reaction rates for both of these iron-base alloys is highly encouraging and give a preliminary indication that both materials will achieve a long life in FeS electrodes. Four additional cells, two for each alloy, have been placed in operation to complete the evaluation of these alloys.

Cells 3C-3, 3C-6, and 3C-7 were operated to test Hastelloy B for application in FeS_2 electrodes. For all three cells, the exposed surfaces of the collector and the inner frame exhibited the same uniform surface attack. The current collector showed a gradient in the rate of reaction, with the area immediately below the conductor bar showing the least amount of corrosive attack and the lower corners showing the most severe attack. These three cells had very high corrosion rates for their Hastelloy B components, with the components of Cell 3C-7 having the lowest corrosion rates. The calculated corrosion rates for 3C-7 ranged between 120 and 630 μm/yr; the mean values were 300 μm/yr for the collector and 330 μm/yr for the frame. It was inferred from the data in Table VI-8 that the rate of attack decreased sharply with increased length of operation. This reduction is probably attributable to a decrease in the effective sulfur-to-metal ratio in the positive electrode due to the high initial rate of attack. The lower rates for the components of Cell 3C-7 are still unacceptably high, and Hastelloy B must be considered unacceptable for long-term use in FeS_2 electrodes.

3. Ceramics for Positive-Electrode Current Collectors (G. Bandyopadhyay, T. M. Galvin, and J. T. Dusek)*

Electrically conductive ceramic coatings on inexpensive metallic substrates are being investigated as substitutes for the high-cost molybdenum current collectors now being used in the positive electrodes of FeS_2 cells. The requirements of such a current collector system include (1) sufficient electronic conductivity to provide current collection efficiency, (2) corrosion resistance in the FeS_2 and molten LiCl-KCl environment at 450°C, (3) resistance to damage under mechanical and thermal stresses that are generated in the cell environment, and (4) lower cost than molybdenum.

Preliminary investigations (ANL-78-94, p. 144) indicated that a number of conductive ceramics, such as TiN, TiC, TiB_2, iron boride, and niobium carbide, should be thermodynamically stable in the FeS_2 positive electrode. Preliminary static corrosion tests were performed on TiN, TiB_2, and iron boride coatings on AISI 1008 steel substrates in an FeS_2-salt environment at 500°C, and only the TiN coating showed adequate stability. Local defects in coatings rather than the coating compositions were thought to be responsible for the deterioration of the specimens. Further static corrosion tests were thus performed on (1) hot-pressed TiN, TiC, and TiB_2 specimens, (2) specimens coated with the candidate materials by chemical vapor deposition (CVD) or by the *rf* sputtering technique, and (3) duplex-coated structures in which the defects in the top coating might be protected by the coating underneath.

The results from these static corrosion tests are summarized in Table VI-9. As can be seen in this table, hot-pressed TiN and TiC showed good chemical stability whereas none of the coated specimens were sufficiently stable in the test environment. In most cases, the coating failure was initiated from the edges and sides of the specimens, indicating that the poor quality of the coating in those areas probably resulted in failure.

Additional samples have been prepared with CVD coated TiB_2, TiC and TiN, and sputtered Mo, TiN, TiC, and Cr (singly or as duplex coatings of various combinations). Some preliminary microstructural data of the CVD

*Materials Science Division, ANL.

Table VI-9. Summary of Static Corrosion Results in FeS_2 + LiCl-KCl (1:1 volume) at 500°C

Composition[a]	Coating Thickness, μm	Maximum Test Duration, hr	Comment
Hot Pressed			
TiN	-	1000	No evidence of chemical attack. Weight gain <1%.
TiC	-	300	No evidence of chemical attack. Weight gain <0.02%.
TiB_2	-	300	Minor attack on grain boundaries. Weight loss ~4%.
Coating[b]			
TiN[c]	10-15	1000	Reacted completely. In 300-h tests, discoloration and minor attack on the edges and corners were detected.
TiC	10-20	1000	Reacted completely.
TiCN	20	300	10-15% of the sample reacted completely.
TiB_2[d]	20	143	Reacted completely or severely attacked.
MoS_2	7	300	Reacted completely.
$MoSi_2$	7	300	Reacted completely.
Duplex Coatings			
TiC + TiN	5/5	300	10-20% of the sample reacted completely.
TiN + TiC	5/5	300	Severely attacked.

[a] All coatings were on AISI 1008 steel substrates.

[b] MoS_2 and $MoSi_2$ coatings were deposited by *rf* sputtering. All other coatings were deposited by chemical vapor deposition.

[c] TiN coating was tested in FeS_2 + LiCl-KCl compositions with or without TiN or Fe_2N/Fe_4N addition in the corrosion bath. The additions in the bath did not influence the results to any significant degree.

[d] The corrosion bath composition was FeS_2 + LiCl-KCl with or without elemental boron or FeB/Fe_2B addition.

coated specimens (ANL-78-94, p. 145) indicated that the coatings were 100% dense and free from microcracks, and that the interface between the TiN and TiCN coatings and the substrate appeared to be reasonably adherent. Additional characterization of these coatings and also the sputtered coatings will be done by microstructural and nondestructive techniques to identify local defects in the coated structures. Also, attempts will be made to characterize the coating compositions (such as stoichiometry or impurities) which might strongly influence the stability of the coatings in the test environment. In addition to the static corrosion tests, electrochemical corrosion tests on the coated samples will also be initiated.

Since it is difficult to obtain a defect-free thin coating, we are investigating monolithic conductive ceramics, such as TiN and TiC, which have shown good chemical stability in static corrosion tests. Assembly of a cell having this type of coated current collector will require some development of the current leadout from the ceramic current collector. However, for a preliminary evaluation of the in-cell corrosion behavior of a monolithic conductive ceramic, Cell MS-5 was assembled using a thin (1.9-mm thick) hot-pressed TiN plate that was placed between the two positive electrodes. Current collection from the positive side was achieved through the TiN plate and also through the positive frames (made of Hastelloy B) that were in mechanical contact with the TiN plate. The current leadout was welded to the frames. Operation of this cell has recently been terminated after 32 days and 47 cycles at a discharge current density of 50 mA/m^2. The internal resistance of this cell was initially 23 mΩ. However, with continued cycling, the resistance went up to ∿28 mΩ, thereby indicating the possibility of a loss of good mechanical contact between the TiN plate and the frames. Post-test examination of this cell will begin soon to identify the corrosion behavior of the TiN plate.

VII. SYSTEMS DESIGN AND ANALYSIS

The approaches taken in the design of the systems for the electric-vehicle and stationary energy-storage batteries are discussed below.

A. Conceptual Design of Stationary Energy-Storage Batteries

(S. M. Zivi, J. A. E. Graae,* A. A. Chilenskas, I. Pollack,† H. Kacinskas†)

The objective of this two year engineering study is to produce a conceptual design of a low-cost ($45-55/kW-hr in 1979 dollars) stationary energy-storage battery based on the state of battery technology projected for the mid-1980s. Early in FY 1978, a reference design of a 100 MW-hr energy-storage battery having Li-Al/FeS or Li-Si/FeS cells was devised as a result of a joint effort between ANL and Rockwell International (RI). In creating the reference design, two criteria were adopted: (1) the energy capacity of the cells should not be more than a factor of 10 greater than that of the largest Li/FeS cells presently extant, and (2) the battery configuration should permit the replacement of failed cells without requiring the cooling of the module from its operating temperature. A general description of the ANL/RI design is given in ANL-78-94, pp. 116-120. However, the estimated cost of the battery hardware (exclusive of cells) and installation was found to be $80/kW-hr, which is well over the goal of about $50/kW-hr.‡ Therefore, the FY 1979 effort has been redirected to search for battery concepts that will permit attaining or approaching the cost goal.

Much of the cost of the above conceptual design may be attributed to the two design limitations. Two very costly elements were the submodule, which contains ninety-six 2.5 kW-hr cells, and the charge equalization system. The high cost of the submodule arises from the large number of cells it consists of, and from the requirement that it be replaceable while at the operating temperature (475°C). The high cost of the equalizing system is attributed to the necessity of placing much of the length of the equalizer conductors in the submodule, which is maintained at the operating temperature.

To reduce the battery cost, we have decided to use the largest cell possible within system limitations such as voltage requirements, converter capacity, *etc.* The following requirements were used to determine the largest cell size: (1) battery energy-storage capacity, 100 MW-hr for a 5-hr discharge; (2) nominal size of available ac/dc converters, 10 MW; (3) range of dc voltage permitted for efficient converter operation, 2700 to 1600 V; and (4) range of voltage for an individual cell from the beginning to end of discharge, 1.6 to 1.0 V. These requirements resulted in the selection of two strings of 1680 cells connected in series, each string having one converter.

---

*ETA Engineering.

†Engineering Division at ANL.

‡The cost studies are described in detail in Section II.C.

It follows that each cell should have an energy capacity of about 30 kW-hr, and each string a capacity of 50 MW-hr. The dimensions of the cell are limited by (1) the allowable temperature rise of the cell midpoint during discharge and (2) by the cost and permissible voltage drops of internal bus conductors and current collectors.

These two factors have been analyzed, and limitations to cell size have been identified for a discharge current density of 50 mA/cm^2. If heat is removed from only the two opposing faces of a cell in which the electrodes are vertically loaded, the maximum permissible value for the cell height is about 20 cm. Assuming the cost requirement and a permissible voltage drop of about 20 mV in the internal conductors, the maximum value for the other two dimensions is on the order of 40 cm. These dimensions suggest a capacity limit of about 8 kW-hr for a cell. However, a larger cell can be attained by inserting into a single container several 8 kW-hr assemblages of electrodes and their associated conductors, with each assemblage having its own external terminals, and then connecting these assemblages in parallel (to avoid large potential differences within the cell). Thus, the 30 kW-hr capacity that was found to be desirable for the 100 MW-hr battery can be achieved by combining four elementary 8 kW-hr cells in a single can.

In order to achieve a large amount of stored energy per unit area of floor, the cell height should be as large as practical; this height can be made as large as desired by stacking the electrodes horizontally instead of vertically. A stack height of about two meters has been assumed, which gives cell dimensions of about 2.4 m x 33 cm x 22 cm. A 30 kW-hr cell would thus contain 212 electrode pairs grouped in four elementary 8 kW-hr cells. Each elementary cell would have its own terminals, located on two of the side walls of the cell. Thus, there would be four positive feedthroughs on one side and four negative terminals on the opposite side (the cell can is electrically negative); the positive feedthrough conductors of one cell would be welded (at the battery site) to the negative terminals of the adjacent cell.

This free standing cell concept assumes the technical feasibility of the use of horizontally oriented electrodes and submerged feedthroughs. Future experimental research is needed to validate these assumptions.

In the modified 100 MW-hr battery design, 168 cells would be electrically connected to form a module having an energy capacity of 5 MW-hr. Ten such modules would be connected in series to form one of two 50 MW-hr battery banks, each of which would have an ac/dc converter. The size of the module is limited mainly by the maximum dimensions allowable for truck transport of prefabricated structures from factory to battery site. A width of 2.1 m (7 ft) and height of 2.4 m (8 ft) for the module (insulation not included) are thought to be optimal. The length of the module can be selected somewhat more freely. The longer the module, the more field labor will be required in assembling it at the site, and the greater the loss of electrical capacity when a module has to be cooled for repair. Obviously, shorter modules will entail more modules for the system, excess inter-module bus work, and more heat loss through end walls. We have selected a module length of 12 m (40 ft).

A high-temperature glass wool insulation, 30 cm thick (1 ft), would be attached to the module (ends, bottom, and sides) to reduce heat losses to about 20 kW, which is about 40% of the average net heat generated in the module on a daily charge-discharge cycle. The remaining 60% of the generated heat would be disposed of by a cooling system in which the coolant (air at about 400°C) is circulated through cooling coils arrayed between cells, radiative heat transfer being the principal mode of heat transfer from cells to coils. The coils and the circulating air within them also would serve to redistribute heat among the various cells of the module. The assembled module would be placed on concrete footings, which would be protected against exposure to high temperatures by a structural design which incorporates a load-bearing thermal barrier between the module and the footing.

In the stationary energy-storage battery, each cell must be connected to a charge-equalization electronic module, which is located externally to the module since it cannot tolerate the 450°C to 500°C temperature range. The voltage drop in the equalizing conductors is an important consideration, and a significant advantage of the postulated module design is that it permits these conductors to operate at ambient temperature where their resistance is relatively low. The charge equalization system has been designed for an equalizing current of 30 A, which corresponds to a range of coulombic efficiency (difference between best and worst cell) among the 168 cells in a module of about 0.4% after about ten years of operation. This is equivalent to a coulombic efficiency range of about 4% in the smaller electric-vehicle cells now being developed.

B. Thermal Management Studies

(M. Farahat, A. Jackson*)

The current thrust of the thermal management studies is directed to the forthcoming tests to be performed with the 40 kW-hr Mark IA electric-vehicle battery. In preparation for these tests, thermal tests were conducted on the 6-V module (described in Section II.A) while it was being cycled in the laboratory and in a van. Stationary cycling of this 6-V battery at ANL (discussed further in Section III.D) showed that a slow accumulation of a gas within the vacuum annulus had raised the pressure above the level required to maintain good insulating properties. This gas was later identified, using a mass-spectrometer, to be hydrogen. For subsequent laboratory tests, the pressure of hydrogen was reduced to an acceptable level, about 0.026 Pa (2×10^{-4} torr), by the use of an ion-pump or a room-temperature getter that was selective for hydrogen. Typical heat loss rates at a pressure of 0.026 Pa were found to be 160 W, with a battery operating temperature of 465°C. At 465°C, the case outside temperature was ∿30°C, the back side being ∿40°C and the front flange ∿50°C. These results further reinforce our expectation of achieving the goal of 400 W heat loss for the 40 kW-hr Mark-IA battery.

For the road test of this battery, it was connected in series to twenty-four 6-V lead-acid batteries in an electric van and heated to 475°C, and a room-temperature getter was connected to the vacuum annulus to control the hydrogen pressure (slow diffusion of trace quantities of hydrogen through the inner case was still occurring at this time). The results of the van test

*Components Technology, ANL.

showed that heat generation within the cells can keep the module temperature well within operating limits (420-500°C). The 6-V module, which had a heat loss rate of ∿160 W, dropped only 5°C in one hour. This means that vehicle operation in excess of four hours can be tolerated without having to rely on auxiliary heaters. The Mark IA battery, which has a much lower heat loss/energy storage ratio than the 6-V module, will slowly increase in temperature under the same driving conditions.

C. Safety Tests
(A. A. Chilenskas)

The Budd Co. has recently completed safety tests on two multiplate Li-Al/FeS cells fabricated by Eagle-Picher for the Mark IA battery program. Two Mark IA cells in the fully charged condition (taken to be the worst case) at 460°C were crushed in a drop-tower test that duplicated the impact of a 50 km/hr (30 mph) barrier crash. The cells were crushed by the impact of a 50 kg weight dropped from a tower to about 66% of their normal thickness, resulting in the cell contents being exposed to air; no evidence was detected of an explosion, electric arcing, electrolyte dispersion, fire, or fumes. Samples taken for hydrogen and hydrogen sulfide at the test site immediately after the test showed no evidence of these gases, although an oder taken to be H_2S or SO_2 was noticed. An analysis was conducted on the forces and cell deflection obtained by the Budd Co. and it was concluded that in a battery containing cells of this type the battery pack may have to be restrained (*e.g.*, use the vehicle frame to provide energy absorption in a crash) or the cell energy may have to be attenuated with supplementary absorbers (*e.g.*, a crushable battery case). These tests are taken as further evidence to support our contention that lithium/metal sulfide batteries can be safely engineered for electric vehicles.

VIII. CALCIUM/METAL SULFIDE BATTERY DEVELOPMENT

The objective of this program is to develop high-performance cells that use inexpensive, abundant materials while maintaining the performance levels required for electric vehicles or load leveling. These cells are expected to follow the lithium/metal sulfide cells into commercial production. The present goals for the cells are a specific energy of 160 W-hr/kg (same as Mark III goals listed in Table I-1) and a materials cost in mass production of $15/kW-hr (1979 dollars). Previous to this report period, studies were conducted with cells having negative electrodes of either calcium or magnesium alloy, positive electrodes of metal sulfide, and a molten-salt electrolyte. However, owing to problems with the magnesium system, we have decided to concentrate further efforts on development of the more promising calcium cell.

A. Electrolyte Development

(C. C. Sy, L. E. Ross, M. F. Roche)

Our studies of electrolytes since the last report (ANL-78-94, p. 187) have concentrated mainly on the properties of 29 mol % LiCl-20 mol % NaCl-35 mol % $CaCl_2$- 16 mol % $BaCl_2$ (mp, 390°C), which has been operated successfully in combination with FeS_2 and NiS_2 electrodes (ANL-78-94, p. 188). This electrolyte is one of three known eutectics in this quaternary system;[24] Table VIII-1 presents the compositions and melting points of these eutectics. Melting-point measurements were made on twenty mixtures of LiF (0-4 mol %), LiCl(3-33 mol %), NaCl(12-38 mol %), $CaCl_2$(35-47 mol %), and $BaCl_2$(7-20 mol %) to find electrolytes with a low lithium content and a low melting point. None of these electrolytes had melting points below 383°C. Thus, it appears that E_2 and E_3 are the only eutectics with a low melting point and a low lithium content in this system. At present, E_3 is being used in cell development work, but E_2 may also prove useful since its melting point is slightly lower than that of E_3, according to our measurements. With either E_2 or E_3, calcium/metal sulfide cells will contain less than 1 wt % lithium and will thus be low in cost. The studies conducted on E_3 during this period are described below.

Table VIII-1. Eutectics in Quaternary System

	Eutectic Composition, mol %		
	E_1	E_2	E_3
LiCl	47	33	29
NaCl	3	12	20
$CaCl_2$	30	37	35
$BaCl_2$	20	18	16
Melting pt.,[a] °C	(395)	383 (385)	390(378)

[a]The numbers in parenthesis are the melting points for these eutectics reported in Ref. 1.

1. Solubility Studies

The CaS solubility in 29 mol % LiCl-20 mol % NaCl-35 mol % $CaCl_2$-16 mol % $BaCl_2$ was determined by chemical analysis. For this analysis, the electrolyte was saturated with CaS at various temperatures in a helium-atmosphere furnace, and the sulfide concentrations were measured by gas-chromatographic assay of the H_2S evolved on dissolving the samples in 6*M* HCl.* Standard curves for this analysis were established by assays of known volumes of H_2S; air oxidation of the samples and standards was avoided by employing a helium carrier gas.

Two methods of sampling the CaS-saturated molten electrolyte were tried. In the first method, quartz sampler tubes with 40-micron quartz frits were used to draw samples from a CaS suspension in the molten electrolyte. This method led to poor results, the calcium sulfide concentrations at 430°C varying from ∿150 to ∿6000 ppm. The poor results were thought to be due to a CaS particulate contamination of the samples. In the second method, 5 g of CaS was placed in a sintered stainless-steel packet (25 cm^2) with 15-20 μm-dia holes, which was then immersed in a Al_2O_3 crucible (250 cm^3) containing 295 g of molten electrolyte. The packet was flooded with electrolyte by alternate helium evacuations and repressurizations. Samples were obtained at various temperatures by immersing a small (5 cm^3) Al_2O_3 crucible in the electrolyte surrounding the packet and equilibrating for 4-5 days before withdrawing the filled crucible. A calibrated chromel-alumel thermocouple was used to monitor the temperature of the electrolyte.

The solubility of CaS in electrolyte as a function of temperature is shown in Fig. VIII-1; these data were determined by the second method described above. Also included in this figure is the solubility of Li_2S in LiCl-KCl.[25] M.-L. Saboungi-Blander† computed the solubility product of CaS at 723 K in LiCl-KCl electrolyte from thermodynamic data; the solubility product divided by the ion fraction of Ca^{++} in LiCl-NaCl-$CaCl_2$-$BaCl_2$(0.35) is also plotted in this figure for comparison with the linear regression curve of the CaS data. It is apparent that the solubility product of CaS in the two electrolytes is similar and is lower than that of Li_2S in LiCl-KCl. The heat of solution was calculated from the slope of the solubility curves, and was found to be 10.22 kcal/mol for Li_2S in LiCl-KCl[25] and 7.97 kcal/mol for CaS in LiCl-NaCl-$CaCl_2$-$BaCl_2$.

The above data are expected to be of use for thermodynamic and kinetic comparisons of calcium and lithium cells. For example, emf differences between the positive electrodes in calcium and lithium cells can be derived from the ratio of the CaS-to-Li_2S solubility. This ratio indicates that, at 441°C, an Fe-FeS-CaS electrode would be 78.5 mV more cathodic than an Fe-FeS-Li_2S electrode.

---

*Assays conducted by M. Bouchard, A. Essling, and M. Homa, Analytical Chemistry Laboratory, ANL.

†Chemical Engineering Division at ANL.

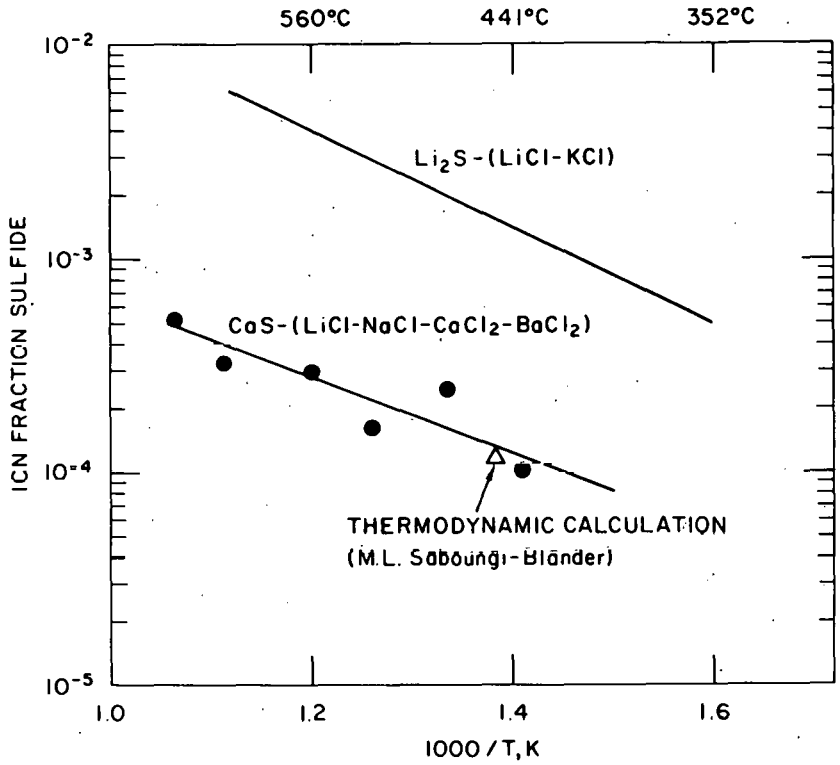

Fig. VIII-1. Solubility of Li_2S in LiCl-KCl and CaS in LiCl-NaCl-$CaCl_2$-$BaCl_2$

2. Vaporization of Sulfur

In an earlier study (ANL-77-75, p. 50), A. E. Martin showed that suspensions of Li_2S and either FeS_2 or NiS_2 in LiCl-KCl electrolyte at 525°C lost sulfur through vaporization at a much higher rate than that of similar mixtures not containing Li_2S. In addition, post-test examinations of Li-Al/FeS_2 and Li-Al/NiS_2 cells (see Section IV.C) have shown that Li_2S deposits form in the BN fabric separator of the cells. These two phenomena may occur through similar mechanisms, namely, the formation and transport of polysulfide ions (*e.g.*, $S_n^=$) in the electrolyte. Such ions could be reduced by Li-Al to form a Li_2S deposit in sealed cells or could be decomposed by heat to form $S^=$ ions and gaseous sulfur in unsealed mixtures. We suspected that, in calcium cells, the low solubility of CaS (see above) would lead to less polysulfide formation, and consequently, good sulfur retention by the positive electrodes. In the present study, weight loss experiments similar to those of Martin were conducted to measure the sulfur loss by vaporization. In later studies, a search for CaS deposits in the BN separator of Ca alloy/FeS_2 cells will be conducted.

The vaporization tests were conducted by heating a suspension of FeS_2, with and without CaS, in 29 mol % LiCl-20 mol % NaCl-35 mol % $CaCl_2$-16 mol % $BaCl_2$. For comparison, a suspension of Li_2S and FeS_2 in LiCl-KCl was included in the test. The sample mixtures contained ∿0.5 g of sulfides and ∿1.5 g of electrolyte. They were heated simultaneously at about 520°C in graphite crucibles (1.27-cm inside diameter) in a helium-atmosphere furnace, and were occasionally removed, cooled, and weighed. Sulfur-to-iron

ratios* for these two suspensions and FeS_2 alone as a function of heating time are given in Fig. VIII-2. The data show that CaS has little effect on vaporization and confirm the previous finding of a rapid sulfur loss in Li_2S-FeS_2 mixtures.

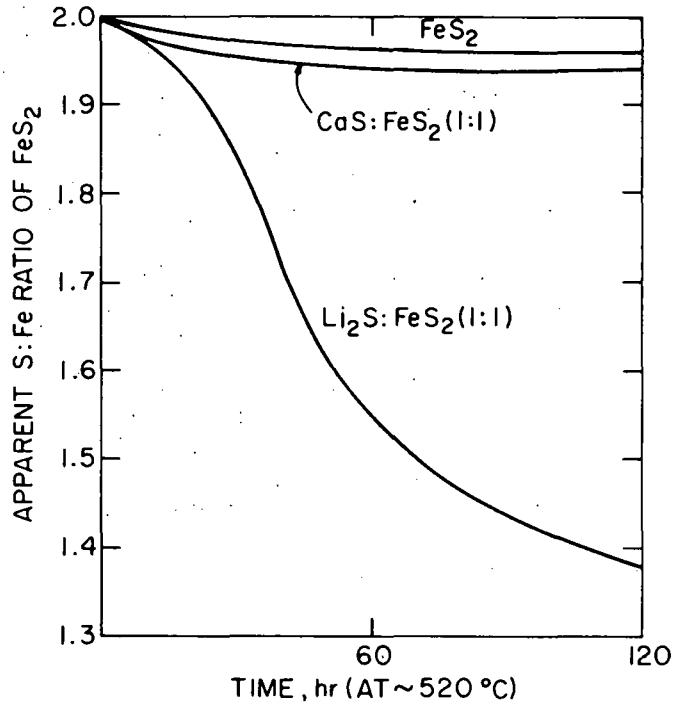

Fig. VIII-2. Sulfur Vaporization Losses From Li_2S-FeS_2(in LiCl-KCl) and CaS-FeS_2 (in LiCl-NaCl-$CaCl_2$-$BaCl_2$)

A similar test was conducted with suspensions of NiS_2 (with and without CaS) in the quaternary salt. Again, CaS had little effect on vaporization. Both the NiS_2 and the NiS_2:CaS (1:1) samples exhibited losses of about 0.15 moles of sulfur per mole of nickel within 20 hr, and about 0.25 moles of sulfur per mole of nickel after 120 hr.

Assuming vaporization losses and electrode losses occur by a similar mechanism, the above experiments suggest that FeS_2 and NiS_2 electrodes will retain sulfur reasonably well in calcium cells.

3. Conductivity and Density Calculations

Using data from the literature,[26] we calculated the conductivity (κ) and density (ρ) of 29 mol % LiCl-20 mol % NaCl-35 mol % $CaCl_2$-16 mol % $BaCl_2$. The equations used for these calculations were as follows:

---

*It was assumed that weight losses occurred exclusively through sulfur vaporization from the FeS_2.

$$\rho = \left(\sum_{i=1}^{4} \frac{f_i}{\rho_i} \right)^{-1} \quad (1)$$

where f_i and ρ_i are the weight fraction and density, respectively, of the i^{th} component; and

$$\kappa = \rho \left(\sum_{i=1}^{4} g_i \Lambda_i \right) \left(\sum_{i=1}^{4} g_i e_i \right)^{-1} \quad (2)$$

where g_i, Λ_i, and e_i are, respectively, the equivalent fraction, equivalent conductivity, and equivalent weight of the i^{th} component.

The calculated κ and ρ at 427 and 527°C of the quaternary salt and the experimental κ and ρ at these two temperatures of the binary salt[27] are presented in Table VIII-2. The quaternary salt, according to these calculations, is about 40% denser than LiCl-KCl (a significant weight penalty), but has about the same conductivity. However, the calculated conductivity may be too high since ion association in the quaternary salt could lower the conductivity significantly. Conductivity measurements will be required to test the above calculations.

Table VIII-2. Molten-Salt Densities and Conductivities

Electrolyte	Density, g/cm^3		Conductivity, $(\Omega\text{-cm})^{-1}$	
	427°C	527°C	427°C	527°C
LiCl-KCl	1.660	1.607	1.426	2.023
LiCl-NaCl-$CaCl_2$-$BaCl_2$	2.331	2.278	1.483	1.913

B. Positive Electrode Development

1. Cell Studies

(L. E. Ross, S. K. Preto, C. C. Sy)

In the last report (ANL-78-94, p. 190), development work on negative-electrode materials was discussed. From those studies, the Ca-Si negative electrode ($CaSi_2$ uncharged; Ca_2Si charged) was selected for engineering-scale development. Recent studies have concentrated on development of three types of positive electrode--NiS_2, FeS_2 and FeS_2-CoS_2.* In later studies, FeS electrodes will be tested.

*In lithium cells, CoS_2 is normally added to the FeS_2 electrode to improve performance.

The test cells employed metal-disulfide electrodes with theoretical capacities of about 4 A-hr. The metal disulfide (NiS_2, FeS_2, and $Fe_{0.93}Co_{0.07}S_2$) was packed in carbon foam and then placed within molybdenum sheet-and-screen housings (area, 3.25 cm^2; 0.8-cm thick). The theoretical capacity densities are 1.00 A-hr/cm^2 for the NiS_2 electrode and 1.20 A-hr/cm^2 for the FeS_2 and FeS_2-CoS_2 electrodes. The negative electrode was a 7-10 A-hr $CaAl_2$ electrode in an iron housing (area, 16 cm^2). The reference electrode was a mixture of $CaAl_4$ and aluminum and was used to control voltage limits.* Zirconia cloth was used as a particle retainer and BN fabric as a separator, and the electrolyte was the quaternary salt described above (E_3) (purified by Anderson Physics Laboratory). The cells were operated at 460°C in alumina crucibles, the positive electrodes being cycled between IR-included voltages of 2.1 V on charge and 1.0 V on discharge.

The achieved capacity densities for the NiS_2, FeS_2, and $Fe_{0.93}Co_{0.07}S_2$ electrodes are shown in Fig. VIII-3. The maximum electrode utilizations (theoretical capacity density divided by achieved capacity density) were very satisfactory--64% for NiS_2 and FeS_2 and 72% for $Fe_{0.93}Co_{0.07}S_2$. The beneficial effects of cobalt are evident from the high achieved capacity density of the $Fe(Co)S_2$ electrode. The achieved capacity of the $Fe(Co)S_2$ electrode in the above calcium cell is similar to that obtained in earlier $LiAl/Fe(Co)S_2$ cells (ANL-75-1, pp. 29-32). All three

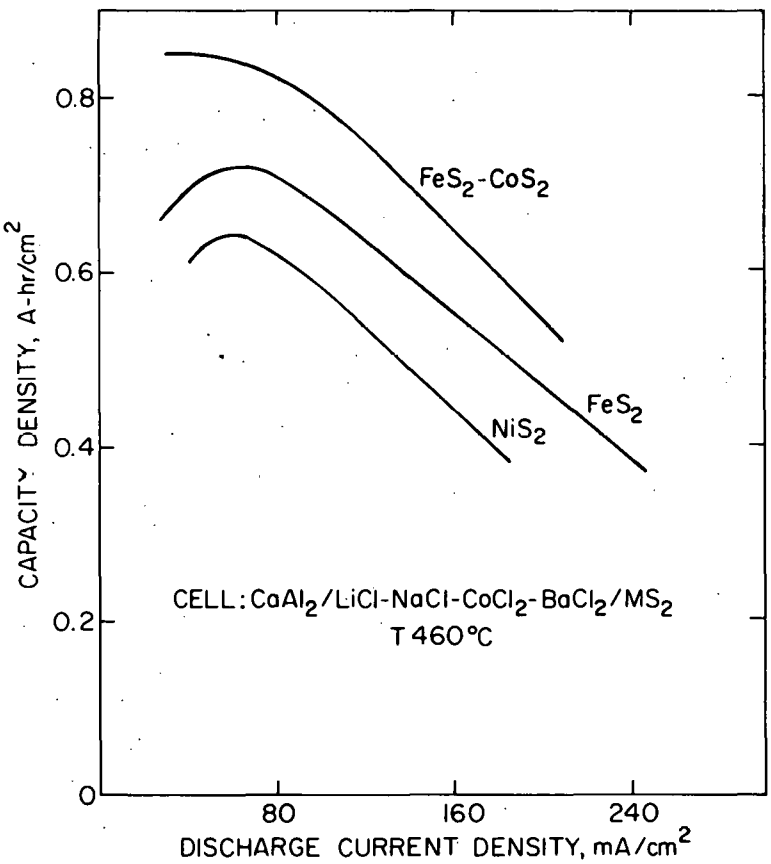

Fig. VIII-3. Capacity Density of Metal Disulfide Electrodes in $LiCl-NaCl-CaCl_2-BaCl_2$

*This avoided inclusion of the $CaAl_2$ negative electrode in the polarization measurements, and thus simplified interpretation of the results.

cells were operated for about 60 cycles with no decline in their coulombic efficiency, which was typically about 98%. However, the NiS_2 electrode exhibited a capacity decline with cycling; post-test examination revealed that the electrode retainers had loosened because of swelling. It is therefore believed that active material was lost in the NiS_2 electrode. Aside from this problem, no major difficulties were encountered with the cell operations.

2. Cyclic Voltammetry of Metal Disulfides
(S. K. Preto)

Previous studies of slow-scan (0.02 mV/sec) voltammograms (ANL-78-94, pp. 168-173, 188-190) were conducted to determine the electrochemical behavior of FeS_2, CoS_2, and NiS_2 electrodes in lithium-cell and calcium-cell electrolytes. In the present study, voltammograms at scan rates of 0.02 to 0.5 mV/sec were generated from these three metal disulfide electrodes in LiCl-KCl electrolyte and LiCl-NaCl-$CaCl_2$-$BaCl_2$ electrolyte. In both electrolytes the working electrodes were ∿100 mg of powdered metal disulfide (FeS_2, NiS_2, CoS_2) in carbon foam within a molybdenum housing (1 cm^2). The counter and reference electrodes were two-phase mixtures of LiAl and Al for the LiCl-KCl electrolyte and $CaAl_4$ and Al for the LiCl-NaCl-$CaCl_2$-$BaCl_2$ electrolyte. The working electrodes were repeatedly cycled over a potential range of 1.0 V to 2.0 or 2.1 V *vs* the reference electrodes.

The data obtained from the voltammetry studies were then used to determine the peak current (i_p) and peak potential (E_p) at scan rates of 0.02 to 0.5 mV/sec for each of the major reactions of the individual electrodes; these reactions and their emf's are listed in Table VIII-3.* The

Table VIII-3. Emf of Metal-Disulfide Electrode Reactions

	Emf, Volts	
	vs LiAl at 400°C	*vs* $CaAl_4$ at 460°C
$FeS_2 \rightarrow Fe_{1-x}S$	1.74[a]	1.78
$FeS \rightarrow Fe$	1.34[b]	1.39
$CoS_2 \rightarrow Co_3S_4$	1.74	1.79
$Co_3S_4 \rightarrow Co_9S_8$	1.63	1.68
$Co_9S_8 \rightarrow Co$	1.35	1.40
$NiS_2 \rightarrow Ni_{1-x}S$	1.75	1.81
$NiS \rightarrow Ni_7S_6$	1.60	1.65
$Ni_7S_6 \rightarrow Ni_3S_2$	1.56	1.59
$Ni_3S_2 \rightarrow Ni$	1.37	1.42

[a] In-cell reaction: $FeS_2 \rightarrow Li_3Fe_2S_4$.

[b] In-cell reaction: $Li_2FeS_2 \rightarrow Fe$.

*Previously reported in ANL-78-94, p. 173 and 189.

results indicated that i_p and E_p vary linearly with the square root of the scan rate, thereby indicating that ohmic effects are dominant in these electrode reactions. Figure VIII-4* shows the peak current as a function of peak potential for the major reactions of the three metal disulfide electrodes in LiCl-KCl, and Figure VIII-5* shows the same type of plot for the reactions of the FeS_2 and CoS_2 electrodes in the quaternary salt. (Because of a variety of experimental difficulties, data for NiS_2 in the quaternary salt have not yet been obtained; these data will be presented in a future report.) As can be easily seen in these two figures, the peak current *vs* peak potential curves are linear. The linear regression curves through these data intercept the voltage axis at voltages slightly above the reaction emf on charge and slightly below the reaction emf on discharge. Note that two closed symbols are shown on the voltage axis (*i.e.*, at zero current) for each reaction. These represent the scan-rate-independent potential at which the discharge peak and charge peak start. These symbols are located slightly below the discharge and slightly above the charge reaction emf.

The information in Figs. VIII-4 and -5 is of use in making qualitative comparisons of the lithium and calcium cell systems. Some of the interesting features are as follows:

1) The resistances, which are the reciprocals of the slopes, are generally much lower in the lithium than in the calcium system. However, this effect may be due to differences in cell design. For example, the lithium tests were run in a smaller cell in which the electrodes were more closely spaced; this difference in cell design could have minimized the cell resistance. We will investigate this apparent conductivity problem in calcium cells in later studies.

2) As can be seen in the two figures, for a given electrode reaction, the charge resistance and discharge resistance often differ greatly. Ideally, these resistances are equal and about the same for all reactions in a given electrode. The NiS_2 electrode in LiCl-KCl most closely approximates this condition. For the other electrodes, various resistance problems are evident. We are unable to account for all these resistive effects with a simple model, but it seems appropriate to assess the influence of electrolyte composition on the curve slopes in later studies.

3) The discontinuity between the point at which the charge and discharge curves for a given reaction intercept the voltage axis have been attributed to "crystallization overpotentials" of the type discussed by Vetter.[28] For example, in studies of metal electrodeposition, crystallization overpotentials have been found to range from ∿10 to ∿300 mV. In Figs. VIII-4 and -5, both the closed symbols and the voltage intercepts for a given reaction are separated by ∿20 to ∿110 mV. This separation would be zero in the absence of crystallization problems. On the basis of their low crystallization overpotentials, the NiS_2 electrode in LiCl-KCl and FeS_2 electrode in $LiCl-NaCl-CaCl_2-BaCl_2$ appear to be better than the other electrodes tested.

* In these figures, data for charge are above the voltage axis, and data for discharge are below the axis. The open symbols represent the i_p and E_p for a given scan rate; the closer the symbol is to the voltage axis, the lower the scan rate.

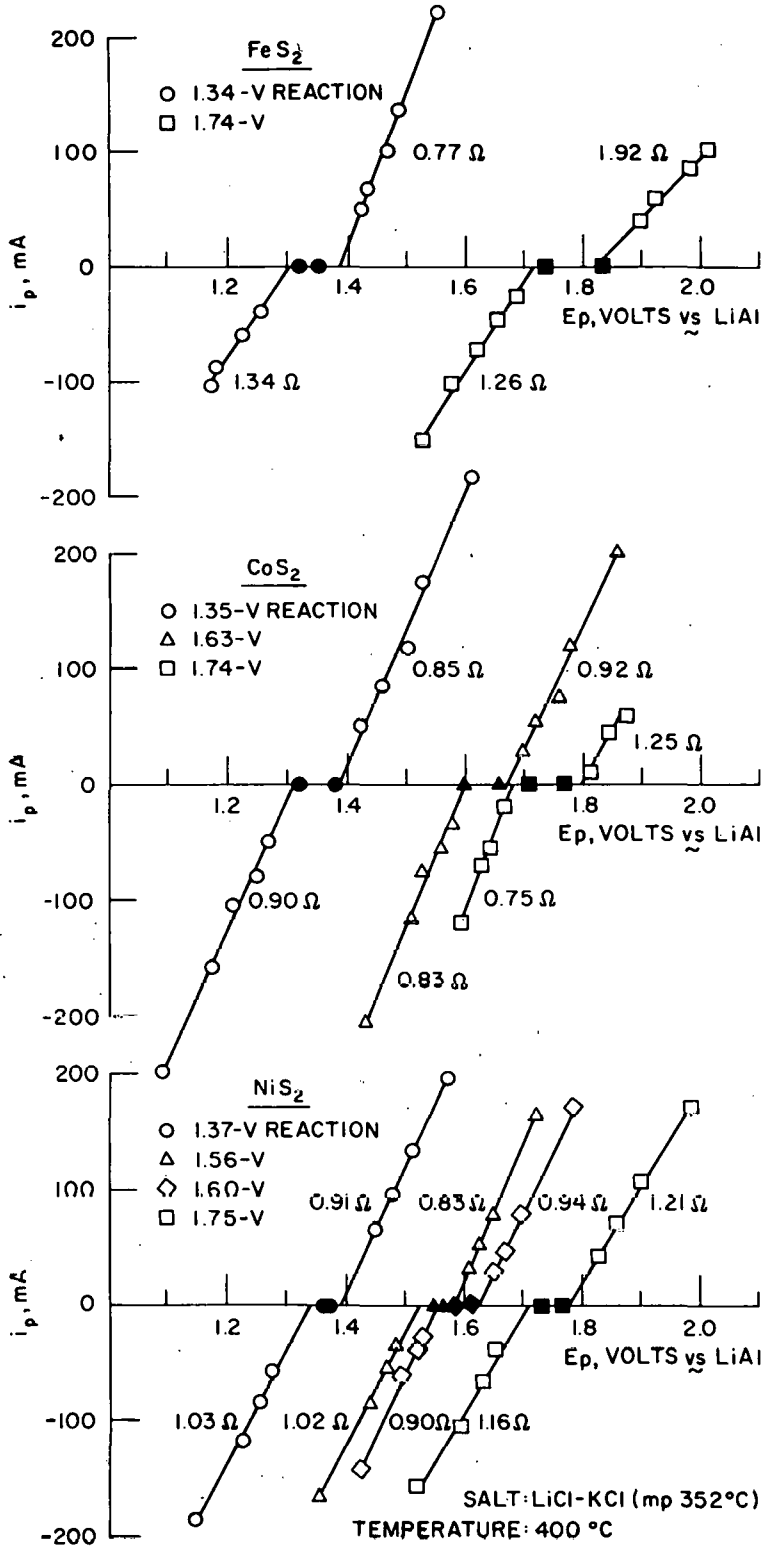

Fig. VIII-4. Peak Currents *vs* Peak Potentials of Metal Disulfides in LiCl-KCl

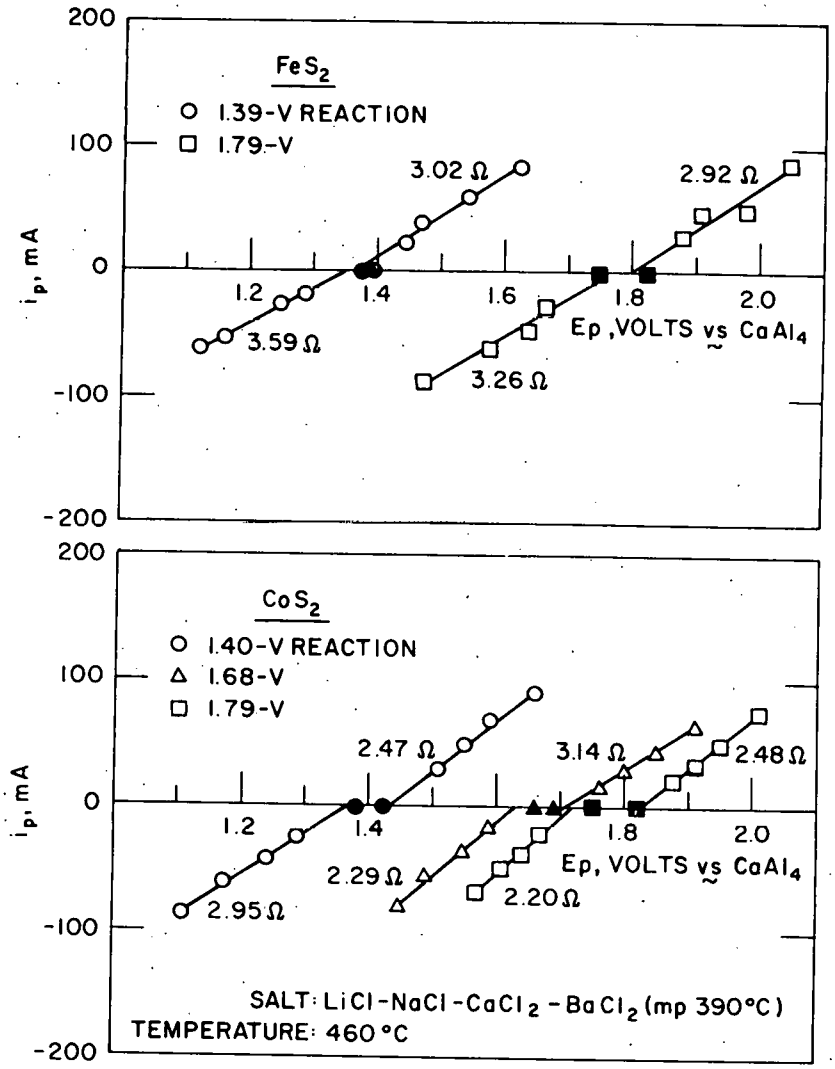

Fig. VIII-5. Peak Current *vs* Peak Potential of Metal Disulfides in LiCl-NaCl-$CaCl_2$-$BaCl_2$

4) Not evident from the figures, but very obvious during the studies, was the rapid loss with cycling in the capacity of the high-voltage reactions of the metal disulfide electrodes in LiCl-KCl electrolyte; this effect is thought to be due to escape of sulfur from these electrodes. In comparison with the electrodes in the lithium system, the electrodes in LiCl-NaCl-$CaCl_2$-$BaCl_2$ did not exhibit this capacity loss even though their operating temperatures were higher, and they generally exhibited much higher utilization. The low rate of capacity loss may be due to the low solubility of CaS.

In summary, in terms of their overall electrochemical properties, NiS_2 in LiCl-KCl and FeS_2 in the quaternary salt are the better electrode systems.

C. Engineering-Scale Cell Tests

(L. E. Ross, L. G. Bartholme, P. F. Eshman, M. F. Roche)

The engineering-scale cell tests have two purposes: to provide information on capacity decline mechanisms and cell performance characteristics under practical conditions, and to provide a convenient measure of progress toward the program goals.

1. Cell CA-15

This cell was the first engineering-scale cell having the quaternary electrolyte LiCl-NaCl-$CaCl_2$-$BaCl_2$ (mp, 390°C). The cell had a sealed, prismatic (13.5 x 13.5 x 3.5 cm) bicell design. Each of the two 0.7-cm-thick negative electrodes contained 1 mole of $CaSi_2$, and the 1.5-cm-thick positive electrode contained a mixture of 1 mole of $Ni_{2.79}Co_{0.21}S_2$ (loaded as Ni + NiS + CoS_2) and 4 moles of CaS. Based on the added CaS, the theoretical capacity of the cell was 214 A-hr. The current collectors were honeycomb structures of iron in the negative electrode and molybdenum in the positive electrode. Particle retention was provided by molybdenum screen and BN felt on the positive electrode and stainless steel screens on the negative electrodes; the separator was BN fabric.

Salt filling of Cell CA-15 was a slow operation (taking about 25 cycles) because of a gassing problem. In out-of-cell experiments conducted by C. Sy with the support of the Analytical Chemistry Laboratory at ANL, the gassing was traced to the presence of 13 wt % $Ca(OH)_2$ in the CaS, which led to hydrogen generation when the hydroxide contacted the negative electrode. Subsequently, a supply of high-purity calcium sulfide (98 wt % CaS) was obtained from a commercial source (Ventron), and was used in Cell CA-16.

The coulombic efficiencies and specific energies during cycling of this cell are summarized in Fig. VIII-6. Most of these cycles were at a temperature of 470°C and a current of 5 A (20-hr discharges at a specific energy of 60 W-hr/kg; 10-hr discharges at 38 W-hr/kg), but a current of 10 A was used near cycle 30 and between cycles 40 and 60 and a temperature of 435°C was used near cycle 80. Two problems are evident from the data in Fig. VIII-6. First, the coulombic efficiency is low in early cycles and increases with cycling, indicating a chemical reaction that consumes capacity. Second, the specific energy declines during cycling; in addition, the resistance was found to increase during cycling, from 10 to ~25 mΩ.

2. Cell CA-16

Cell CA-16 was identical to Cell CA-15 except for the following: iron was substituted for nickel (thus the positive active material was Fe + FeS + CoS_2 + CaS), and four layers of carbon foam* (12 x 12 x 0.7 cm each) current collector were compressed into the 1.5 cm-thick positive electrode as it was hot pressed.

*Supplied by Chemtronics International, Inc., Ann Arbor, Mich.

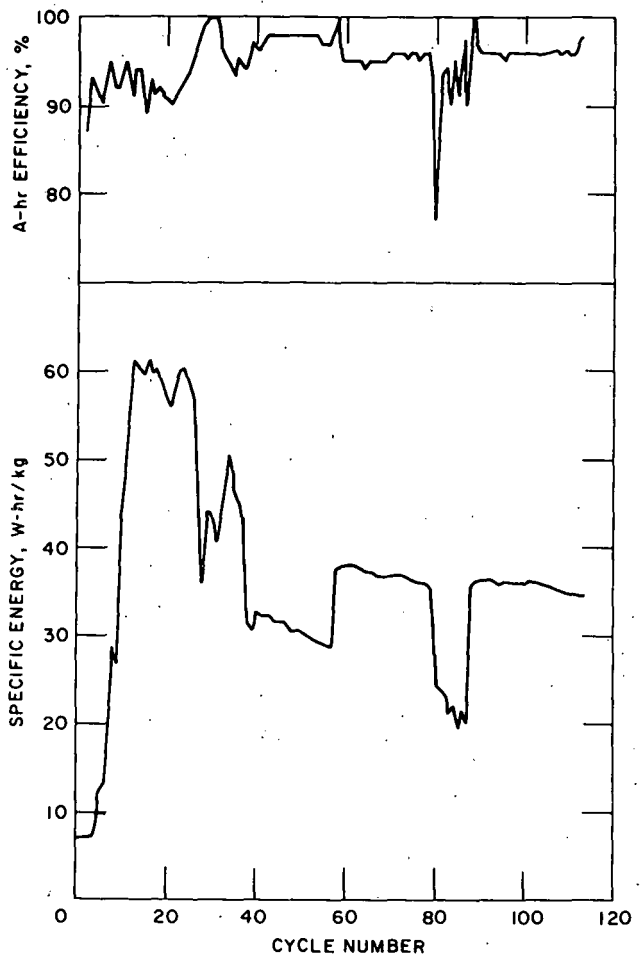

Fig. VIII-6. Performance Data on Cell CA-15

This cell is presently under test at 460°C. It has achieved a higher specific energy than previous calcium cells, 78 W-hr/kg, which is about 60% of the specific energy of a comparable Li-Al/FeS_2 bicell* (Fig. VIII-7). During the first 35 cycles, the cell resistance increased from 8 to 15 mΩ, and the capacity decreased from 118 to 76 A-hr. In addition, the coulombic efficiency was low (∿90%) in early cycles, but it had increased to 99% by cycle 30. Thus, this cell has cycling problems similar to those of Cell CA-15. The causes of these effects will be sought during post-test examinations of Cells CA-15 and CA-16.

3. Performance Summary

The performance of the three most recent engineering-scale cells is given in Table VIII-4. As can be seen in this table, significant improvements in specific energy have been made in the calcium cells (from

*Fabricated by Eagle-Picher and tested at ANL.

42 to 78 W-hr/kg). Methods of eliminating the decline in specific energy with cycling will be investigated as more engineering-scale cells are fabricated.

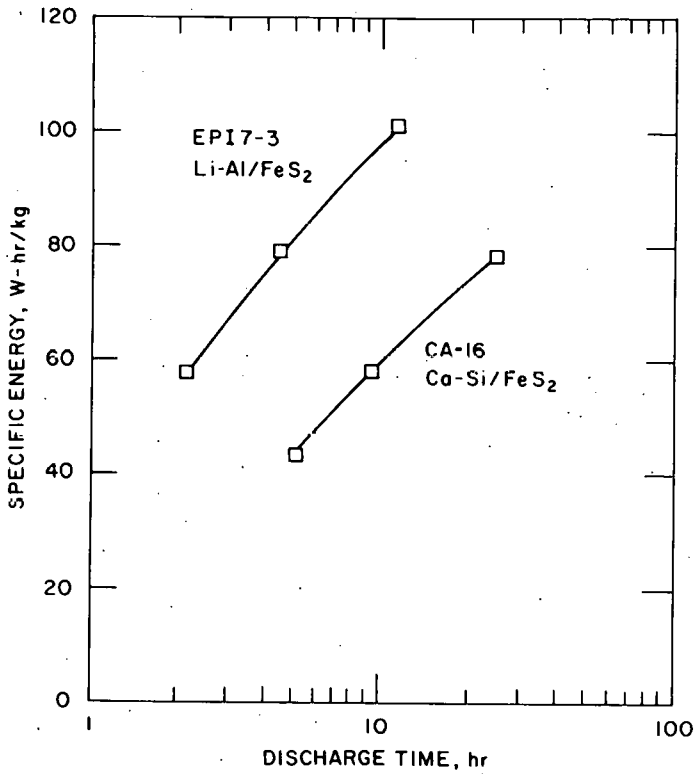

Fig. VIII-7. Specific Energy of a Calcium and Lithium Cell

Table VIII-4. Performance of Three Calcium Cells

Cell No.	Specific Energy, W-hr/kg		A-hr Eff., %		Cycles Operated
	Max.	Final	Initial	Final	
CA-14[a]	42[b]	31[b]	99	74	120
CA-15	61[c]	34[c]	90	97	115
CA-16	78[c]	d	88	e	>30

[a]This $Ca(Mg_2Si)/NiS_2$ cell was reported in ANL-78-94, p. 185.

[b]Measured at a current of 6 A (6-hr rate).

[c]Measured at a current of 5 A (20-25 hr rate).

[d]Cell still operating; specific energy has declined by 35%.

[e]At present, 99% on cycle 30.

REFERENCES

1. Y.-W. Hu, I. D. Raistrict, and R. A. Huggins, *Ionic Conductivity of Lithium Orthosilicate - Lithium Phosphate Solid Solutions*, J. Electrochem. Soc., *124* (8), 1240 (August 1977).

2. ERDA/JPL-1012-76/3, *The Cost of Energy from Utility-Owned Solar Energy Systems*, Jet Propulsion Laboratory JPL5040-29 (June 1976).

3. U. S. Energy Research and Development Administration, Office of Electric and Hybrid Vehicles, *Test and Evaluation Procedures for Electric Vehicles*, (1976).

4. N. P. Yao, L. A. Heredy, and R. C. Saunders, J. Electrochem. Soc. *118*, 1039 (1971).

5. C. H. Liu, A. J. Zielen and D. M. Gruen, J. Electrochem. Soc. *120*, 67 (1973).

6. M. L. Saboungi, J. Marr, and M. Blander, J. Chem. Phys. *68*, 1375 (1978).

7. M. L. Saboungi, J. Marr, and M. Blander, J. Chem. Phys. *125*, 1567 (1978).

8. J. Newman and Richard Pollard, University of California, private communication (1978).

9. J. Newman, University of California, private communication.

10. C. E. Vallet and J. Braunstein, J. Electrochem. Soc. *125*, 727 (1978).

11. D. F. Pridmore and R. T. Shuey, American Mineralogist *61*, 248 (1976).

12. A. L. Echarri and C. Sanchez, Solid State Comm. *15*, 827 (1974).

13. W. D. Johnston, R. C. Miller, and D. H. Damon, J. Less Common Metals *8*, 272 (1965).

14. D. Argyriades, G. Derge, C. M. Pound, Trans. Met. Soc. AIME *215*, 909 (1959).

15. J. P. Suchet, *Crystal Chemistry and Semiconduction in Transition Metal Binary Compounds*, Academic Press, New York, p. 211 (1971).

16. D. F. A. Koch, *In Modern Aspects of Electrochemistry, No. 10*, J. O'M. Bockris and B. E. Conway, eds., Plenum Press, New York, p. 212 (1975).

17. R. J. Heus and J. J. Egan, J. Phys. Chem. *77*, 1989 (1973).

18. W. M. Latimer, J. Am. Chem. Soc. *73*, 1480 (1950).

19. N. P. Yao, L. A. Heredy, and R. C. Saunders, J. Electrochem. Soc. *118*, 1039 (1971).

20. *JANAF Thermochemical Tables,* Dow Chemical Co., Midland, Mich. (1965).

21. K. C. Mills, *Thermodynamic Data for Inorganic Sulfides, Selenides, and Tellurides,* Butterworths, London (1974).

22. J. F. Elliott and M. Gleiser, *Thermochemistry for Steelmaking,* Vol. 1, Addison-Wesley Publishing Co., Reading, Mass. (1960-1963).

23. M. M. Farahat, J. A. E. Graae, A. A. Chilenskas, and D. L. Barney, *Thermal Management of the Lithium/Metal Sulfide Electric Vehicle,* SAE Meeting, February 22, 1979, Detroit, Michigan.

24. T. V. Tsyvenkova *et al.,* Russ J. Inorg. Chem. *18,* 426 (1973).

25. M.-L. Saboungi, J. J. Marr, M. Blander, J. Electrochem. Soc. *125,* 1567 (1978).

26. G. J. Janz, *Molten Salts Handbook,* Academic Press, New York (1967).

27. E. R. Van Artsdalen and I. S. Jaffe, J. Phys. Chem. *59,* 118 (1955).

28. K. J. Vetter, *Electrochemical Kinetics,* Academic Press, New York pp. 671-674 (1967).

Appendix A. Summary of Cell Performance

In this appendix, cell performance data are presented for Li-Al/FeS multiplate cells fabricated by Eagle-Picher Industries for the Mark IA program, Li-Al/FeS bicells fabricated by Gould Inc., Li-Si/FeS bicells fabricated by Rockwell International, and Li-Al/FeS bicells fabricated by ANL. These cells were tested either at ANL or the contractors' facilities.

Appendix A-1. Performance Data on Eagle-Picher Li-Al/FeS Multiplate Cells

Cell Description[a]	Maximum Performance @ Indicated Rate		Rates, hrs		Initial Eff., %		Life Characteristics						Remarks
									% Decline in				
	A-hr	W-hr	Disch.	Charge	A-hr	W-hr	Days[b]	Cycles[b]	Capacity	Energy	A-hr Eff.	W-hr Eff.	
EPMP-7-021, Li-Al/FeS-Cu_2S, 400 A-hr, 3.7 kg	328	373	4	8	99	80	35	65	9	9	3	3	Cell design: 15 wt % Cu_2S added to positive electrode, and screen retainer only. Testing terminated to make room for another cell.
EPMP-7-022, Li-Al/FeS-Cu_2S, 398 A-hr, 3.7 kg	316	358	4	8	97	77	40	86	28	27	0	0	Cell design: 20 wt % Cu_2S added to positive electrode and Y_2O_3 felt retainer on positive. Terminated.
EPMP-7-023, Li-Al/FeS-Cu_2S, 398 A-hr, 3.5 kg	311	324	4	8	98	67	35	72	21	12	0	0	Cell design similar to that of -022. Terminated.
EPMP-7-024, Li-Al/FeS-Cu_2S, 405 A-hr	328	386	4	8	>99	>83	23	33	21	23	53	53	Cell design: 15 wt % Cu_2S in positive electrode, Y_2O_3 felt retainer on positive. Terminated.
EPMP-7-027, Li-Al/FeS-Cu_2S, 405 A-hr, 3.69 kg	341	381	4	8	>99	77	42	87	58	61	72	74	Cell design: 15 % Cu_2S and nickel positive current collector and rod. Terminated.
EPMP-7-028, Li-Al/FeS-Cu_2S, 405 A-hr, 3.64 kg	329	374	4	8	>97	>73	47	78	20	23	10	11	Cell design: 15 wt % Cu_2S in positive electrode, Y_2O_3 felt retainer on positive. Terminated.
EPMP-7-029, Li-Al/FeS-Cu_2S, 405 A-hr, 3.62 kg	311	355	4	8	>99	78	>112	>230	(30)	(31)	(28)	(29)	Cell design: Fe-ribbon positive current collector and rod. Study of cell reversal.

(Contd)

Appendix A-1. Performance Data on Eagle-Picher Li-Al/FeS Multiplate Cells

Cell Description[a]	Maximum Performance @ Indicated Rate		Rates, hrs		Initial Eff., %		Life Characteristics						Remarks
									% Decline in				
	A-hr	W-hr	Disch.	Charge	A-hr	W-hr	Days[b]	Cycles[b]	Capacity	Energy	A-hr Eff.	W-hr Eff.	
EPMP-7-030, Li-Al/FeS-Cu_2S, 405 A-hr, 373 kg	340	396	4	8	>99	>82	36	59	16	15	0	0	Cell design: 15 wt % Cu_2S in positive, Y_2O_3 felt retainer on positive and negative. Terminated to run another cell.
EPMP-7-031, Li-Al/FeS-Cu_2S, 402 A-hr, 3.85 kg	325	371	4	8	>99	80	99	186	21	21	3	4	Cell design: LiCl-rich electrolyte, Y_2O_3 felt retainer on positive and negative. Tested at 470°C. Terminated.
EPMP-7-032, Li-Al/FeS, 402 A-hr, 3.94 kg	358	405	4	8	>98	>77	35	60	20	21	13	14	Cell design: LiCl-rich electrolyte, Y_2O_3 felt retainer on both faces. Terminated.
EPMP-7-033, Li-Al/FeS-Cu_2S, 402 A-hr, 3.25 kg	322	393	8	8	>98	81	81	145	13	13	10	15	Cell design similar to -031. Testing terminated in discharged condition.
EPMP-7-035, Li-Al/FeS, 402 A-hr, 3.96 kg	333	385	4	8	>98	>79	52	102	9	9	5	5	Cell design: LiCl-rich electrolyte, Y_2O_3 felt on both faces, nickel-honeycomb current collector (instead of usual iron). Testing terminated for post-test analysis.
EPMP-7-036, Li-Al/FeS, 402 A-hr, 3.92 kg	343	379	4	8	>98	>74	31	78	9	7	7	5	Cell design similar to -035. Terminated.
EPMP-7-038, Li-Al/FeS-Cu_2S, 436 A-hr, 3.87 kg	364	417	4	8	99	79	11	21	0	0	0	0	Cell design: 15 wt % Cu_2S in positive electrode and screen particle retainer. Terminated due to poor performance.

(Contd)

Appendix A-1. Performance Data on Eagle-Picher Li-Al/FeS Multiplate Cells

Cell Description[a]	Maximum Performance @ Indicated Rate		Rates, hrs		Initial Eff., %		Life Characteristics						Remarks
									% Decline in				
	A-hr	W-hr	Disch.	Charge	A-hr	W-hr	Days[b]	Cycles[b]	Capacity	Energy	A-hr Eff.	W-hr Eff.	
EPMP-7-041A, Li-Al/FeS-Cu_2S, 436 A-hr, 3.3 kg	334	388	4	8	99	80	34	58	29	30	13	21	Similar to -038. Terminated.
EPMP-7-043, Li-Al/FeS-Cu_2S, 409 A-hr, 3.8 kg	339	391	4	8	99	80	38	76	44	47	6	13	Cell design: 15 wt % Cu_2S in positive electrode and Y_2O_3-felt retainer on positive face. Terminated.
EPMP-7-044, Li-Al/FeS-Cu_2S, 409 A-hr, 3.9 kg	343	392	4	8	>99	78	21	37	21	23	0	1	Similar to -043. Terminated.
EPMP-7-045, Li-Al/FeS-Cu_2S, 409 A-hr, 3.8 kg	351	403	4	8	99	79	39	62	10	11	3	4	Tested at 470°C. Terminated.
EPMP-7-046, Li-Al/FeS-Cu_2S, 409 A-hr, 3.8 kg	335	383	4	8	99	79	118	203	24	25	3	4	Similar to -043. Terminated.
EPMP-7-047, Li-Al/FeS-Cu_2S, 409 A-hr, 3.8 kg	341	401	4	8	>99	82	16	26	7	6	1	2	Similar to -043. Terminated.
EPMP-7-050, Li-Al/FeS-Cu_2S, 408 A-hr, 3.8 kg	307	353	4	8	98	78	28	53	24	26	30	31	Cell design: 20 wt % Cu_2S in positive electrode and Y_2O_3 felt on positive face. Terminated because cell leaked.
EPMP-7-053, Li-Al/FeS-Cu_2S, 408 A-hr, 3.9 kg	330	401	8	8	>99	84	12	17	42	46	58	60	Similar to -050. Terminated due to poor efficiency.

(Contd)

Appendix A-1. Performance Data on Eagle-Picher Li-Al/FeS Multiplate Cells

Cell Description[a]	Maximum Performance @ Indicated Rate		Rates, hrs		Initial Eff., %		Life Characteristics						Remarks
									% Decline in				
	A-hr	W-hr	Disch.	Charge	A-hr	W-hr	Days[b]	Cycles[b]	Capacity	Energy	A-hr Eff.	W-hr Eff.	
EPMP-7-054, Li-Al/FeS-Cu S, 408 A-hr, 3.9 kg	334	386	4	8	>99	81	72	129	73	75	61	65	Terminated due to poor efficiency.
EPMP-7-055, Li-Al/FeS, 402 A-hr, 3.9 kg	325	393	4	8	99	82	>144	>302	15	24	5	10	Cell has LiCl-rich electrolyte.
EPMP-7-056, Li-Al/FeS, 402 A-hr, 3.71 kg	284	320	5	8	>99	79	78	179	42	43	0	3	Cell used LiCl-rich electrolyte. Terminated.
EPMP-7-057, Li-Al/FeS, 402 A-hr, 3.72 kg	336	380	4	8	>99	80	79	156	20	21	0	4	Cell used LiCl-rich electrolyte. Terminated.
EPMP-7-058, Li-Al/FeS, 402 A-hr	352	404	4	8	>99	81	c	c	c	c	c	c	Cell used LiCl-rich electrolyte. Testing at 470°C.
EPMP-7-059, Li-Al/FeS, 403 A-hr, 3.8 kg	322	390	4	8	98	82	28	50	4	7	14	15	Similar to -055. Terminated.
EPMP-7-060, Li-Al/FeS, 403 A-hr, 3.8 kg	240	271	4	8	99	76	96	172	(6)	(7)	(44)	(43)	Similar to -055. Study of cell reversal. Terminated for examination.
EPMP-7-061, Li-Al/FeS-Cu_2S, 409 A-hr, 3.8 kg	341	394	4	8	>99	81	97	210	72	73	2	11	Eutectic electrolyte prepared by Eagle-Picher. Similar to -045. Terminated.
EPMP-7-062, Li-Al/FeS-Cu_2S, 409 A-hr, 3.8 kg	348	406	4	8	>99	81	91	191	32	32	4	6	Similar to -045. Terminated.
EPMP-7-063, Li-Al/FeS-Cu_2S, 409 A-hr, 3.8 kg	354	410	4	8	>99	81	67	176	27	28	5	8	Similar to -045. Terminated.

(Contd)

Appendix A-1. Performance Data on Eagle-Picher Li-Al/FeS Multiplate Cells

Cell Description[a]	Maximum Performance @ Indicated Rate, A-hr	Maximum Performance @ Indicated Rate, W-hr	Rates, hrs: Disch.	Rates, hrs: Charge	Initial Eff., %: A-hr	Initial Eff., %: W-hr	Life Characteristics: Days[b]	Life Characteristics: Cycles[b]	% Decline in: Capacity	% Decline in: Energy	% Decline in: A-hr Eff.	% Decline in: W-hr Eff.	Remarks
EPMP-7-065, Li-Al/FeS-Cu_2S, 409 A-hr, 3.8 kg	345	397	4	8	>99	80	48	141	58	56	0	1	Similar to -045. Terminated for safety-test use.
EPMP-7-066, Li-Al/FeS-Cu_2S, 409 A-hr, 3.8 kg	343	394	4	8	>99	79	27	43	38	40	61	63	Similar to -045. Testing terminated--poor coulombic efficiency.
EPMP-7-067, Li-Al/FeS-Cu_2S, 409 A-hr, 3.8 kg	302	352	4	8	99	82	42	70	14	13	41	40	Filled with LiCl-rich (410°C liquidus) electrolyte. Terminated.
EPMP-7-068, Li-Al/FeS-Cu_2S, 409 A-hr, 3.8 kg	313	376	4	8	98	81	34	69	31	30	39	37	Similar to -067. Terminated.
EPMP-7-069, Li-Al/FeS, 409 A-hr, 3.8 kg	329	384	4	8	98	81	5	4	-	-	-	-	Filled with LiCl-rich electrolyte. Cell shorted.
EPMP-7-070, Li-Al/FeS-Cu_2S, 387 A-hr, 3.7 kg	303	342	4	8	>99	77	>22	>41	9	8	8	8	Design as -067; used for equalization studies.
EPMP-7-071, Li-Al/FeS-Cu_2S, 387 A-hr, 3.7 kg	303	341	4	8	99	75	67	118	16	14	58	47	Filled with LiCl-rich (410°C liquidus) electrolyte. Used for J-227 driving profile test. Terminated.
EPMP-7-072, Li-Al/FeS-Cu_2S, 387 A-hr, 3.7 kg	327	377	4	8	98	80	67	128	34	34	4	8	15 wt % Cu S added to positive electrode. Terminated for safety test use.
EPMP-7-073, Li-Al/FeS-Cu_2S, 386 A-hr, 3.7 kg	315	368	4.5	8	>99	80	63	132	23	24	1	1	Design similar to -072. Terminated for safety test use.

(Contd)

Appendix A-1. Performance Data on Eagle-Picher Li-Al/FeS Multiplate Cells

Cell Description[a]	Maximum Performance @ Indicated Rate		Rates, hrs		Initial Eff., %		Life Characteristics						Remarks
									% Decline in				
	A-hr	W-hr	Disch.	Charge	A-hr	W-hr	Days[b]	Cycles[b]	Capacity	Energy	A-hr Eff.	W-hr Eff.	
EPMP-7-074, Li-Al/FeS-Cu_2S, 387 A-hr, 3.7 kg	329	381	4	8	98	79	c	112	33	39	0	0	Design similar to -072. Terminated
EPMP-7-075, Li-Al/FeS-Cu_2S, 387 A-hr, 3.7 kg	332	386	4	8	98	79	80	167	54	56	64	66	Design as -072. Testing terminated.
EPMP-076, Li-Al/FeS-Cu_2S, 387 A-hr, 3.6 kg	315	356	4	8	>99	77	55	68	24	30	0	1	Design as -072. Terminated.
EPMP-7-077, Li-Al/FeS-Cu_2S, 387 A-hr, 3.7 kg	321	368	4	8	>99	80	c	137	27	26	0	2	Design as -072. Terminated.
EPMP-7-078, Li-Al/FeS-Cu_2S, 387 A-hr, 3.6 kg	306	352	4	8	97	78	c	126	c	c	c	c	Design as -072. Terminated.
EPMP-7-079, Li-Al/FeS-Cu_2S, 387 A-hr, 3.7 kg	292	338	4	8	99	80	c	90	13	13	1	2	Design as -072. Terminated
EPMP-7-080, Li-Al/FeS-Cu_2S, 387 A-hr, 3.7 kg	350	402	4	8	98	79	71	132	29	31	12	15	Design as -072. Testing terminated.
EPMP-7-081, Li-Al/FeS-Cu_2S, 387 A-hr, 3.7 kg	327	376	4	8	99	80	c	c	c	c	c	c	Design as -072. Testing @ 165°C.
EPMP-7-082, Li-Al/FeS-Cu_2S, 387 A-hr, 3.7 kg	278	331	4	8	99	83	7	15	0	0	0	2	Design as -072. Restraint plate bolts broke and test terminated.
EPMP-7-083, Li-Al/FeS-Cu_2S, 387 A-hr, 3.8 kg	320	372	4	8	98	79	c	124	23	24	0	0	Design as -072. Terminated.

(Contd)

Appendix A-1. Performance Data on Eagle-Picher Li-Al/FeS Multiplate Cells

Cell Description[a]	Maximum Performance @ Indicated Rate		Rates, hrs		Initial Eff., %		Life Characteristics						Remarks
									% Decline in				
	A-hr	W-hr	Disch.	Charge	A-hr	W-hr	Days[b]	Cycles[b]	Capacity	Energy	A-hr Eff.	W-hr Eff.	
EPMP-7-084, Li-Al/FeS-Cu_2S, 387 A-hr, 3.7 kg	285	329		8	>99	80	c	103	25	25	2	3	Design as -072. Terminated.
EPMP-7-085, Li-Al/FeS-Cu_2S, 387 A-hr, 3.7 kg	321	373	4	8	98	79	47	96	27	28	0	1	Design as -072. Terminated.
EPMP-7-086, Li-Al/FeS-Cu_2S, 387 A-hr, 3.8 kg	321	370	4	8	>99	80	78	161	21	21	0	2	Design as -072. Terminated.
EPMP-7-087, Li-Al/FeS-Cu_2S, 387 A-hr, 3.7 kg	333	383	4	8	>99	80	>67	>129	21	21	0	1	Design as -072. Now testing at 4.7-hr rate.
EPMP-7-088, Li-Al/FeS-Cu_2S, 387 A-hr, 3.7 kg	283	330	4	8	97	77	62	141	17	17	0	0	Design as -072. Terminated.
EPMP-7-089, Li-Al/FeS-Cu_2S, 387 A-hr, 3.7 kg	332	395	5	8	>99	83	>100	>232	34	38	2	8	Design as -072. Now testing @ 5-hr rate and 470°C.
EPMP-7-090, Li-Al/FeS-Cu_2S, 387 A-hr,	335	398	5.5	8	>99	83	c	c	c	c	c	c	Design as -072. Terminated.
EPMP-7-091, Li-Al/FeS-Cu_2S, 387 A-hr, 3.8 kg	323	376	4	8	>99	80	>78	>181	21	23	2	9	Design as -072; used for power pulse tests.
EPMP-7-092, Li-Al/FeS-Cu_2S, 387 A-hr, 3.8 kg	348	418	5.5	8	>99	83	82	159	19	22	0	2	Design as -072. Terminated.
EPMP-7-093, Li-Al/FeS-Cu_2S, 387 A-hr, 3.7 kg	348	416	5.5	8	99	83	70	120	57	63	0	15	Design as -072. Testing terminated.

(Contd)

Appendix A-1. Performance Data on Eagle-Picher Li-Al/FeS Multiplate Cells

Cell Description[a]	Maximum Performance @ Indicated Rate		Rates, hrs		Initial Eff., %		Life Characteristics						Remarks
									% Decline in				
	A-hr	W-hr	Disch.	Charge	A-hr	W-hr	Days[b]	Cycles[b]	Capacity	Energy	A-hr Eff.	W-hr Eff.	
EPMP-7-094, Li-Al/FeS-Cu_2S, 387 A-hr, 3.8 kg	268	302	4	8	98	78	40	74	18	25	62	6	Design as -072. Terminated due to short circuit.
EPMP-7-095, Li-Al/FeS-Cu_2S, 387 A-hr, 3.7 kg	325	379	4.5	8	>99	80	97	238	55	57	51	51	Design as -072. Terminated.
EPMP-7-096, Li-Al/FeS-Cu_2S, 387 A-hr, 3.7 kg	331	392	4.5	8	>99	80	>109	>224	20	23	1	4	Design as -072.
EPMP-7-103, Li-Al/FeS-Cu_2S, 387 A-hr, 3.8 kg	329	376	4	8	99	79	19	37	22	22	0	0	Terminated for safety test use.
EPMP-7-113, Li-Al/FeS-Cu_2S, 409 A-hr, 3.8 kg	304	352	4	8	>99	80	41	86	6	8	0	1	Design as -072. Terminated due to short circuit.
EPMP-7-114, Li-Al/FeS-Cu_2S, 387 A-hr, 3.7 kg	318	370	4.4	8	97	79	48	99	21	23	0	1	Design as -072. Terminated.

[a]Cell description includes cell number, composition of negative and positive electrodes, theoretical capacity, and cell weight.

[b]The "greater than" symbols denote continuing operation.

[c]Data not available.

Appendix A-2. Performance Data on Gould Li-Al/FeS Cells

Cell Description[a]	Pos. Electrode Additives[b]	Electrolyte, w/o LiCl	Cell Operat. Resist., mΩ		Frozen Resist., Ω	Specific Energy, W-hr/kg		Cycle Life	
			t = 0	t = 15 sec		20 mA/cm^2	60 mA/cm^2	Cycles	Hours
X-40, 164.3 A-hr, 2.376 kg	100 w/o Fe 3 v/o C 1 v/o Co 6.7 w/o Co	49.3	2.45	3.00	0.4	81.3	69.8	20	550
X-41, 165.47 A-hr, 2.123 kg	50 w/o Fe 3 v/o C 1 v/o Co	50.0	3.12	4.58	3.9×10^5	93.3	61.4	11.5	452
X-42, 178.8 A-hr, 2.071 kg	25 w/o Fe 3 v/o C 1 v/o Co	50.0	-	-	2.4	-	-	0.5	90
X-43, 165.99 A-hr, 2.114 kg	as X-41	52.0	2.57	3.60	6×10^4	92.2	70.7	11.5	451
X-43A, 167.20 A-hr, 2.04 kg	as X-41	52.0	4.22	5.59	5.3×10^4	70.9	44.0	13.5	388
X-43B, 164.675 A-hr, 2.11 kg	as X-41	52.0	2.6	4.1	-	95.6	71.2	14	644
X-44, 168.33 A-hr, 2.285 kg	as X-41	53.8	3.16	4.10	2.3×10^5	84.2	58.1	36.5	700
X-45, 169.49 A-hr, 2.148 kg	as X-41	48.0	2.82	3.50	9.5×10^3	88.7	61.4	123.5	1630
X-47, 169.10 A-hr, 2.388 kg	25 w/o Fe 3 v/o C 1 v/o Co	52.0	2.93	3.57	7.3×10^5	83.5	59.0	13.5	428
X-48, 173.95 A-hr, 2.33 kg	50 w/o Fe 3 v/o C 3 v/o Mo	52.0	2.99	3.63	6.9	86.8	62.7	11.5	420

(Contd)

Appendix A-2. Performance Data on Gould Li-Al/FeS Cells

Cell Description[a]	Pos. Electrode Additives[b]	Electrolyte, w/o LiCl	Cell Operat. Resist., mΩ t = 0	Cell Operat. Resist., mΩ t = 15 sec	Frozen Resist., Ω	Specific Energy, W-hr/kg 20 mA/cm^2	Specific Energy, W-hr/kg 60 mA/cm^2	Cycle Life Cycles	Cycle Life Hours
X-49, 175.77 A-hr, 2.35 kg	50 w/o Fe 3 v/o C 3 v/o Cr	52.0	3.20	4.37	1.3×10^4	60.7	47.2	11.5	420
X-50, 179.01 A-hr, 2.35 kg	50 w/o Fe 3 v/o C 3 v/o V	52.0	3.04	3.57	74.8	78.8	58.9	11.5	426
X-53,[c] 211.73 A-hr, 2.30 kg	25 w/o Fe 3 v/o C 1 v/o Co	52.0	3.00	3.83	7.6	99.4	58.0	15	547
X-54,[c] 184.04 A-hr, 2.33 kg	25 w/o Fe 3 v/o C 1 v/o Co	52.0	3.65	4.21	1.4×10^7	89.0	58.4	11	431
X-55, 176.86 A-hr, 2.46 kg	100 w/o Fe 3 v/o Zr 1 v/o C	52.0	3.62	4.72	-	74.1	60.0	13.5	626
X-56, 179.72 A-hr, 2.47 kg	50 w/o Fe 3 v/o C 1 v/o Co 2 v/o ZrO_2	52.0	-	-	0.0	-	-	0.5	9
X-56A, 176.266 A-hr, 2.27 kg	100 w/o Fe 3 v/o C 1 v/o Co 2 v/o ZrO_2	52.0	3.51	4.43	-	93.6	-	>4.5	>25
X-57, 190.4 A-hr, 2.46 kg	100 w/o Fe 3.4 v/o C 1 v/o Co 2 v/o ZrO_2	52.0	4.26	5.52	-	80.7	67.1	14.5	623

(Contd)

Appendix A-2. Performance Data on Gould Li-Al/FeS Cells

Cell Description[a]	Pos. Electrode Additives[b]	Electrolyte, w/o LiCl	Cell Operat. Resist., mΩ		Frozen Resist., Ω	Specific Energy, W-hr/kg		Cycle Life	
			t = 0	t = 15 sec		20 mA/cm²	60 mA/cm²	Cycles	Hours
X-64, 186.8 A-hr 2.11 kg	100 w/o Fe 3.4 w/o C 1 w/o Co	52.0	-	-	0	-	-	-	140

[a] Cell description includes cell number, composition of negative and positive electrodes, theoretical capacity, and cell weights.

[b] Amounts are percent of active material (no salt) except for the 6.7 w/o Co in X-40 which is the percent of iron.

[c] Assembled half-charged.

Appendix A-3. Performance Data on Rockwell International Li-Si/FeS Bicells

Cell No.	Design Characteristics			Coulombic Eff.,[a] %	Pos. Utiliz.,[b] %	Lifetime		Comments
	Pos. Elect.	Sep.	Electrolyte			Cycles	Days	
1A to 6A	Dual-face	Fine AlN	55 wt % LiCl	-	-	0	0	Four cells failed during startup; two cut up for inspection.
7A	Dual-Face	Fine AlN, Y_2O_3 cloth on neg.	55 wt % LiCl	89	-	28	10	Short circuit, tested at ANL.
8A	Dual-face	Coarse AlN, Y_2O_3 cloth on neg. and ZrO_2 on pos.	55 wt % LiCl	93(75)	40-55	281	164	Subjected to six thermal cycles without apparent effect.
9A-1	Dual-face	Coarse AlN, ZrO_2 over pos.	55 wt % LiCl	91(180)	40-50	255	121	Damaged by overcharge.
9A-2	Dual-face	Coarse AlN, ZrO_2 over pos.	50 wt % LiCl	95(187)	30-35	284	136	None.
9A-3[c]	Dual-face	Coarse AlN, ZrO_2 over pos.	50 wt % LiCl	98(92)	30-35	92	36	Voluntarily terminated.
10A[d]	Dual-face	Lithium silicate phosphate	55 wt % LiCl	90(52)	20-25	73	27	Failure in positive electrode.
11A	Dual-face	BN felt	55 wt % LiCl	-	-	-	-	Short circuit found in electrolyte.
12A	Dual-face	Coarse AlN, ZrO_2 on pos.	55 wt % LiCl	90(103)	50-55	149	45	Assembled partially charged. Nickel powder added to positive.

(Contd)

Appendix A-3. Performance Data on Rockwell International Li-Si/FeS Bicells

Cell No.	Design Characteristics			Coulombic Eff.,[a] %	Pos. Utiliz.,[b] %	Lifetime		Comments
	Pos. Elect.	Sep.	Electrolyte			Cycles	Days	
1B	Split-rib	Lithium silicate phosphate	55 wt % LiCl	98(91)	40-45	120	53	Assembled partially charged. Heavy central copper current collector. Short circuit in ZrO_2 cloth.
2B	Split-rib	Lithium silicate phosphate	55 wt % LiCl	98(118)	15-25	208	50	Assembled partially charged. Forty-three percent excess Fe added to positive. Voluntarily terminated.

[a] Numbers in parentheses are cycles at which coulombic efficiency began to decline at accelerated rate.

[b] Approximate range at 465-475°C.

[c] Tested at ANL and returned to RI; data for RI testing only.

[d] Rebuilt after initial failure; data shown for subsequent test only.

Appendix A-4. Performance Data on ANL Li-Al/FeS Cells

Cell Description[a]	Maximum Performance @ Indicated Rate[b] A-hr	W-hr	Rates, hrs Disch.	Charge	Initial Eff.,[c] % A-hr	W-hr	Life Characteristics Days[d]	Cycles[d]	% Decline in Capacity	Energy	A-hr Eff.	W-hr Eff.	Remarks
R-36, Li-Al/NiS-CoS_2, U, 180/150, 13.3 x 15.2 x 3.5 cm, 1.8 kg	100 70	146 84	13.5 3.0	13.5 8.0	99	79	>444	>1084	33	30	20	18	Carbon fiber added to NiS positive electrode.
R-41, Li-Al/FeS-Cu_2S, U, 180/103, 13.3 x 15.2 x 3.5 cm, 1.7 kg	76	100	3.3	8.8	>99	83	180	351	2	13	2	1.2	BN felt separator treated with $LiAlCl_4$. Terminated.
R-42, Li-Al/FeS-Cu_2S, U, 160/113, 13.3 x 15.2 x 3.5 cm, 1.7 kg	61	75	3.0	6.0	60	42	103	253	21	23.5	35	46	Similar to R-41 but with $LiAlCl_4$ in positive electrode. Terminated.
R-43, Li-Al/FeS, U, 150/134, 13.3 x 15.2 x 3.5 cm, 1.8 kg	83	96	5	0	100	83	127	240	14.6	32.3	20	22	Design: BN felt separator with $LiAlCl_4$, LiCl-rich electrolyte, high-temperature carbon added. Terminated.
R-44, Li-Al/FeS, U, 180/133, 13.3 x 15.2 x 3.5 cm, 1.8 kg	80	98	4	10	99	82	>210	>326	0	0	0	0	This cell has BN felt separator with $LiAlCl_4$, LiCl-rich electrolyte, high-temperature carbon added to positive, and iron current collector.
R-46, Li-Al/Fe, U, 180/133, 13.3 x 15.2 x 3.5 cm, 1.8 kg	56.5	65.0	7.2	7.25	98.5	79.5	70	121	20	18	11	7	This cell has BN felt separator with $LiAlCl_4$, high-temperature carbon, LiCl-rich electrolyte, and Fe rod current collector with no sheet. Terminated.
R-47, Li-Al/FeS, U, 210/144, 13.3 x 15.2 x 3.5 cm, 1.78 kg	90.3	108.4	4.5	14.5	99.8	84.5	>102	>147	9	8	0	0	This cell has BN felt separator with $LiAlCl_4$, high-temperature carbon, LiCl-rich electrolyte, and Ni current collector.
R-48, Li-Al/FeS, U, 210/144, 13.3 x 15.2 x 3.5 cm, 1.78 kg	80	102	4.0	10.8	100	87.5	>86	>112	0	2	0	3	Similar to R-47, but with all iron current collector.

(Contd)

Appendix A-4. Performance Data on ANL Li-Al/FeS Cells

Cell Description[a]	Maximum Performance @ Indicated Rate[b] A-hr	W-hr	Rates, hrs Disch.	Charge	Initial Eff.,[c] % A-hr	W-hr	Life Characteristics Days[d]	Cycles[d]	% Decline in Capacity	Energy	A-hr Eff.	W-hr Eff.	Remarks
R-49, Li-Al/FeS, U, 185/144, 13.3 x 15.2 x 3.18 cm, 1.68 kg	84	102	4.2	11.2	99.9	84.9	>44	>67	1	2	0	0	Similar to R-48, with only one electrode frame around positive electrode.
R-50, LiAl/FeS, U, 141/103, 13.3 x 15.2 x 2.7 cm, 1.40 kg	63	78	3	10	99	78	>17	>27	0	0	0	0	Similar to R-47, but thinner positive electrode.
M-8, Li-Al/FeS, C 155/113, 13.3 x 13.5 x 2.8 cm, 1.55 kg	83 74	101 88	3 3.8	8.5 7.5	97	84	197	347	9	10	0	0	Design: BN felt separator/ retainer, LiCl-rich electrolyte (Anderson) used throughout, positive loading of 1.41 A-hr/ cm^3. 3.5 mΩ cell resistance. Terminated.
M-10, Li-Al/FeS, C, 155/115, 13.3 x 13.5 x 2.8 cm, 1.56 kg	56 43	65 50	2.8 1.4	5.5 4.5	99 99	83 83	100	300	18	15	9	0	Design: BN felt separator/ retainer, LiCl-KCl eutectic, positive loading of 1.40 A-hr/cm^3. Terminated.
M-11, Li-Al/FeS, C, 174/132, 13.3 x 13.5 x 2.8 cm, 1.52 kg	71 60	80 67	3.5 2	7 6	99 99	79 77	130	365	18	15	0	0	Design: BN felt separator/ retainer, LiCl-rich electrolyte (Anderson), positive loading of 1.61 A-hr/cm^3. 3.5 mΩ cell resistance. Terminated.
M-12, Li-Al/FeS-Cu_2S, C, 155/121, 13.3 x 13.5 x 2.8 cm, 1.55 kg	67	80	3.3	6.8	98	83.6	83	202	44	41	6	6	Design: BN felt separator/ retainer, LiCl-KCl eutectic, positive loading of 1.40 A-hr/ cm^3. 3.5 mΩ cell resistance. Terminated.
M-MP-3, Li-Al/FeS, C, 420/346, 13.9 x 14.6 x 7.9 cm, 4.68 kg	265 239	327 285	8.8 4	9 8	99 98	87 86	48	85	2	2.5	0	0	This cell had cold pressed electrodes (three positive, four negative); LiCl-rich electrolyte; BN-felt separators. Cell resistance at 50% discharge is 1.14 mΩ.

(Contd)

Appendix A-4. Performance Data on ANL Li-Al/FeS Cells

Cell Description[a]	Maximum Performance @ Indicated Rate[b] A-hr	W-hr	Rates, hrs Disch.	Charge	Initial Eff.,[c] % A-hr	W-hr	Life Characteristics Days[d]	Cycles[d]	% Decline in Capacity	Energy	A-hr Eff.	W-hr Eff.	Remarks
KK-15, Li-Al/FeS, C, 150/133, 13.3 x 13.3 x 2.8 cm, 1.54 kg	101 87 77.5	128 108 93.5	10 4.5 2.5	10 8 7	99	89	143	245	5	5	0	0	This cell has carbon-bonded FeS electrode (1.4 A-hr/cm^3), hot-pressed LiAl electrodes, LiCl-rich electrolyte, BN-felt separator. Resistance is 2.8 mΩ. Terminated after accidental overcharge.
K-MP-1, Li-Al/FeS, C, 420/333, 13.3 x 13.3 x 6.9 cm, 396 kg	276 263 246	344 313 279	9 4.3 2.7	9 8 7	95	82	60	42	5	5	0	0	Multiplate cell: BN-felt separator, no electrode frames, carbon-bonded positive electrode (1.4 A-hr/cc) and pressed negative. Achieved a very high specific power - 101 W/kg at 50% discharge. Feedthrough short-circuited.
PW-9, Li-Al/FeS, 1/2 C, 216/144, 13.65 x 13.02 x 4.2 cm, 1.94 kg	94 69 55.8	114 82.6 65.84	18.4 6.9 3.7	18.4 9.3 7.4	99	82	>451	>793	0	0	0	2.3	Design: hot pressed MgO powder separator, screen and frame on negative electrodes. M-series cell design. Resistance 8-10 mΩ. Addition of electrolyte returned performance to initial rate.
PW-12, Li-Al/FeS, 1/2 C, 190/134, 14.53 x 13.97 x 2.69, 1.6 kg	65	79.3	6.5	8.5	97	87	78	103	22	19	34	39	Hot-pressed MgO powder separator (2-cm thick, 70 wt % salt). Resistance is 4.6-6.4 mΩ.
PW-13, Li-Al/FeS, 1/2 C, 175/144, 14.63 x 13.97 x 2.6 cm, 1.7 kg	83	96.6	11	11	99	80	125	188	47	48	28	29	MgO powder separator. Cell temporarily short circuited in early stages, but was repaired. Cell terminated.

(Contd)

Appendix A-4. Performance Data on ANL Li-Al/FeS Cells

Cell Description[a]	Maximum Performance @ Indicated Rate[b] A-hr	W-hr	Rates, hrs Disch.	Charge	Initial Eff.,[c] % A-hr	W-hr	Life Characteristics Days[d]	Cycles[d]	% Decline in Capacity	Energy	A-hr Eff.	W-hr Eff.	Remarks
PW-16, Li-Al/FeS, 1/2 C, 173/131, 14.63 x 13.69 x 2.69, 1.8 kg	106 65 83	129 71 96	12 2.1 4.2	14 8.7 11	99	78	152	330	22	22.4	0	0	Design: vibratory loaded MgO powder separator, LiCl-rich electrolyte (Anderson). Positive loading of 1.1 A-hr/cm^3. Internal resistance is 5 mΩ. Leak has developed in cell container. Voluntarily terminated.
MP-PW-1, Li-Al/FeS, 1/2 C, 530.1/388.2, 8.26 x 13.97 x 17.15, ~6.0 kg	301.5	374.1	15	15	96	82.3	>5	>4	0	0	0	0	Multiplate cell with vibratory loaded MgO and LiCl-rich electrolyte. Same positive loading density as PW-16. Internal resistance is 2.2 to 2.5 mΩ.

[a] The letters U and C are used to indicate uncharged and charged cells, respectively. The capacity ratio is the number of ampere-hours in the negative electrode over the number of ampere-hours in the positive electrode.

[b] Based on at least 5 cycles.

[c] Based on at least 10 cycles at the 5-hr discharge rate.

[d] The "greater than" symbols denote continuing operation.

[e] Percent declines from the maximum values at the 5-hr discharge, except where noted.

APPENDIX B. POST-TEST EXAMINATIONS OF CELLS

The results of the post-test examination of multiplate cells and bicells are given below.

Appendix B-1. Summary of Post-Test Examinations of Multiplate Cells

Cell Description[a]	Lifetime Cycles	Lifetime Days	Reason Terminated	Comments
EPMP-5-001, Li-Al/FeS, E	8	5	Equipment malfunction	Electrodes showed uniform thickness, no extrusion and no bulging of cell can. Separator showed considerable deficiency of electrolyte.
EPMP-5-003, Li-Al/FeS, E	39	60	End of test	Examination showed minor variations in electrode thickness, minor agglomeration of Li-Al in lower portion of negative electrodes, deficiency of electrolyte in separator. No extrusion of electrodes. Negative electrodes swelled by about 25% in thickness.
EPMP-5-005, Li-Al/FeS-Cu_2S, E	55	94	End of test	This cell showed a cold resistance of 0.3 mΩ, indicating a short circuit. Negative electrode thickness was non-uniform; negative electrodes swelled by 25-40% in thickness. Short circuit was attributed to the migration of Li-Al from the negative electrode and the deposition of copper and iron (from positive electrode) in the open interstices of the EN fabric separator. Separator was more completely filled with electrolyte; but not completely filled.
EPMP-5-009, Li-Al/FeS-Cu_2S, E	39	75	End of test	Cell resistance was 9 Ω (cold). Electrode thickness was uniform. Minor extrusion at top. Very minor agglomeration of Li-Al. Some unreacted Li-Al in outside electrodes. Negative electrodes showed 15-20% swelling in thickness.
EPMP-5-018, Li-Al/$CuFeS_2$-Fe, E	38	68	Declining A-hr efficiency	This cell showed a partial short circuit due to cracked lower insulator in feed-through. Major deficiency of electrolyte in negative electrodes and separators. Major agglomeration of LiAl in center of negative electrodes.
EPMP-7-022, Li-Al/FeS-Cu_2S, E	6	4	Short circuit	Multiple short circuits caused by ruptures in separator and screens, which in turn were caused by the electrodes being broken during cell assembly.
EPMP-7-026, Li-Al/FeS-Cu_2S, E	37	58	Short circuit	Short circuit caused by extrusion of positive electrode material through ruptures in screens and separators at bottom of cell. Cell thickness expanded by 20-25% (loose retainer plate bolts) and was refilled with electrolyte. Edge of cell showed bulging. Electrolyte filling of separators and electrodes was good. Little evidence of agglomeration in Li-Al.

(Contd)

Appendix B-1. Summary of Post-Test Examination of Multiplate Cells

Cell Description[a]	Lifetime Cycles	Lifetime Days	Reason Terminated	Comments
EPMP-7-030, Li-Al/FeS-Cu_2S, E	33	59	Short circuit	The feedthrough developed a short circuit on cycle 49, which was isolated and the cell was operated an additional 10 cycles. Short was in top of feedthrough and was caused by electrolyte from external source.
EPMP-7-032, Li-Al/FeS-Cu_2S, E	35	60	Short circuit	Short circuit caused by upward extrusion of one positive electrode, which ruptured screen and fabric and forced screen into contact with top cover plate. Negative-electrode thickness in center of cell was very non-uniform, with some areas showing 50-60% expansion. Some areas were slightly compressed. Extensive agglomeration of Li-Al was present in the negative electrode. Separator was deficient in electrolyte.
EPMP-7-034, Li-Al/FeS, LR	0	0	Short circuit	Short circuit developed during electrolyte filling, when 100 g of liquid $LiAlCl_4$ was added to cell followed by LiCl-rich electrolyte. Short was apparently caused by metallic deposits (from the $LiAlCl_4$) within the separator. The separator was completely filled with electrolyte. Results indicate that $LiAlCl_4$ should not be added as a liquid and that amount should be minimized.
EPMP-7-035, Li-Al/FeS, LR	55	101	Declining A-hr efficiency	Short circuit caused by extrusion of positive electrode material through rupture in screen and separator at bottom of cell. Edge of cell bulged. Minor agglomeration of Li-Al. Electrode thickness was uniform and expanded by ∿25%. Deficiency of electrolyte in negative electrode and separator.
EPMP-7-036, Li-Al/FeS, LR	29	78	Declining A-hr efficiency	Cause of short circuit same as -035. Negative electrodes expanded ∿25%, and showed some non-uniformity and minor Li-Al agglomeration; edge of cell bulged.
EPMP-7-033, Li-Al/FeS, LR	81	145	Declining A-hr efficiency	Cause of short circuit same as -035. Minor agglomeration of Li-Al in negative electrode. Negative electrode showed both compression and expansion. Very non-uniform thickness in center of cell. Edges of cell can were severely bulged.
EPMP-7-048, Li-Al/FeS, E	0	0	Short circuit	Separators were pretreated with wetting agent, $LiAlCl_4$. The amount used was excessive. Short circuit was attributed to metallic deposits across the separator from the $LiAlCl_4$. Because of the nature of the fabric, the $LiAlCl_4$ was concentrated in these areas.

(Contd)

Appendix B-1. Summary of Post-Test Examination of Multiplate Cells

Cell Description[a]	Lifetime Cycles	Lifetime Days	Reason Terminated	Comments
EPMP-7-059, Li-Al/FeS, E	27	50	Declining A-hr efficiency	Cause of short circuit same as -035. Electrode thickness was very uniform. Considerable deficiency of electrolyte in separator and negative electrode. Original Li-Al particles in center of negative electrode (unreacted). Negative electrodes expanded 20-25%.
EPMP-7-068, Li-Al/FeS-Cu_2S, LR	36	69	Declining A-hr efficiency	The short circuit was between one pair of electrodes (a positive and the adjacent negative) about one inch from the bottom. The retainer screen of the positive electrode was ruptured in this area and it appears that a broken wire penetrated the separator and contacted the negative electrode. Electrode thickness was very uniform. Minor agglomeration of Li-Al. The two center negative electrodes had extruded through ruptures in the retainer screens at the bottom. Deficiency of electrolyte in separator. 20-30% expansion in thickness of negative electrodes.
EPMP-7-069, Li-Al/FeS-Cu_2S, E	~5	4	Short circuit	The electrical feedthrough short circuited. The short was caused by electrolyte corrosion at the top of the upper insulator. The electrolyte was from an external source and did not leak through the feedthrough.
EPMP-7-071, Li-Al/FeS-Cu_2S, LR	118	67	Short circuit	Short circuit was caused by rupture in separator near the edge in the center positive electrode; Li-Al agglomeration was observed in the center portion of the negative electrodes. Areas of excessive corrosion of the current collectors were observed, which indicate higher temperature operation (>450°C) or some overcharging. Negative electrode expansion was 30%.
EPMP-7-094, Li-Al/FeS-Cu_2S, E	74	48	Short circuit	Short circuit was caused by a metallic bridge across insulator of the feed-through; this problem was brought about by corrosion due to the accidental spill of electrolyte in this area. The BN powder seal in the feedthrough was effective. Minor agglomeration observed in negative electrode. Inner negative electrodes showed 7% compression while outer negative electrodes showed 20% expansion. Positive electrodes showed 80% expansion. Cell was fully discharged.

(Contd)

Appendix B-1. Summary of Post-Test Examination of Multiplate Cells

Cell Description[a]	Lifetime Cycles	Lifetime Days	Reason Terminated	Comments
EPMP-7-164, Li-Al/FeS-Cu_2S, E	5	3	Poor coulombic efficiency	Poor coulombic efficiency was caused by a loop in the positive screen penetrating the separator at one edge, which resulted in a partial short circuit. Electrolyte filling was very good in the electrodes and fair in the separators.
EPMP-7-166, Li-Al/FeS-Cu_2S, E	-	-	Short circuit	Cell was accidentally overheated (>600°C). Short circuit caused by molten Li-Al penetrating the separator.
EPMP-7-287, Li-Al/FeS-Cu_2S, E	-	-	Short circuit	Short circuit was caused by accidental overcharge in electrolyte filling operation which resulted in metallic iron deposits across the separator.

[a]Cell description includes cell number, composition of negative and positive electrodes, and electrolyte composition (the symbols E and LR represent the eutectic and LiCl-rich electrolyte compositions, respectively).

Appendix B-2. Post-Test Examination of Bicells

Cell Description	Lifetime Cycles	Lifetime Days	Reason Terminated	Comments
G04-019A, Li-Al/FeS_2	18	20	Short circuit	Metallographic examination showed massive intrusions of positive electrode material into the BN fabric separator, and this appears to be the cause of the short circuit. Li_2S was deposited in separator. Positive electrode was deficient in electrolyte, and expanded by 60%.
EP-I8L-035, Li-Al/FeS_2-CoS_2	83	94	End of test	Cell was subjected to vibration testing. The microstructure of the positive and negative electrodes was the same as observed in non-vibrated cells, indicating that the vibration testing had no effect on electrode morphology. Li_2S was deposited in the separator. Negative electrode showed 40% expansion. Positive electrode showed 7% compression.
EP-I8H-036, Li-Al/FeS_2-CoS_2	104	106	Declining capacity	Cause of the declining capacity was not identified. Typical deposit of Li_2S was observed in the separator. Negative electrode showed 80% expansion. Positive electrode showed 8% expansion, 90 vol % active material (10 vol % electrolyte), and was about half discharged.
G-0080-9, Li-Al/FeS	2	0	Short circuit	This cell used a copper current collector in the positive electrode. The short circuit was caused by copper deposition across the separator between the positive bus bar (copper) and the housing bracket at the negative electrode potential. Corrosion of the copper current collector ranged from 270 to 566 mils/year penetration.
GX-45, Li-Al/FeS	51	113	Short circuit	Short circuit was caused by rupture in BN felt separator, which in turn was caused by the gross non-uniform expansion of the negative electrode and compression of the positive electrode in localized areas.
EP-I3B-2, Li-Al/FeS-Cu_2S	333	505	Short circuit	Short circuit was caused by the honeycomb current collector of the positive electrode cutting through the separator. Also, metallic copper was deposited within the separator. Negative electrode showed 40% expansion.
EP-I3B-1, Li-Al/FeS-Cu_2S	417	896	Short circuit	Short circuit was caused by the honeycomb current collector of the positive electrode cutting through the separator. Metallic copper was deposited within the separator. Positive electrode showed non-uniform swelling.

(Contd)

Appendix B-2. Post-Test Examination of Bicells

Cell Description	Lifetime Cycles	Lifetime Days	Reason Terminated	Comments
R-31, Li-Al/NiS_2-CoS_2	378	1040	Short circuit	Short circuit was caused by extrusion of positive electrode material around the folded BN fabric separator at the top of the cell. The positive electrode was severely compressed in this area by expansion of the negative electrodes. Dimensional uniformity of the electrodes was poor.
M-7, Li-Al/$FeS_{1.44}$	85	136	Declining coulombic efficiency	The cause of the declining coulombic efficiency (85%) was not identified. The Y_2O_3 felt separator showed evidence of reaction with the positive electrode to form Y_2O_2S. Negative electrode showed expansion of almost 100%. The 6-mm thick separator was compressed to ∿1.4-mm. Li_2S was deposited within the separator. Utilization was non-uniform in the negative electrode.
M-9, Li-Al/FeS-Cu_2S	132	240	Declining capacity	Specific cause of declining capacity was not identified. Negative electrodes showed agglomeration in back positions (∿90 vol % Li-Al). Front portions of electrodes were ∿50 vol % Li-Al. Positive electrode very dense looking (50-70 vol %) for a charged condition. Metallic copper was deposited within separator. BN felt separator was compressed from 6 to 1.5-1.7-mm. Negative electrodes showed excessive expansion (>50%).
KK-14, Li-Al/FeS-Cu_2S	151	301	Declining coulombic efficiency	The cause for the declining coulombic efficiency (∿75%) was not identified. Possible contributing factors are: six freeze-thaw cycles, metallic copper deposits within separators, and non-uniform utilization of the negative electrodes (bottom portions were depleted of Li, while the upper portions contained normal LiAl for charged electrodes). BN felt was compressed from 6 to ∿1.9 mm. Electrodes showed considerable expansion
PW-14, Li-Al/FeS-Cu_2S	22	26	Short circuit	Short circuit was caused by a defective feedthrough. This cell used a MgO powder separator (-60 + 120 mesh) and was more densely loaded in the bottom portion (∿50 vol %) than in the top (>40 vol %). Also, a considerable amount of MgO was present within the positive electrode. This apparently occurred during vibratory loading of the MgO powders.
R-41, Li-Al/FeS-Cu_2S	180	351	Short circuit	Short circuit was caused by the electrode frames at the top of the cell cutting through the BN felt separator. This was caused by the excessive swelling of the positive electrode (50-100% expansion). Metallic copper was deposited within the separator. A band of α-$LiAlO_2$ was observed at the top of the negative electrodes, indicating exposure to oxygen during assembly or operation.

(Contd)

Appendix B-2. Post-Test Examination of Bicells

Cell Description	Lifetime Cycles	Lifetime Days	Reason Terminated	Comments
JS-3, Li-Al/FeS-Cu_2S	8	10	Short circuit	Short circuit was caused by extrusion of positive material through the overlap; point of the separator at the top of the positive electrode. The negative electrodes showed ~100% expansion in this area. The positive electrode showed excessive expansion at the bottom (>50%), whereas the negative electrodes were severely compressed.
R-38, Li-Al/FeS-C	94	172	Short circuit	Short circuit was caused by the extrusion of positive electrode material past the overlap in the separator at the top of the electrode; appearance of the electrodes indicated non-uniform utilization of the electrodes from top to bottom.
R-40, Li-Al/FeS-C	63	109	Short circuit	Short circuit was caused by the feedthrough. Examination showed that electrolyte leaked from the cell through the BN powder seal. This allowed corrosion to occur at the top of the feedthrough with the formation of a metallic bridge across the upper insulator. BN powder (-325 mesh) was inadvertently used for the seal rather than the -40 +325 BN powder which forms a better seal.
HC-2, Li-Al/FeS_2	111	144	Short circuit	Cell assembled in air, with Li_2FeS_2 used as starting material in the positive electrode. Examination showed $LiAlO_2$ in the negative electrode tops, indicating air reaction with the Li-Al alloy. Short circuit caused by sulfide deposits in the separator and conductive ZrO_2 contacting both electrodes.
KK-6, Li-Al/FeS_2-CoS_2	183	313	End of test	Lithium sulfide deposits typical of FeS_2 cells were observed within the separator. Also, Li_2S or Al_2S_3 was observed in the negative electrodes. The negative electrodes were cast plates with 11 wt % Li. These electrodes expanded by more than 100% in thickness, and the back 1/3 was α-Al(Li-Al depleted of Li), with the remainder LiAl. This indicates non-uniform reaction.
M-8, Li-Al/FeS	197	347	End of test	Negative electrodes had expansion of about 100%. The BN felt separator had been compressed from 6 to 2.4 mm. The corrosion of the electrodes was somewhat greater than normal.
PW-8, Li-Al/FeS	280	673	End of test	Negative electrodes showed excessive expansion in thickness and the positive electrode was severely compressed. The MgO powder separator was 3-mm thick on one face of the positive electrode and 5-mm thick on the other face. Also, MgO powder was observed inside the positive electrode (see Cell PW-14). The positive electrode showed some evidence of non-uniform reactions from top (mostly Li_2FeS_2) to bottom (mostly J-phase).

Distribution for ANL-79-39

Internal:

M. V. Nevitt
R. V. Laney
P. R. Fields
S. A. Davis
B. R. T. Frost
G. T. Garvey
J. J. Roberts
K. E. Anderson
J. D. Arntzen
B. Bandyopadhyay
J. Barghusen
D. L. Barney (25)
L. Bartholme
J. E. Battles
E. C. Berrill
L. Burris
F. A. Cafasso
A. A. Chilenskas (25)
K. Choi
P. Cunningham
D. Day
W. DeLuca
P. A. Eident
R. Elliott
P. Eshman
M. K. Farahat
A. K. Fischer
E. C. Gay
J. E. A. Graae
J. L. Hamilton
J. Harmon
E. R. Hayes
F. Hornstra
A. A. Jonke
T. D. Kaun
R. W. Kessie
G. M. Kessler
J. E. Kincinas
K. Kinoshita
V. M. Kolba
W. Kremsner
M. L. Kyle
W. W. Lark
S. Lawroski
R. F. Malecha
F. J. Martino
C. A. Melendres
A. Melton
W. E. Miller
F. Mrazek
K. M. Myles
Z. Nagy
P. A. Nelson (50)
N. Otto
E. G. Pewitt
R. B. Poeppel
S. Preto
G. Redding
K. A. Reed
M. F. Roche
L. E. Ross
M. Saboungi-Blander
W. W. Schertz
J. L. Settle
H. Shimotake
M. A. Slawecki
J. A. Smaga
R. K. Steunenberg
S. Susman
B. Swaroop
C. A. Swoboda
C. Sy
Z. Tomczuk
R. Varma
D. R. Vissers
S. Vogler
D. S. Webster
S. E. Wood
N. P. Yao
S. M. Zivi
A. B. Krisciunas
ANL Contract File
ANL Libraries (5)
TIS Files (6)

External:

DOE-TIC, for distribution per UC-94cb (346)
Manager, Chicago Operations and Regional Office, DOE
Chief, Office of Patent Counsel, DOE-CORO
V. Hummel, DOE-CORO
W. R. Frost, DOE-CORO
President, Argonne Universities Association
Chemical Engineering Division Review Committee:
- C. B. Alcock, U. Toronto
- R. C. Axtmann, Princeton Univ.
- R. E. Balzhiser, Electric Power Research Institute
- J. T. Banchero, Univ. Notre Dame
- T. Cole, Ford Motor Corp.
- P. W. Gilles, Univ. Kansas
- R. I. Newman, Allied Chemical Corp.
- G. M. Rosenblatt, Pennsylvania State Univ.

E. Adler, Hughes Aircraft Co., El Segundo
J. G. Ahlen, Illinois Legislative Council, Springfield
J. W. Alpha, Corning Glass Works, Corning, N. Y.
J. Ambrus, Naval Surface Weapons Center, Silver Spring, Md.
J. N. Anand, Dow Chemical Co., Walnut Creek, Calif.

F. Anson, California Inst. Technology
B. Askew, Gould Inc., Rolling Meadows, Ill.
P. Auh, Brookhaven National Lab.
B. S. Baker, Energy Research Corp., Danbury, Conn.
H. Balzan, Tennessee Valley Authority, Chattanooga
K. F. Barber, Div. Electric and Hybrid Vehicle Systems, USDOE
H. J. Barger, Jr., U. S. Army MERDC, Fort Belvoir
R. W. Barnes, Lithium Corp. of America, Gantonia, N. C.
T. R. Beck, Electrochemical Technology Corp., Seattle
M. Benedict, Massachusetts Inst. Technology
D. N. Bennion, U. California, Los Angeles
J. Birk, Electric Power Research Inst.
J. Braunstein, Oak Ridge National Lab.
M. Breiter, GE Research & Development Center, Schenectady
J. O. Brittain, Northwestern U.
R. Brodd, Parma Technical Center, Union Carbide Corp.
J. J. Brogan, Div. Highway Systems, USDOE
E. Brooman, Battelle Memorial Inst., Columbus
B. D. Brummet, McGraw-Edison Co., Bloomfield, N. J.
M. C. Burton, Delco Remy, Anderson, Ind.
D. M. Bush, Sandia Laboratories
E. Buzzelli, Westinghouse Electric Corp., Pittsburgh
E. J. Cairns, Lawrence Berkeley Lab.
E. Carr, Eagle-Picher Industries, Joplin
P. Carr, Energy Development Associates, Madison Heights, Mich.
Chloride Systems (U. S. A.) Inc., North Haven, Conn.
C. Christenson, Gould Inc., Rolling Meadows, Ill.
M. Cohen, U. Chicago
A. R. Cook, Int'l Lead Zinc Research Organization, Inc., New York City
G. Coraor, E. I. duPont de Nemours & Co., Wilmington
D. R. Craig, Hooker Chemical Corp., Orchard Park, N. Y.
G. Cramer, Southern California Edison, Rosemead
F. M. Delnick, Sandia Labs.
H. Dietrich, Fiber Materials, Inc., Biddeford, Mass.
D. L. Douglas, Electric Power Research Inst.
E. Dowgiallo, MERADCOM, Ft. Belvoir
J. Dunning, General Motors Research Lab., Warren, Mich.
P. Eggers, Battelle Memorial Inst., Columbus
M. Eisenberg, Electrochimica Corp., Mountain View, Calif.
R. P. Epple, Div. Materials Sciences, USDOE
H. R. Esplg, Gould Inc., Rolling Meadows, Ill.
D. T. Ferrell, Jr., ESB Inc., Yardley, Pa.
P. L. Fleischner, National Beryllia Corp., Haskell, N. J.
J. H. B. George, Arthur D. Little, Inc., Cambridge, Mass.
J. Giner, Giner, Inc., Waltham, Mass.
G. Goodman, Globe-Union, Inc., Milwaukee
G. Gorten, Gorten and Associates, Sherman Oaks, Calif.
H. Grady, Foote Mineral Co., Exton, Pa.
S. Gratch, Birmingham, Mich.
D. Gregory, Inst. Gas Technology, Chicago
N. Gupta, Ford Motor Co., Dearborn, Mich.
N. Hackerman, Rice U.
G. Hagey, Div. of Environmental Impacts, USDOE
C. Halpin, Halpin Engrs., Grosse Point, Mich.

R. Hamilton, Carborundum Co., Niagara Falls
W. Hassenzahl, Los Alamos Scientific Laboratory
L. A. Heredy, Atomics International
B. Higgins, Eagle-Picher Industries, Joplin
R. Hudson, Eagle-Picher Industries, Joplin
J. R. Huff, U. S. Army Mobility Equipment R&D Center, Fort Belvoir
R. A. Huggins, Stanford U.
R. A. Huse, Public Service Electric & Gas Co., Newark, N. J.
S. D. James, U. S. Naval Surface Weapons Center, Silver Spring, Md.
M. A. Jansen, Allegheny Power Service Corp., Greensburgh, Pa.
G. Janz, Rensselaer Polytechnic Inst.
H. Jensen, C&D Batteries, Plymouth Meeting, Pa.
F. Kalhammer, Electric Power Research Institute
C. Kamienski, Lithium Corp. of America, Gastonia, N. C.
M. Katz, Div. Energy Storage Systems, USDOE
K. Kinsman, Ford Motor Co., Dearborn, Mich.
R. Kirk, Div. of Electric and Hybrid Vehicle Systems, USDOE
K. W. Klunder, Div. of Energy Storage Systems, USDOE
J. Kollar, Northfield, Ill.
J. Lagowski, Detroit Edison Utility Co.
H. Laitinen, U. Florida
J. J. Lander, Air Force Aero Propulsion Lab., Wright-Patterson AFB
A. Landgrebe, Div. of Energy Storage Systems, USDOE (6)
C. E. Larson, Bethesda, Md.
S. H. Law, Northeast Utilities, Hartford, Conn.
C. A. Levine, Dow Chemical Co., Walnut Creek, Calif.
D. Linden, U. S. Army Electronics Command, Fort Monmouth, N. J.
R. Llewellyn, Indiana State U.
P. S. Lykoudis, Purdue Univ.
J. Mathers, U. Maryland
C. J. Mazac, PPG Industries, Corpus Christi
J. McKeown, Office of Resource Management, USDOE
C. McMurty, Carborundum Co., Niagara Falls
D. Meighan, C&D Batteries, Plymouth Meeting, Pa.
R. C. Miller, Kawecki Berylco Industries, Inc., Boyertown, Pa.
R. Minck, Ford Motor Co., Dearborn, Mich.
R. Murie, General Motors Corp., Warren, Mich.
E. M. Murman, Flow Research Co., Kent, Wash.
G. Murray, Detroit Edison Utility Co.
J. Newman, U. California, Berkeley
J. Nowabilski, Union Carbide Co., Tonawanda
C. Pax, Div. Electric and Hybrid Vehicle Systems, USDOE (6)
G. F. Pezdirtz, Div. of Energy Storage Systems, USDOE
R. Pollard, U. California, Berkeley
R. K. Quinn, Sandia Labs.
L. H. Raper, Eureka Co., Bloomington, Ill.
R. Rightmire, Standard Oil of Ohio, Cleveland
P. F. Ritterman, TRW Inc., Redondo Beach
R. Rizzo, Globe-Union, Inc., Milwaukee
N. Rosenberg, Transportation Systems Center, Cambridge, Mass.
R. Rubischko, Gould Inc., Rolling Meadows, Ill.
A. J. Salkind, Rutgers U.
A. F. Sammells, Inst. Gas Technology, Chicago
W. Schaefer, Commonwealth Edison, Maywood, Ill.
G. Scharbach, American Motors General Corp., Wayne, Mich.

T. Schneider, Public Service Electric & Gas Co., Newark, N. J.
R. I. Schoen, National Science Foundation
J. R. Schorr, Battelle Memorial Inst., Columbus
D. R. Schramm, Public Service Electric & Gas Co., Newark, N. J.
H. J. Schwartz, NASA Lewis Research Center
J. R. Selman, Illinois Inst. Technology
J. A. Shropshire, Exxon Research and Engineering Co., Linden, N. J.
R. Singleton, U. S. Bureau of Mines, Washington
A. I. Snow, Atlantic Richfield Co., Harvey, Ill.
S. Srinivasan, Brookhaven National Lab.
D. Stakem, Catalyst Research Corp., Baltimore
E. Steeve, Commonwealth Edison Co., Chicago
R. H. Strange II, National Science Foundation
R. L. Strombotne, U. S. Dept. Transportation, Washington
S. Sudar, Atomics International
R. H. Swoyer, Pennsylvania Power and Light Co., Allentown
P. C. Symons, Energy Development Assoc., Madison Heights, Mich.
R. Szwarc, General Electric Co., St. Petersburg
F. Tepper, Catalyst Research Corp., Baltimore
L. Thaller, NASA Lewis Research Center
G. M. Thur, Div. Highway Systems, USDOE
C. W. Tobias, U. California, Berkeley
L. Topper, Div. of Res. & Technical Assessment, USDOE
W. Towle, Globe-Union, Inc., Milwaukee
A. A. Uchiyama, Jet Propulsion Lab.
J. Vanderryn, Office of International Affairs, USDOE
J. V. Vinciguerra, Eagle-Picher Industries, Joplin
J. B. Wagner, Arizona State U.
R. D. Walker, Jr., U. Florida
C. O. Wanvig, Jr., Globe-Union, Inc., Milwaukee
S. A. Weiner, Ford Motor Co., Dearborn, Mich.
J. Werth, ESB Inc., Yardley, Pa.
C. Wienlein, Globe-Union, Inc., Milwaukee
F. Will, General Electric R&D Center, Schenectady
A. Williams, Dow Chemical Co., Midland, Mich.
J. Withrow, Chrysler Corp., Detroit
S. E. Wood, El Paso, Tex.
T. Wydeven, NASA Ames Research Center
O. Zimmerman, Portland General Electric Co., Portland, Ore.
M. Zlotnick, Energy Technology, USDOE
Chloride Technical Limited, Manchester, England
L. Pearce, Admiralty Materials Lab., Holten Heath, England
E. Voss, Varta Batterie A. G., Kelkhern, Germany
E. Aiello, U. Chicago
W. J. Argersinger, Jr., U. Kansas
J. T. Banchero, U. Notre Dame
K. J. Bell, Oklahoma State U.
R. Blanco, Oak Ridge National Lab.
C. F. Bonilla, Columbia U.
W. Brandt, U. Wisconsin, Milwaukee
A. E. Dukler, U. Houston
W. J. Frea, Michigan Technological U.
J. E. Linehan, Marquette U.
Maine Univ., Prof. in charge of Chem. Engr. Lib.

Marquette U., Dept. of Chemistry
Michigan Technological U., Library
N. R. Miller, United Nuclear Industries, Richland
G. Murphy, Iowa State U.
E. A. Peretti, U. Notre Dame
G. W. Preckshot, U. Missouri
H. Rosson, U. Kansas
C. Sanathanan, U. Illinois—Chicago Circle
A. Sesonske, Purdue U.
USDOE, Director, Office of Safeguards and Security
B. W. Wilkinson, Michigan State U.
Comision Nacional de Energia Atomica, Library, Argentina
J. A. Sabato, Com. Nac. de Energia Atomica, Buenos Aires, Argentina
C. H. Cheng, Nat'l Tsing Hau Univ., China
National Radiological Protection Board, Library, Harwell, England
L. Kemmerich, Ges. fur Kernforschung, Karlsruhe, Germany
F. Weigel, Inst. fur Anorganische Chemie der U. Munich, Germany
N. Saratchandran, Bhabha Atomic Research Centre, Bombay, India
K. Fujimiya, U. of Tokyo, Japan
Japan Atomic Energy Research Inst., Tokai-mura, Japan
K. Matsuda, Inst. of Physical & Chemical Res., Yamato-machi, Japan
S-S. Lee, Korea Advanced Institute of Science, Korea
Korean Atomic Energy Research Institute, Korea
R. Nordberg, Sahlgren's Hospital, Göteborg, Sweden
T. Wallin, Royal Inst. Technology, Stockholm